Proceedings of the

XIX INTERNATIONAL SCIENTIFIC CONFERENCE ELECTRONICS AND APPLIED PHYSICS APHYS 2023

October, 17-21, 2023,
Kyiv, Ukraine

Taras Shevchenko National University of Kyiv
Faculty of RadioPhysics, Electronics and Computer Systems

Organizing Committee

A. Netreba, Associate Professor – Chairman, Faculty of RadioPhysics, Electronics and Computer Systems, Taras Shevchenko National University of Kyiv
N. Bashmakova – Vice-Chairman, Faculty of RadioPhysics, Electronics and Computer Systems, Taras Shevchenko National University of Kyiv
O. Nechyporuk, Associate Professor – Vice-Chairman, Faculty of RadioPhysics, Electronics and Computer SystemsTaras Shevchenko National University of Kyiv
V. Moiseienko, Laboratory Head – Secretary, Faculty of RadioPhysics, Electronics and Computer Systems, Taras Shevchenko National University of Kyiv
I. Anisimov, Professor, Faculty of RadioPhysics, Electronics and Computer Systems, Taras Shevchenko National University of Kyiv
Y. Boyko, Associate Professor, Faculty of RadioPhysics, Electronics and Computer Systems, Taras Shevchenko National University of Kyiv
A. Veklich, Professor, Faculty of RadioPhysics, Electronics and Computer Systems, Taras Shevchenko National University of Kyiv
V. Vysotskiy, Professor, Faculty of RadioPhysics, Electronics and Computer Systems, Taras Shevchenko National University of Kyiv
D. Ivanenko, Associate Professor, Faculty of RadioPhysics, Electronics and Computer Systems, Taras Shevchenko National University of Kyiv
A. Goriachko, Associate Professor, Faculty of RadioPhysics, Electronics and Computer Systems, Taras Shevchenko National University of Kyiv
A. Karlash, Associate Professor, Faculty of RadioPhysics, Electronics and Computer Systems, Taras Shevchenko National University of Kyiv
D. Bozhko, Ph.D. Assistant Professor, USA, University of Colorado, Colorado Springs
A. Konovalov, Assistant Professor, Faculty of RadioPhysics, Electronics and Computer Systems, Taras Shevchenko National University of Kyiv
M. Kononov, Associate Professor, Faculty of RadioPhysics, Electronics and Computer Systems, Taras Shevchenko National University of Kyiv
V. Lozovskyi, Associate Professor, Faculty of RadioPhysics, Electronics and Computer Systems, Taras Shevchenko National University of Kyiv
O. Nedybaliuk, Associate Professor, Faculty of RadioPhysics, Electronics and Computer Systems, Taras Shevchenko National University of Kyiv
V. Ovechko, Professor, Faculty of RadioPhysics, Electronics and Computer Systems, Taras Shevchenko National University of Kyiv
C. Patton, Professor, USA, Colorado University
S. Pogorilyi, Professor, Faculty of RadioPhysics, Electronics and Computer Systems, Taras Shevchenko National University of Kyiv
S. Radchenko, Associate Professor, Faculty of RadioPhysics, Electronics and Computer Systems, Taras Shevchenko National University of Kyiv
S. Savenkov, Professor, Faculty of RadioPhysics, Electronics and Computer Systems, Taras Shevchenko National University of Kyiv
V. Skryshevsky, Professor, Institute of High Technologies, Taras Shevchenko National University of Kyiv
M. Strikha, Professor, Faculty of RadioPhysics, Electronics and Computer Systems, Taras Shevchenko National University of Kyiv
B. Hillebrands, Professor, Germany, Kaiserslautern University
I. Marushchak – Engineer, Faculty of RadioPhysics, Electronics and Computer Systems, Taras Shevchenko National University of Kyiv

O. Mokhonko – PhD Student, Faculty of RadioPhysics, Electronics and Computer Systems, Taras Shevchenko National University of Kyiv
O. Murmantsev – PhD Student, Faculty of RadioPhysics, Electronics and Computer Systems, Taras Shevchenko National University of Kyiv
R. Bohdanov – PhD, Faculty of RadioPhysics, Electronics and Computer Systems, Taras Shevchenko National University of Kyiv

General information

Date	October, 17-21, 2023
Location for mails	Taras Shevchenko National University of Kyiv Volodymyrska Str. 64/13, 01601 Kyiv – Ukraine
Physical location	Faculty of RadioPhysics, Electronics and Computer Systems, Taras Shevchenko National University of Kyiv, Prospect Glushkova, 4g, Kyiv 03022, Ukraine
Organization	Taras Shevchenko National University of Kyiv, Faculty of RadioPhysics, Electronics and Computer Systems

Scientific program

The Conference contributions are accepted from the following areas:

1. Laser Physics and Optoelectronics
2. Surface Physics, Nano- and Microelectronics
3. Physics of Semiconductors and Dielectrics, Semiconductor Devices
4. Physics of Magnetism
5. Computer Technologies
6. Mathematical Problems of Applied Physics
7. Medical Physics
8. Plasma Physics
9. Radio Engineering and Communications
10. Polarimetry: Theory and Applications

Conference site

All events associated with the XIX International Scientific Conference Electronics and Applied Physics will take place in on-line regime in 2023.

Time

Local time is one hour ahead of Middle European time.

Conference language

The language of the Conference Proceedings is English.

Presentation

The Conference program includes invited lectures and contributed papers. All reports will be lectured in oral presentation.
Invited talks: 45 minutes (including discussion)
Other talks: 15 minutes (including discussion)

Edited by O. Mokhonko, Dr. O. Nechyporuk.

PREFACE

The XIX INTERNATIONAL SCIENTIFIC CONFERENCE ELECTRONICS AND APPLIED PHYSICS (APHYS 2023) will be held October, 17-21, 2023, in the capital of Ukraine Kyiv. The famous scientific and cultural center of Europe welcomes over 75 delegates from different Universities and Scientific Centers of 5 countries of Europe, America and Asia.

The intend of APHYS 2023 is to provide a forum where novel and relevant achievements in Applied Physics (RadioPhysics and Electronics) could be discussed, to bring together young scientists of different disciplines and foster their cooperation, to stimulate international research in the field of Applied Physics, development, fabrication and application of new physical ideas in the corresponding devices. It is too important now for Ukraine as a member of Bologna Process and as well as of European Community.

The APHYS 2023 is organized by Faculty of RadioPhysics, Electronics and Computer Systems of Taras Shevchenko National University of Kyiv.

The Conference technical program is divided into nine sessions; three invited lectures and more than 50 oral contributions will be presented, discussed and argued.

We believe the APHYS 2023 will give a chance for students, postgraduate students, young professors and scientists to discuss their problems and give an impulse for the development of future research and success.

We hope the delegates will enjoy the meeting. We hope also the participants and accompanying guests will enjoy visits to local places interests.

The next INTERNATIONAL SCIENTIFIC CONFERENCE ELECTRONICS AND APPLIED PHYSICS will be held in Kyiv, from October 22 to 25, 2024.

Dr. A. Netreba,
Chairman of the Organizing Committee

Dr. O. Nechyporuk,
Vice-Chairman of the Organizing Committee

INVITED LECTURES

INTRODUCTION TO BASICS OF INTELLECTUAL PROPERTY: WHAT ONE NEEDS TO KNOW WHILE WORKING IN HIGH TECH?

Dr. Alina Veligura
Head of IP for Monitoring and Enterprise Informatics,
Philips IP&S, Eindhoven, The Netherland

In many fields of industry, Intellectual Property (IP) and especially patents are an essential part of business to obtain an advantage over competitors.
Intellectual property is a product of intellectual labor or in simpler words: everything originating from your mind. There are five types of intellectual property, each of which is protectable by a corresponding Intellectual property right.
Amongst these types of intellectual property, three of them are often more relevant to the activities in the high tech industry:

1. Products of the original creative work (text, photo, software, etc.), which are protectable by a copyright;
2. Know-how, which is protectable by a Trade Secret; and
3. Technical inventions protectable by patent rights.

When working on your own creative content, be it a preparation of the scientific manuscript or a presentation at the conference, one needs to be aware of making use of the content of others, be it a picture from the internet of a piece of the software code, without violation of their copyright. Additional attention should be paid to the usage of the open-source software and IP license conditions associated with it. In some instances, such a usage in one's own software code may result in an obligation of making said software code or other IP originating from this development available to others.
Separate attention should be given to the usage of an output from generative Artificial Intelligence (AI) models. This output may include copyrighted work of others, who have not given their permission to have their work being used in any way. Of course, one should not forget that entering confidential information as an input to the generative AI model (unless one is certain about confidential conditions of the AI model provider) would potentially make this information available to others.
Another important IP right to high tech industry, and any industry in general, is the patent right protecting technical inventions. Patents are exclusive rights granted by the government to an inventor for their invention. Having a patent implies making a deal: the right to exclude others from exploiting the invention (during a limited period) versus the obligation to disclose the invention in detail to support technical progress. While specific details of invention's eligibility to a patent protection may differ from one country to another, there is one main criterion which is the same in all countries: an invention shall be novel (not forming a part of the prior art). Invention not forming a part of the prior art means that nowhere in the world such an invention has been: (i) described in any document; or (ii) disclosed orally (for example, at the conference or workshop); or (iii) used in any way. Only after meeting a condition of novelty the invention can be further assessed on its patentability.
Concluding with the basic introduction into most important IP aspects in high tech industry, be aware of IP ownership: "Who owns IP one creates?" and the fact that in majority of countries such an ownership is defined a labor agreement one's employer, wherein unless specified otherwise, the employer owns products of the intellectual labor of their employees.
To summarize, be aware of your IP rights and respect IP rights of others.

NONLINEAR DYNAMICS OF SKYRMION STRINGS

Volodymyr P. Kravchuk
Leibniz-Institut für Festkörper- und Werkstoffforschung, IFW Dresden, 01171 Dresden, Germany
e-mail: v.kravchuk@ifw-dresden.de

The skyrmion core, percolating the volume of the magnet, forms a skyrmion string -- a topological Dirac-string-like object. Here we analyze the nonlinear dynamics of a skyrmion string in a low-energy regime by means of the collective variables approach, which we generalized for the case of strings. Using the perturbative method of multiple scales (both in space and time), we show that the weakly nonlinear dynamics of the translational mode propagating along the string is captured by the focusing-type nonlinear Schrödinger equation. As a result, the basic "planar-wave" solution, which has the form of a helix-shaped wave, experiences modulational instability. The latter leads to the formation of cnoidal waves. Both types of cnoidal waves, dn- and cn-waves, as well as the separatrix soliton solution, are confirmed by micromagnetic simulations. Beyond the class of traveling-wave solutions, we found Ma-breather propagating along the string. Finally, we proposed a generalized approach that enables one to describe the nonlinear dynamics of the modes of different symmetries, e.g., radially symmetrical or elliptical.

For more details see Refs. [1, 2]

References

[1] V.P. Kravchuk, *Nonlinear dynamics of skyrmion strings*. arXiv:2306.11866 (2023) [accepted for publication in Phys. Rrev. B].
[2] S. Okumura, V.P. Kravchuk, M. Garst, *Instability of Magnetic Skyrmion Strings Induced by Longitudinal Spin Currents*, Physical Review Letters, **131**, 066702 (2023).

HIGH-PERFORMANCE OF LIQUID-GATED SILICON NANOWIRE FIELD-EFFECT TRANSISTORS COVERED WITH ULTRATHIN LAYERS OF DIAMOND LIKE TETRAHEDRAL AMORPHOUS CARBON

Nazarii Boichuk
Bioelectronics (IBI-3), Forschungszentrum Jülich, Germany

LASER PHYSICS AND OPTOELECTRONICS

NON-DESTRUCTIVE TESTING OF MAO ALUMINA COATINGS USING SUB-THZ ELLIPSOMETRY

Galuza A.A.*, Kolenov I.V., Vinnikov D.V.***, Mizrakhy S.V.*****

**National Technical University "Kharkiv Polytechnic Institute", 2 Kyrpychova St., Kharkiv 61002, Ukraine, e-mail: alexey.galuza@gmail.com*

***Institute of Electrophysics and Radiation Technologies of the NAS of Ukraine, P.B. 8812, 28 Chernyshevsky St., Kharkiv 61002, Ukraine,*

O.Ya. Usikov Institute for Radiophysics and Electronics of the NAS of Ukraine, 12, Ac. Proskura St., Kharkiv 61085, Ukraine

e-mail: ivan.kolenov@gmail.com

****National Science Center Kharkiv Institute of Physics and Technology, Kharkiv, Ukraine, email: vinniden@gmail.com*

*****O.Ya. Usikov Institute for Radiophysics and Electronics of the NAS of Ukraine, 12, Ac. Proskura St., Kharkiv 61085, Ukraine*

emial: smizrakhy@hotmail.com

The work is devoted to the possibility of using sub-terahertz ellipsometry for non-destructive testing of oxide coatings on the surface of aluminum (Al2O3 coating on an Al substrate) obtained by microarc oxidation. Reliable estimates are obtained for such coating parameters as thickness, structure, and composition. The applicability of various planar ellipsometric models for determining the coating parameters is considered. A piecewise ellipsometric model is proposed, which made it possible to determine the distribution of parameters over the coating surface.

Introduction

In recent years, the microarc oxidation (MAO) method has become increasingly popular, due to which it is possible to synthesize nanoceramic superhard corrosion-resistant composite layers on the surface of various products, including medical ones [1–3]. The structure and properties of the coating depend on many factors: thermal, physicochemical, hydrodynamic, etc. [1, 2]. Therefore, the development of the technological process for obtaining coatings with the desired set of properties (structure, coating thickness, roughness, porosity, etc.) can be quite laborious and requires express control of the coating state [3]. Typically, the following methods are used for these tasks: optical microscopy, scanning electron microscopy (SEM), X-ray diffraction analysis (XRD), etc. SEM and XRD methods are not express ones; optical microscopy is not very informative [1].

Ellipsometry is a non-destructive, high-precision, reproducible express method for studying the interface of media [4, 5]. The large wavelength of sub-terahertz ellipsometry makes it possible to consider the rough surface of MAO coatings as a homogeneous layer with some effective optical constants, which simplifies the processing of experimental data [6]. In this paper, we propose to use sub-terahertz ellipsometry as an express method for monitoring the properties of MAO coatings.

Samples and research methods

Al plates 57×25 mm in size and 1 mm thick were used as samples for research, which subjected the MAO treatment of various durations (1, 10, 20, and 30 min.). The cooling system maintained the electrolyte temperature not higher than 60°C.

For ellipsometric studies, we used a quasi-optical terahertz ellipsometer assembled from elements based on a hollow dielectric beam guide and operating according to a scheme with a rotating analyzer. An avalanche-transit diode with an operating wavelength of 2.14 mm, which is much larger than the size of the film roughness, was used as a radiation source. The setup used is described in detail in [7, 8]. As auxiliary methods, optical microscopy, scanning electron microscopy, and X-ray diffraction analysis were used.

Results and discussion

As a result of studying the samples of MAO coatings on aluminum plates with different processing times, it was shown that standard multilayer planar models do not allow for describing the results of an ellipsometric experiment correctly. It has been established that it is a consequence of the systematic (regular) non-uniformity of the thickness of the coating (in the middle of the sample, the film is thinner than at the edges). It is shown that this inhomogeneity correlates with the electric field distribution during MAO treatment. Therefore, for processing experimental data, a piecewise surface model was proposed, which made it possible to describe surface structures with a gradient of properties over the sample surface more adequately than standard planar models. However, the standard single-layer surface model makes it possible to determine the average thickness

of inhomogeneous coatings with sufficient accuracy. In this case, the deviation of the single-layer model from the experimental data can be a measure of the non-uniformity (primarily of the thickness gradient over the surface) of the coating. The correctness of the constructed model was confirmed by independent measurements of the thicknesses, composition, and structure of the resulting films. It is shown that the results of the ellipsometric experiment in the sub-terahertz range are practically insensitive to the parameters of the metal substrate, which eliminates the need to determine the optical constants of a particular metal substrate with high accuracy. Estimates of the optical constants of mullite in the sub-terahertz range were carried out and were n=3.44, k=0.53.

Thus, we have shown that sub-terahertz multiangle ellipsometry is an effective method for non-destructive express-control of the MAO coatings parameters. This method is very sensitive to surface changes even in the very early stages of coating formation when other non-destructive methods (such as XRD) do not yet detect any changes.

Acknowledgments

This work was partly supported by the Simons Foundation, USA, Presidential Discretionary-Ukraine Support Grants (Award Number: 1030287).

References

[1] F. Simchen, M. Sieber, A. Kopp, and T. Lampke, “Introduction to plasma electrolytic oxidation — an overview of the process and applications,” Coatings, vol. 10(7), p.627, 2020.

[2] D.-S. Tsai and C.C. Chou, “Review of the soft sparking issues in plasma electrolytic oxidation,” Metals, vol. 8(2), 2018.

[3] D. Vinnikov, A. Ozerov, V. Yuferov, and V. Fomin, “The microplasma aluminum and titanium oxidation in condensed environments,” Probl. At. Sci. Technol., vol. 1(125), pp. 178–184, 2020.

[4] H. Fujiwara, *Spectroscopic Ellipsometry: Principles and Applications*. Wiley, Chichester, 2007.

[5] R.M.A. Azzam and N.M. Bashara, *Ellipsometry and Polarized Light*. North Holland, Amsterdam, 1999.

[6] A.I. Belyaeva, A.A. Galuza, V.K. Kiseliov, I.V. Kolenov, A.A. Savchenko, E. M. Kuleshov, and S.Y. Serebriansky, “Quasioptical scale modeling of metal surface localized defects influence on optical ellipsometry data,” Telecommun. Radio Eng., vol. 75(2), pp. 171–181, 2015.

[7] A.A. Galuza, V.K. Kiseliov, I.V. Kolenov, A.I. Belyaeva, and Y.M. Kuleshov, “Developments in THz-range ellipsometry: quasi-optical ellipsometer,” IEEE Trans. THz Sci. Technol., vol. 6(2), pp. 183–190, 2016.

[8] A. Belyaeva, A. Galuza, I. Kolenov, and S. Mizrakhy, “Developments in terahertz ellipsometry: Portable spectroscopic quasi-optical ellipsometer-reflectometer and its applications,” J. Infrared, Millim., Terahertz Waves, vol. 42(2), pp. 130–153, 2021.

FEATURES OF FOCUSING COMBINED MODES OF DIELECTRIC WAVEGUIDE RESONATOR

Degtyarev Andrey*, Dubinin Mykola*, Maslov Vyacheslav*,
Muntean Konstantin*, Svystunov Oleg*

**V.N. Karazin Kharkiv National University, e-mail: mykola.dubinin@karazin.ua*

In the last decade there has been a significant growth in research related to the terahertz (THz) range of electromagnetic radiation [1]. To date, many terahertz laser sources have been developed ranging from milliwatt femtosecond laser-based generators to free electron lasers with average power of hundreds of watts [2]. However, the application of THz technologies has not reached its potential yet due to the lack of compact and powerful sources of THz radiation having wide spectral range. Therefore, both the development and study of lasers emitting in THz range are still hot topics [3]. Research on the selection and focusing of THz laser beams is also topical today. Analysis of the literature allows us to conclude that the fundamental and higher laser modes with linear, radial, and azimuthal polarizations have been studied in the known works. It is also known that waveguide gas lasers generate efficiently the combined modes that have a more complex spatial field distribution [4]. However, not enough attention has been paid to the study of combined regimes so far.

This work is devoted to the study of higher-order combined modes generated by a THz laser whose resonator contains a hollow dielectric circular waveguide. The main attention was paid to the study of the spatial structure of radiation beams formed by combined modes $TE_{0n}+EH_{2n}$ and $EH_{-1n} + EH_{3n}$ (n = 1, 2, 3). Both the propagation of formed beams in free space and their moderate and sharp focusing by long- and short-focal distance lenses are considered.

The vector theory of Rayleigh-Sommerfeld was used to model propagation in free space of laser beams excited by the modes of a quasi-optical waveguide resonator. Well-known methods of measuring the spatial-energy characteristics of laser beams in the THz range for experimentally study were used. The setup contained a waveguide gas laser based on formic acid HCOOH vapor, which has strong emission lines in the THz range. The THz laser was optically pumped by a cw CO2 laser described in [5]. The optical resonator of the THz laser contained an input phase shifter and an output flat translucent mirror with a circular hollow dielectric waveguide placed between the mirrors [6]. The current configuration of the resonator favors the preferential formation and selection of combined laser modes. The spectrum of the generated laser modes is shown in Fig. 1. The radiation was registered by a pyroelectric photodetector equipped with a pinhole diaphragm of 0.2 mm diameter.

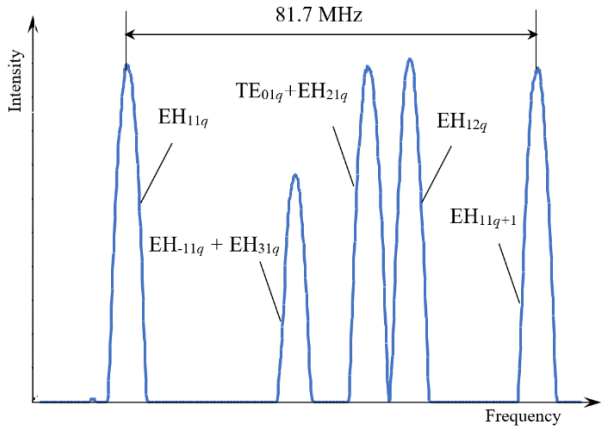

Fig. 1. Mode spectrum of the HCOOH laser

The generation power of the THz laser on the EH_{11q} and $TE_{01q}+EH_{21q}$ modes was 3.6 mW, while the generation power for the $EH_{-11q}+EH_{31q}$ and EH_{12q} modes was 2.9 mW. The laser was set to the more powerful linearly polarized $TE_{01q}+EH_{21q}$ mode to study the sharp and moderate

focusing of the combined modes. The focal length of the short-focus lens was 36.36 mm and the long-focus lens was 160 mm. The lens used in the experimental setup was mounted at 300 mm from the output mirror of the THz laser providing full coverage of the laser beam. The transverse distribution of the radiation of the studied mode was measured for both types of focusing - sharp and moderate.

It is theoretically and experimentally found that the plane of the TE_{01q}+ EH_{21q} mode field intensity peak at moderate focusing is shifted from the lens focal plane by a distance $z_{Imax} = 11.56\ \lambda$ in the direction of increasing the z coordinate. A similar shift of the peak intensity plane for the same mode at sharp focusing is only $z_{Imax} = 1.48\ \lambda$. The transverse intensity distributions in the plane of the field intensity peak for the focused combined TE_{01q}+ EH_{21q} mode at moderate and sharp focusing are shown in Fig. 2. The figures show that in the region of the minimum size of the focused beams, the transverse intensity distribution of the TE_{01q}+EH_{21q} mode maintains its circular shape regardless of whether the focusing is moderate or sharp. The calculated and experimental distributions of the intensity of the focused mode TE_{01q}+EH_{21q} diverge slightly. This discrepancy in the intensity distributions can be explained by the influence of lens aberrations which were not considered in the calculation as well as by the insufficient resolution of the photodetector.

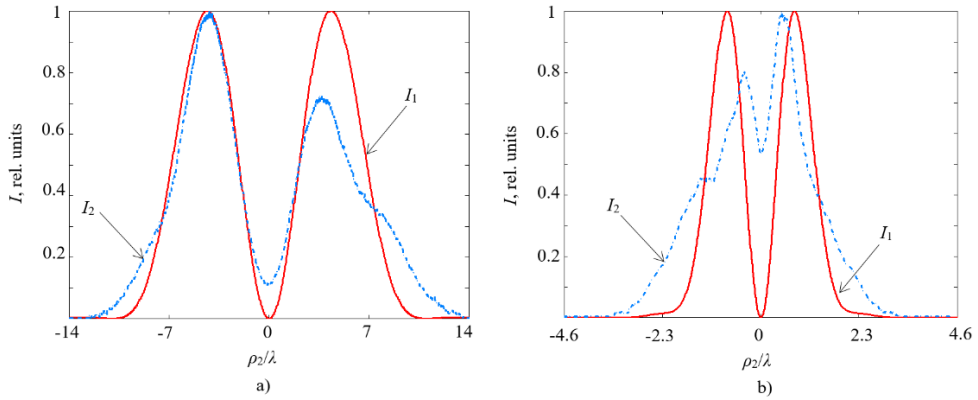

Fig. 2. Calculated (I_1) and experimental (I_2) transverse distributions of the total field intensity of the TE_{01q}+ EH_{21q} mode under moderate (a) and sharp (b) focusing.

The experiment showed that the diameter of the focused TE_{01q}+ EH_{21q} mode (FWHM) at moderate focusing (NA = 0.16) was 12.9 λ (notice that FWHM = 13.6 λ in calculations) while the same diameter at sharp focusing (NA = 0.68) was 2.2 λ (notice that FWHM = 2.55 λ in calculations). The physical features of the spatial-energy characteristics of THz laser beams with linear field polarization at sharp and moderate focusing in free space are analyzed theoretically and experimentally. The vector theory of Rayleigh-Sommerfeld was used to model propagation in free space of laser beams excited by the modes of a quasi-optical waveguide resonator. Well-known methods of measuring the spatial-energy characteristics of laser beams in the THz range for experimentally study were used. It is shown that the intensity of the total electric field of both combined TE_{0n}+EH_{2n} and
EH_{-1n}+EH_{3n} modes (n = 1, 2, 3) is defined in the focal region by all three components and has a dip on the axis for both types of focusing. The central maxima of the field of these modes are significantly shifted from the geometric foci of the lenses used as the order n of these modes increases. The EH_{-11}+EH_{31} mode has the smallest diameter (2.94 λ) of the focal spot in the region of maximum intensity with sharp focusing. The TE_{01}+EH_{21} mode has the smallest diameter (13.65 λ) of the focal spot with moderate focusing.

References

1. I.F. Akyildiz, C. Han, Z. Hu, S. Nie, J.M. Jornet, Terahertz band communication: an old problem revisited and research directions for the next decade, IEEE Trans. Commun. 70 (6) (2020) 4250–4285. https://doi:10.1109/TCOMM.2022.3171800.
2. A. Saha, A. Biswas, K. Ghosh, N. Mukhopadhyay, Optical to Terahertz Engineering, Springer, 2023.
3. A. Leitenstorfer, A.S. Moskalenko, T. Kampfrath, J. Kono, E. Castro-Camus, K. Peng et al., The 2023 terahertz science and technology roadmap, J. Phys. D: Appl. Phys. 56 (2023) 223001. https://doi.org/10.1088/1361-6463/acbe4c.
4. J. Henningsen, M. Hammerich, A. Olafsson, Mode structure of hollow dielectric waveguide lasers, Appl. Phys. B 51 (4) (1990) 272–284. https://doi.org/10.1007/BF00325048.
5. A. Degtyarev, V. Maslov, A. Topkov, Continuous-wave Terahertz Waveguide Lasers, LAP LAMBERT Academic Publishing, 2020.
6. O.V. Gurin, A.V. Degtyarev, N.N. Dubinin, M.N. Legenkiy, V.A. Maslov, K.I. Muntean, V.N. Ryabykh, V.S. Senyuta, Formation of beams with nonuniform polarisation of radiation in a cw waveguide terahertz laser, Quantum Elec. 51(4) (2021) 338–342. https://doi.org/10.1070/QEL17511.

PACKET QUANTIZATION OF THE ELECTROMAGNETIC FIELD

Volodymyr Ovechko*

**Faculty of RadioPhysics, Electronics and Computer Systems, Taras Shevchenko National University of Kyiv, Volodymyrska Str. 64/13, Kyiv 03127, Ukraine, email: ovs@univ.kiev.ua*

A method of packet representation of the electric field operator based on the use of a model of a quantum oscillator with an energy-limited parabolic potential is proposed. The energy of a photon is determined by its duration τ and the order of the elementary wave packet

Introduction

Significant practical improvements in devices for the generation and detection of single-photon optical signals led to the activation of the development of new areas of quantum optics: quantum computers, the latest information systems, quantum tomographs. At the same time, a modern experimental base was formed for the study of fundamental quantum phenomena: entangled quantum states, particle-wave properties of quantum objects, conditions for distinguishing classical and quantum properties, etc. A special place in this list is occupied by the carrier of the electromagnetic field - the photon. Its integral characteristics are well known and have been used in quantum optics for more than 100 years, starting with the works of M. Planck, A. Einstein, and P. Dirac. However, the modern stage requires the study and application of more detailed structural characteristics of photons as quantum objects limited in time and space.

The thesis that any physical object must be local cannot be doubted [1]. The use in Planck's formula for the energy of a frequency photon as a characteristic of a monochromatic (infinite) signal can be considered as an approximate limiting case. The problem is similar to that in classical physics: is the distribution of parameters of local objects correct on the basis of infinite harmonic functions? The answer is almost obvious: the basis functions must be defined in a limited domain. This work is devoted to the substantiation of such a series distribution for the field representation of photons.

Theory

Report plan: 1. A quantum oscillator with parabolic truncated potential (PTP). 2. Eigenfunctions and eigenenergies of a two-level quantum oscillator. 3. Basic functions of the two-level system: elementary wave packages. Conditional extremum problem. 4. Electromagnetic field operator. Coherent states. 5. The shape of the photon (spatial-temporal modes) and its energy formula.

1. The question is to what extent the limitations of the potential for the creation of a two-level system affect the spectrum of self-energies

$$U(x) = \begin{cases} \frac{1}{2} m(\omega x)\text{^}2 , & |x| \le a \\ \frac{1}{2} m(\omega a)\text{^}2 , & |x| > a \end{cases} \qquad (1)$$

2. The first conclusion: the number of levels depends on U_0. A particular two-level system will be in the range of cutoff energies $(3/2)\ \hbar\omega \le U_0 \le (5/2)\ \hbar\omega$. Second: an increase in the cutoff potential brings the eigenvalues of the energy closer to $\hbar\omega/2;\ 5\ \hbar\omega/2$ for even states and to $3\ \hbar\omega/2;\ 7\ \hbar\omega/2$ for odd ones. Therefore, the amplitudes of the potentials can be considered optimal: $U_0 = 4\ \hbar\omega/2;\ 5\ \hbar\omega/2$. Third: the energy of the ground state for these amplitudes is equal to $\hbar\omega/2$ as it should be. The structure of levels for $U_0 = (5/2)\ \hbar\omega$ is shown in Fig. 1.

3. We have solved the variational problem for the conditional extremum. Let's write Fermi's "golden rule" as object function. Additional connections

$$\int_{-1/2}^{1/2} f_{od}(p)\, dp = 0 \qquad (2)$$

$$\int_{-1/2}^{1/2} f_{od}^2(p)\, dp = 1 \qquad (3)$$

The justification of conditions (2) - (3), see work [2] $(p = t / \tau)$.

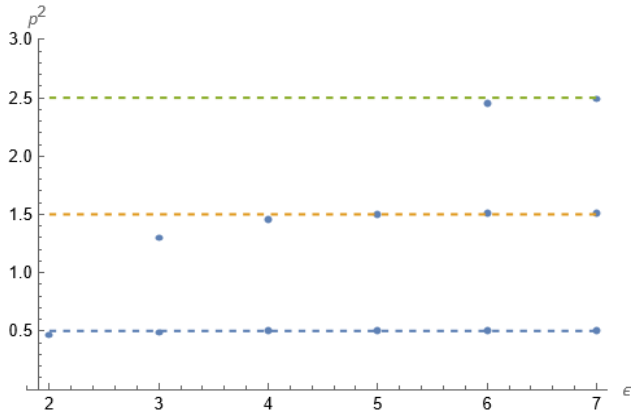

Fig. 1. Dependencies of energy eigenvalues E_i on the cutoff U_0 of the PTP: $\varepsilon = 2\,U_0 / \hbar w$, $p^2 = E / \hbar w$

Graphs of odd functions of lower orders are shown in Fig. 2

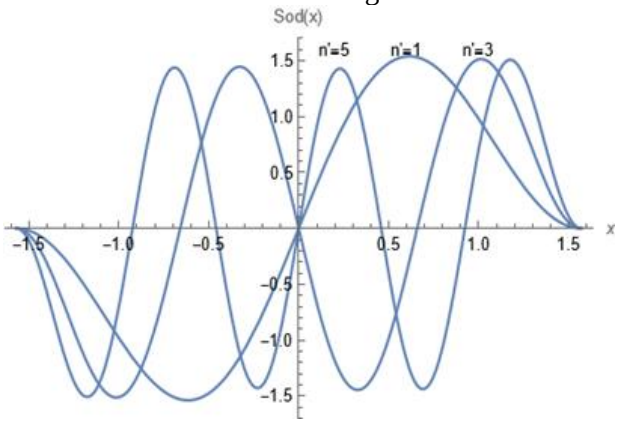

Fig. 2. The optimal shape of the n′-th order odd pulse signal $S_{od}(x)= f_{od}(x) : x = \pi t / \tau$

4. The quantum state of the electromagnetic field is considered coherent . Consider a one-dimensiona signal with linear polarization. Then operator of the electric field

$$\hat{E}(z,t) = \varphi(z,t)\hat{A} + \text{e.c.} = \varphi(z,t)\hat{A} + \varphi^{*}(z,t)\,\hat{A}^{+} \qquad (4)$$

where $\hat{A} = \int dk\, W(k) a(k)$ - the packet photon annihilation operator, $\hat{A}^{+} = \int dk\, W(k) a^{+}(k)$ - the packet photon creation operator, W (k) – Fourier spectrum of the elementary wave packets $f_{od}(t)$, $\omega = kc$

$$\varphi(z,t) = A\sqrt{\frac{h}{2\tau V}(n+\eta)}\, f_{od}(z,t) \qquad (5)$$

$$< E > = < \alpha \left| \phi(z,t)\,\hat{A} + \phi^{*}(z,t)\,\hat{A}^{+} \right| \alpha > = 2\,\varphi(z,t)\,|\alpha| \cos[\theta] \qquad (6)$$

5. Numerical optimization of the probability of photon absorption by a two-level system excited by an EWP pulse determines the relation of the $(\omega\tau)_{opt}$. parameter and the order of the EWP function n. It turned out to be linear, from where the photon energy is $\varepsilon = (h/2\tau)(n+1+2/\pi)$. In the limiting case $n \gg 1$, the formula takes the usual form $\varepsilon = \hbar\omega$.

References

[3] V. Bykov. Laser Electrodynamics (Cambridge Scholars, 2008.)

[4] V. Ovechko," Femtosecond optics – optics of the elementary wave packets," J. Opt. Soc. Am. B, v.29, 799-805 (2012).

PHYSICS OF MAGNETISM

ENHANCED LONGITUDINAL RELAXATION OF SOLITONS IN ULTRATHIN MAGNETIC FILDS

Ivan A. Yastremsky[1,2], Boris A. Ivanov[3], Denys Makarov[2]

[1]Taras Shevchenko National University of Kiev, 03127 Kiev, Ukraine
[2]Helmholtz-Zentrum Dresden-Rossendorf e.V., Institute of Ion Beam Physics and Materials Research, Bautzner Landstrasse 400, 01328 Dresden, Germany
[3]Institute of Magnetism, National Academy of Sciences and Ministry of Education and Science, 03142 Kyiv, Ukraine

Abstract: *We demonstrate that for ultrathin ferromagnetic films, the contribution of the longitudinal relaxation to soliton damping is comparable to or stronger than any other traditional transversal mechanism, including spin pumping. This finding brings the longitudinal relaxation from being a rather exotic concept, which was thought to be negligible for majority of practically relevant cases, to an important ingredient to tailor dynamics of solitons for modern technology and fundamental physics.*

The relaxation fundamentally determines the operation speed and energy efficiency of spintronic and spinorbitronic devices. The phenomenological theory of the magnetization dynamics was formulated in 1935. The famous Landau-Lifshitz equation in the original form or with Gilbert damping term conserves the magnetization length, allowing only its transversal evolution. Since then, the transversal picture of the magnetization relaxation has become overwhelmingly successful when describing linear magnetic excitations (spin waves) and motion of topologically protected magnetic excitations (magnetic solitons) including domain walls (DWs), bubbles, droplets and recently skyrmions.

Still, in any magnetic system, the change of the magnetization length is allowed [1, 2]. For solitons, the change of the magnetization length, *M*, occurs due to anisotropic magnetic interactions. Arriving at a given location, solitons spend energy to create a deviation (dip) of the magnetization length by the longitudinal (with respect to the magnetization) component of the effective field (Fig. 1)

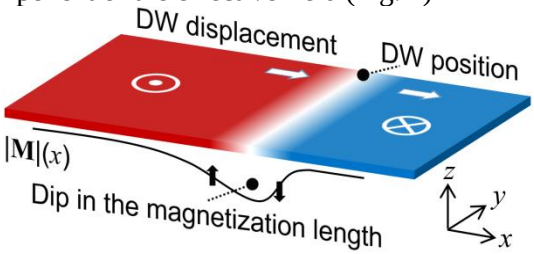

Fig. 1. Longitudinal relaxation is related to the appearance of a dip in the magnetization length, at the location of a domain wall (DW). The dip follows the moving DW. This dip is in the range of $\boldsymbol{\chi_{||}H_K}$, where $\boldsymbol{\chi_{||}}$ is the longitudinal magnetic susceptibility and $\boldsymbol{H_K}$ is the anisotropy field. The dip follows the moving DW. In ultrathin films $\boldsymbol{\chi_{||}}$ is enhanced.

The magnetization length at this location is restored as soon as the soliton moves away. The process of changing the magnetization length is irreversible and leads to the dissipation of energy. Investigations performed for bulk ferromagnets within the Landau-Lifshitz-Bar`yakhtar (LLBar) and the Landau-Lifshitz-Bloch (LLB) equations for solitons without structural suppression of the magnetization (e.g. DWs) sufficiently far from the Curie temperature have not identified any significant contribution from the longitudinal relaxation [3,4]. In bulk materials, up-to now the only two examples are known, where the transversal relaxation picture failed to describe the dynamics of magnetic solitons properly. The longitudinal relaxation dominates the dynamics of solitons at temperatures close to the Curie temperature [5-7]. The motion of Bloch points (with strong structural suppression of the magnetization) is another example where the longitudinal dynamics is important for bulk ferromagnets even far from the Curie temperature [8].

Recently it was identified that the contribution of the so far neglected longitudinal relaxation to the damping of domain walls (without strong structural suppression of the magnetization length) in ultrathin (2D) easy-axis magnetic films sufficiently far from the Curie temperature is comparable or even stronger than any other transversal mechanism discussed before, including spin-pumping [9]. This enhancement is associated

with the Mermin-Wagner theorem and caused by a higher sensitivity of 2D ferromagnets to an effective field compared to their 3D counterparts.

Ultrathin ferromagnetic films support fast moving skyrmions. This paves the way to the realization of prospective racetrack memory concept, the performance of which is determined by the static and dynamic micromagnetic parameters. This memory is potentially more stable to external stimuli compared to widely used SSD memory. The necessity of having strong Dzyaloshinskii-Moriya interactions (DMI) and perpendicular magnetic anisotropy requires utilization of ultrathin magnetic (~1 nm) layers, which possess compromized quality that substantially enhances the magnetic damping for non-collinear magnetic textures.

The finding [9] stimulates the investigation of nowdays technologically relevant skyrmions and merons. In this respect basing on the LLBar equations we generalize the Thiele equation for the case of the longitudinal relaxation. The local relaxation tensor for in the Thiele equation is expressed as follows

$$D_{ij} = \frac{\alpha}{\gamma M}\int \frac{\partial \mathbf{M}}{\partial x_i}\frac{\partial \mathbf{M}}{\partial x_j} dS + \frac{1}{\gamma M \alpha_{||}}\int \frac{\partial M}{\partial x_i}\frac{\partial M}{\partial x_j} dS \quad (1)$$

where γ is the gyromagnetic ratio, α is a local (Gilbert) transversal relaxation constant, $\alpha_{||}$ is a local longitudinal relaxation constant, $M = |\mathbf{M}|$ is a length of the magnetization vector. Correspondingly the first term in (1) is well known result of Thiele and the second term is a longitudinal contribution to the relaxation tensor. In this contribution, we will compare the impact of the longitudinal relaxation mechanism to its transversal counterparts on the motion of magnetic solitons. In particular, the longitudinal contribution increases with a decrease of the transversal relaxation (e.g., the Gilbert constant).

References

[1] L. N. Bulaevskii and V. L. Ginzburg, Temperature dependence of the shape of the domain wall in ferromagnetics and ferroelectrics, Soviet Physics JETP, **18**, 530-535, 1964.

[2] V. G. Bar'yakhtar, *Phenomenological description of relaxation processes in magnetic materials*, Zh. Eksp. Theor. Fiz. **87**, 1501 (1984) [Sov. Phys. JETP **60**, 863, (1984)].

[3] V.G.Baryakhtar, B.A.Ivanov, A.L.Sukstanskii, and E.Yu.Melikhov, *Soliton relaxation in magnets*, Phys. Rev. B **56**, 619(1997).

[4] W.Wang et al., *Phenomenological description of the nonlocal magnetization relaxation in magnonics, spintronics, and domain wall dynamics*, Phys. Rev. B **92**, 054430 (2015).

[5] M. Grahl and J. Kötzler, *Speeding-up and scaling of domain-wall relaxation near T_C of a uniaxial ferromagnet*, Z. Phys B **75**, 527–537 (1989).

[6] J.Kötzler, M.Grahl, I.Sessler, and J.Ferre, *Size and fluctuation effects on the dynamics of linear domain walls in an Ising ferromagnet*, Phys. Rev. Lett. **64**, 2446 (1990).

[7] J.Kötzler, D.A.Garanin, M.Hartl, and L.Jahn, *Evidence for critical fluctuations in Bloch walls near their disordering temperature*, Phys. Rev. Lett. **71**, 177(1993).

[8] E.G.Galkina, B.A.Ivanov and V.A.Stephanovich, *Phenomenological theory of Bloch point relaxation*, JMMM **118**, 373 (1993).

[9] I. A. Yastremsky, J. Fassbender, B. A. Ivanov, and D. Makarov, *Enhanced Longitudinal Relaxation of Magnetic Solitons in Ultrathin Films*, Phys. Rev. Appl. **17**, L061002 (2022).

OPTICAL TUNING OF THE MAGNETIC MODE FREQUENCIES IN Si:YIG

M. O. Popov*, H. L. Chumak*

** Educational and Scientific Institute of High Technologies, Taras Shevchenko National University of Kyiv, Kyiv 01601, Ukraine, e-mail: maxim_popov@univ.kiev.ua, chumak_hryhorii@univ.kiev.ua*

This paper reports the experimental observation of the photoinduced changes in magnetic resonance frequencies of the single–crystal ferrite sample with chemical composition $Y_3Fe_{4.48}Si_{0.52}O_{12}$. The measurements have shown that at room temperature the registered frequency shift is mostly caused by the thermal action of IR radiation. However at liquid nitrogen temperature the observed effect may be safely attributed to the photoinduced variation of magnetocrystalline anisotropy field value, caused by optically activated hopping of conduction electrons between crystallographically equivalent octahedral positions.

Introduction

It is known that in silicon-doped iron-yttrium garnet (further denoted as Si:YIG) single-crystal specimens it is possible to affect the magnetic properties and magnetization configuration of the material by photomagnetic treatment [1,2]. That influence can be explained by using the concept of photoactivated jumps of the weakly coupled electrons between the Fe^{2+} ions in nonequivalent positions. Fe^{2+} ions appear in crystal lattice as a result of partial replacement of trivalent iron atoms in stoichiometric YIG by tetravalent silicon ions during doping and they preferably occupy octahedral crystallographic sites (four such sites per unit cell). The Fe^{2+} ions are strongly anisotropic and their contribution to the net magnetic anisotropy of a crystal is extremely large. If all the sites are populated with equal probability their total contribution to the magnetic anisotropy will compensate each other. If for some reason the population balance between different sites is broken, this causes appearance of a uniaxial magnetic anisotropy. The illumination of the sample with optical of near infrared radiation will cause a photostimulated transitions between different sites due to non-equal probability of photon absorption by electrons on atoms depending of the angle between local axis of symmetry and incoming light polarization [3].

Our work is devoted to the experimental investigation of light irradiation effect on the magnetostatic modes resonance frequencies in disk-shaped specimen of single crystal Si:YIG at both room (300 K) and liquid nitrogen (77 K) temperatures. Since those frequencies depend on magnetocrystalline anisotropy field, and anisotropy field value is sensitive to optical radiation, this substantiates background for the new way to effectively tune the magnetic resonance frequencies by exposing the magnetic crystal to light.

Experimental part.

The sample under investigation was the disk made from Si:YIG with the chemical formula $Y_3Fe_{4.48}Si_{0.52}O_{12}$ cut in such way that disk surface normal corresponds to <110> crystallographic direction. The sample geometrical dimensions were D=2.5 mm, H=0.27 mm. The sample was positioned atop of the short-circuited coplanar microstrip transmission line manufactured from the RT Duroid 5880 laminate (see Fig. 1).

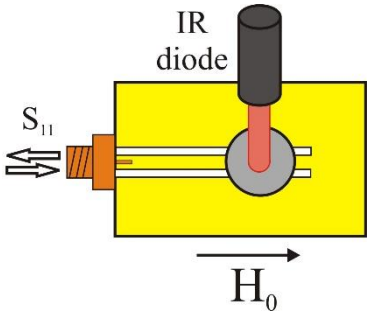

Fig.1 Schematics of experimental set-up for the investigation of optical irradiation influence on the magnetic resonance frequency.

During the experiments the whole structure was subjected to the external bias magnetic field oriented in sample's plane and directed along the transmission line. For the photomagnetic measurements, the disk was illuminated by a focused beam from the 808 nm infrared laser diode. For the cryogenic experiments the microstrip with sample were completely submerged in liquid nitrogen inside a thermo-isolated casing.

The experimentally measures reflection characteristics for the Si:YIG sample measured at room temperature for different laser illumination power are presented on Fig. 2. Besides data for Si:YIG, this figure also contains results for the reference sample with the same dimensions but manufactured from undoped

polycrystalline YIG ($Y_3Fe_5O_{12}$). Since pure YIG does not have measurable amounts of impurity atoms, it is not expected to show photomagnetic response. Comparison between black and red lines in Fig. 2b shows that Si:YIG demonstrates larger frequency shifts, which may be explained by the effect of photoinduced variation of magnetic anisotropy (which is absent in the reference sample). However, the difference between both cases in relatively small, suggesting that thermal heating is responsible for the large part of the net measured frequency change and photomagnetic phenomena accounts for just a fraction of it.

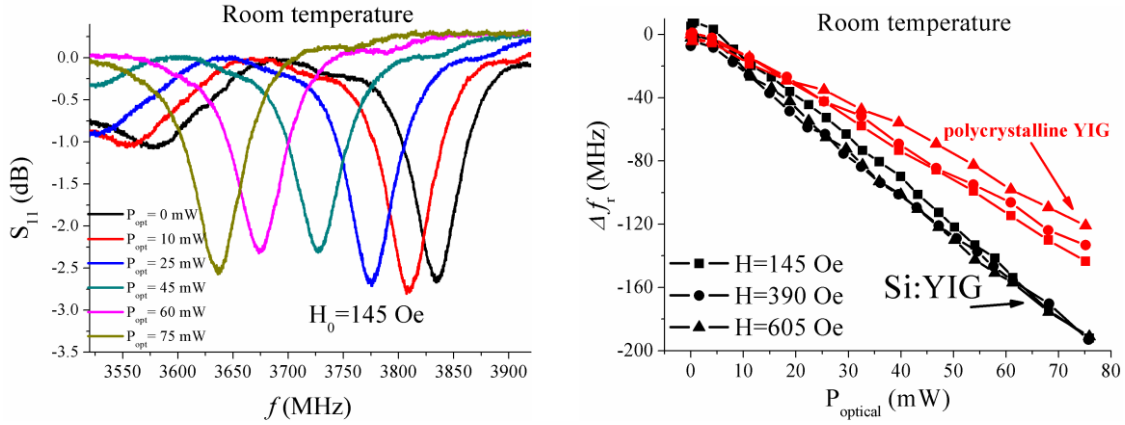

Fig.2. a) Transmission characteristics of Si:YIG for fixed value of bias magnetic field and different laser diode power at room temperature; b) comparison between Si:YIG (black lines) and polycrystalline YIG (red lines).

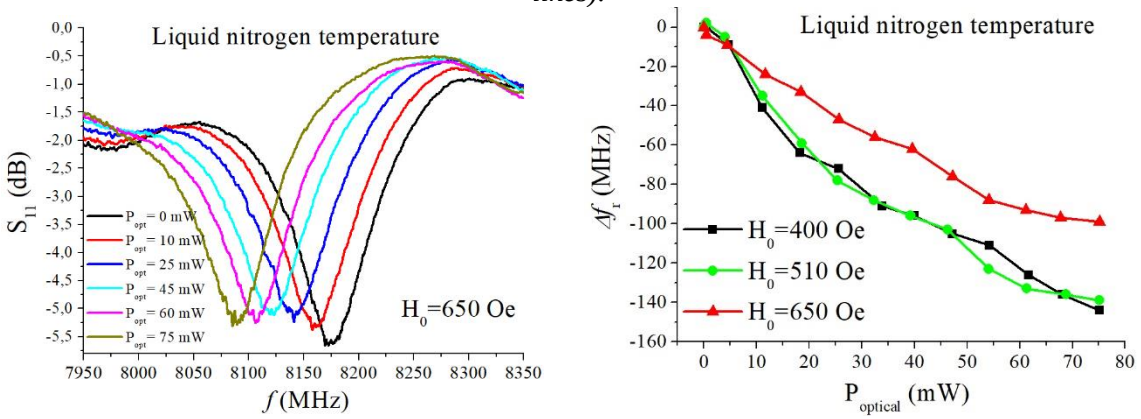

Fig.3. a) Transmission characteristics of Si:YIG for different laser diode power at liquid nitrogen temperature; b) optically induced magnetic resonance frequency shifts in Si:YIG at different values of bias magnetic field.

On the contrary, in the case of liquid nitrogen, the reference sample (polycrystalline YIG) has demonstrated negligible frequency shift (10 MHz at most). Consequently, the registered optically induced frequency change is caused by the magnetooptical effect only. The experimentally measured frequency shift amounted to ≈150 MHz for the applied optical power of 75 mW. This phenomenon provides the background for an optically tunable magnetic devices which may be advantageous in comparison with traditional magnetic field tunable components.

References

[1] V. F. Kovalenko, and E. L. Nagaev, “Photoinduced magnetism”, Sov. Phys. Usp., vol.29, pp. 297–321, 1986.

[2] R. W. Teale, D. W. Temple, and D. I. Weatherley, “Magnetic anisotropy and magnetic anneal in silicon-doped yttrium iron garnet”, Phys. C : Solid State Phys., vol. 3, pp. 1376-1387, 1970.

[3] I. I. Davidenko, S. N. Lyakhimets, and V. F. Kovalenko, “Phenomenological description of spin-reorientational transitions in YIG:Si induced by linearly polarized light”, Phase Transitions: A Multinational Journal, vol. 50, no. 4, pp. 255-263, 1994.

ULTRAFAST PROPAGATION OF NONLINEAR SPIN WAVE THROUGH AN ANTIFERROMAGNETIC MAGNONIC CRYSTAL

***Gorobets, O.Yu., *Kulish, V.V., *Syzon, I.A., *Provolovska, D.V.**
**National Technical University of Ukraine «Igor Sikorsky Kyiv Polytechnic Institute», 37 Beresteisky Ave., 03056 Kyiv, Ukraine, e-mail: provolovska.daryna@lll.kpi.ua*

Analytical model of a nonlinear spin wave (SW) [1] ultrafast propagating through one-dimensional antiferromagnetic magnonic crystal is proposed when the SW velocity exceeds the maximum velocity of linear SW in both antiferromagnets (AFMs) or at least in one of them. Both AFMs that comprise the magnonic crystal are assumed to be two-sublattice uniaxial ones. The Landau-Lifshitz equations have been used in the sigma model with account for the exchange bias between magnetic sublattices of both AFMs, the magnetic anisotropy, the magnetic dipole-dipole interaction and the Dzyaloshynskyi-Moriya interaction. The discrete sets of frequencies and velocities for the considered SW are obtained. The boundary conditions for the Néel vector on the interface between two AFMs are derived with the exchange bias between magnetic sublattices of both AFMs taken into account. These boundary conditions are applied for both fully uncompensated interface and fully compensated one for the illustration purposes. Analysis of the results show that the nonlinear SW is reflectionless, phase-coherent and possess a number of parameters that can be considered as degrees of freedom for encoding information. These findings open up new possibilities of digital data processing utilizing nonlinear SW propagating through antiferromagnetic magnonic crystal in supercritical mode.

Analytical model

Exact solution of Landau-Lifshitz equations are the basis of an analytical model of ultrafast propagation of nonlinear spin wave through one-dimensional antiferromagnetic magnonic crystal. The velocity of spin wave exceeds the maximum velocity of linear SW in both antiferromagnets (AFMs) or at least in one of them.

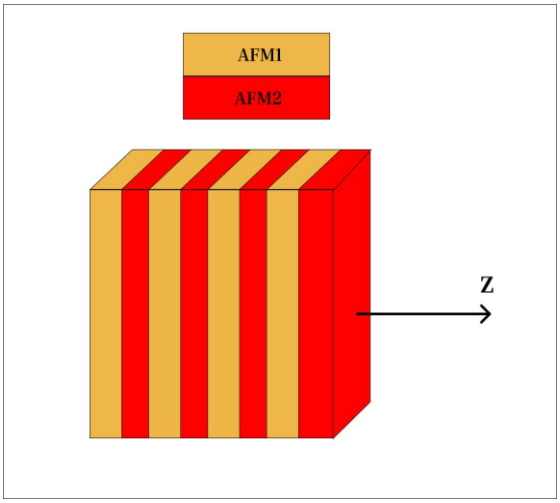

Fig. 1. Antiferromagnetic magnonic crystal studied in the paper.

References

[1] . O. Y. Gorobets and Y. I. Gorobets, 3D Analytical Model of Skyrmion-like Structures in an Antiferromagnet with DMI, J. Magn. Magn. Mater. 507, 166800 (2020).

THE EFFECT OF MAGNETIC FIELD ON RESIDUAL STRESS RELAXATION IN EP-718 ALLOY

Seidametov S.V., Pavlenko D.V., Schetinina M.O., Loskutov S.V., Pravda M.I.
National University Zaporizhzhia Polytechnic, 64 Zhukovskogo str., Zaporizhzhia, 69063, Ukraine, e-mail: stanislav.seidametov@gmail.com

The effect of a pulsed magnetic field on tensile residual stresses in iron-nickel alloy EP-718 (Inconel 718 analog) is investigated. Significant reduction of nearly 40% in residual stress levels is observed in the surface layer of specimens when a pulsed magnetic field is applied. Such patterns are associated with the magnetoplastic effect.

Iron-nickel alloys are widely used in the aviation industry due to their high strength, resistance to high temperatures, oxidation and corrosion, and good machinability. The residual tensile stresses that occur in surfase layer of the parts during their manufacture and operation, as well as during heat and mechanical treatment, are an important factor affecting the strength and durability of constructions, as their high concentration leads to the formation of fatigue cracks. Moreover, the presence of residual stress limits the application of additive manufacturing products. To remove them, thermal [1, 2], mechanical and ultrasonic [3] methods are employed. The most widespread way to relieve residual stresses is heat treatment, which, despite several advantages, has significant drawbacks, such as high energy consumption for heating and structural changes, resulting in a loss of part strength characteristics. From this point of view, the use of a magnetic field is promising. In the laser remelting of Inconel 718 superalloy, the introduction of a transverse static magnetic field resulted in a notable reduction in the compressive residual stress of the remelted region, with the stress decreasing from 392.50 to 315.45 MPa under the effect of the 0.55 T magnetic field [4]. Consequently, the objective of this work is to study the effect of a pulsed magnetic field on tensile residual stresses in the iron-nickel alloy EP-718.

The prismatic specimens of EP-718 (Inconel 718 analog) alloy with dimensions of 59×10×1.9 mm^3 were cut from a sheet produced using conventional technology (GOST 19903-74). The iron-nickel heat-resistant alloy belongs to the austenitic class, and, therefore, is paramagnetic at room temperature.

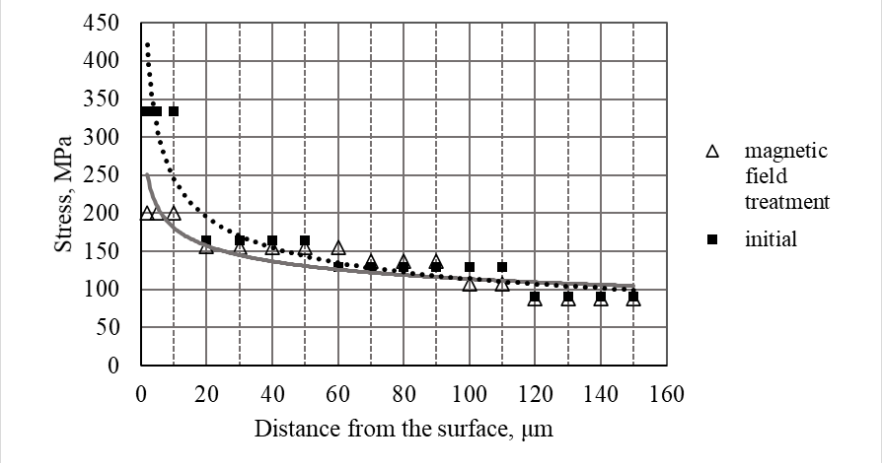

Fig. 1. Residual stress distribution in the surface layer of the specimens

The tensile residual stresses on the specimen surface were formed by grinding on a surface grinding machine and determined by the method of successive removal of metal thin layers by electrolytic polishing using PION-2 device. The electrolyte had the following composition: hydrofluoric acid - 2%; nitric acid - 30%; the rest - water. The deflection of the specimen was recorded by a self-recorder. The mass of the specimen before and after electropolishing was determined using an analytical balance of the ADV-200 type with an accuracy of 0.001 g.

To generate a pulsed magnetic field, the discharge of the capacitor battery of the electrohydro-pulse press model T1220 was used through a copper solenoid. The specimens were treated with a pulsed magnetic field repeatedly (10 pulses) in the mode of charging the capacitor battery to U=5 kV. According to calculations the value of the magnetic field induction of the solenoid, corresponding to this voltage, was 0.37 T. At the same time, the temperature of the specimens, measured using a chromel-copper thermocouple, did not change.

The study's findings (Fig. 1) regarding the residual stress distribution in the surface layer of the specimens reveal that the application of a pulsed magnetic field leads to a decrease in the value of residual stresses at depths up to 20 μm from 334 MPa to 201 MPa by almost 40%. The reduction of residual stresses in a paramagnetic iron-nickel alloy is associated with the rearrangement of the dislocation structure under the influence of a magnetic field, i.e. magnetoplastic effect.

References

[1] S.J. Park, S.-H. Jo, J.G. Kim, et al., "Evolution of microstructure, mechanical properties and residual stress of a cold rolled invar sheet due to heat treatment," *Metals*, vol. 12, 2022, Art. no. 110.

[2] P.E. Aba-Perea, P.J. Withers, T. Pirling, et al., "In situ study of the stress relaxation during aging of nickel-base superalloy forgings," *Metall Mater Trans*, vol. 50A, 2019, Art. no. 3555.

[3] H. Gao, R. K. Dutta, R. M. Huizenga, et al., "Stress relaxation due to ultrasonic impact treatment on multi-pass welds," *Sci. Technol. Weld. Join.*, vol. 19, no. 6, 2014, pp. 505-513.

[4] J. Nie, C. Chen, S. Shuai, et al., "Effect of static magnetic field on the evolution of residual stress and microstructure of laser remelted Inconel 718 superalloy," *J. Therm. Spray Technol.*, no. 29, 2020.

SURFACE PHYSICS, NANO- AND MICROELECTRONICS

INFLUENCE OF AHARONOV-BOHM EFFECT ON HYDRODYNAMIC INSTABILITY OF A TUBULAR ELECTRON BEAM MOVING ALONG SEMICONDUCTOR NANOTUBE WITH DIELECTRIC FILLING

Yu. O. Averkov*, Yu. V. Prokopenko, V. M. Yakovenko***, V. A. Yampol'skii******

** O. Ya. Usikov Institute for Radiophysics and Electronics of the National Academy of Sciences of Ukraine, Kharkiv 61085, Ukraine; Faculty of Computer Science of V. N. Karazin Kharkiv National University, Kharkiv 61077, Ukraine, e-mail: yuriyaverkov@gmail.com*

*** O. Ya. Usikov Institute for Radiophysics and Electronics of the National Academy of Sciences of Ukraine, Kharkiv 61085, Ukraine, e-mail: yurii.prokopenko@nure.ua*

**** O. Ya. Usikov Institute for Radiophysics and Electronics of the National Academy of Sciences of Ukraine, Kharkiv 61085, Ukraine*

***** O. Ya. Usikov Institute for Radiophysics and Electronics of the National Academy of Sciences of Ukraine, Kharkiv 61085, Ukraine; Faculty of Theoretical Physics of V. N. Karazin Kharkiv National University, Kharkiv 61077, Ukraine, e-mail: val.yampolskii@gmail.com*

In this paper, the hydrodynamic instability of a non-relativistic electron beam moving along a semiconductor nanotube with dielectric filling has been investigated. The expressions for dispersion equation of coupled waves of the beam and eigenwaves of the structure under study as well as the increment of instability have been obtained. The numerical calculations show that the dependence of the increment value on the number of quanta of the magnetic flux inside the nanotube oscillates with the period equal to one quantum of the magnetic flux. This can be seen as a manifestation of the Aharonov-Bohm effect.

Introduction

The special feature of the conductive nanotubes is that the area of the electron movement in them is nonsimply connected. This leads to specific effects where the phase of the electron wave function plays the very important role. Such phenomena are the result of the Aharonov-Bohm effect (see [1] and references therein). In recent works [2]-[3], it has been first established that the spectrum of bulk-surface and surface eigenmodes of a semiconductor nanotube with dielectric filling placed in a coaxial constant magnetic field is quntized. This is manifested in oscillations of the number of dispersion branches with the change of the magnetic flux Φ in the nanotube. In Ref. [3], the analytical expression for the electron energy loss due to the excitation of eigenmodes under the Cherenkov resonance condition as well as the analytical expression for the increment of the kinetic instability for the flow of charged particles with the Maxwell distribution of velocities has been derived and numerically analysed. In the present work, we derive and numerically analyse the expressions for both the dispersion equation for the coupled waves of the beam and eigenmodes of the structure under study and the instability increment.

Statement of the problem and main results

Consider a dielectric cylinder of radius ρ_c occupying the space region $0 \le \rho \le \rho_c$, $0 \le \varphi \le 2\pi$, and $|z| < \infty$ (the z-axis is directed along the cylinder axis). We suppose that the cylinder is made of a solid-state isotropic nonmagnetic material with real permittivity ε and there is infinitely thin semiconductor layer on the lateral surface of the cylinder. This structure is placed in the vacuum in a DC magnetic field $\tilde{H}_0$ directed in parallel to its axis. A non-relativistic and monoenergetic tubular electron beam moves in the vacuum along the cylinder, the wall thickness of beam is the same as the distance between this wall and the nanotube surface. Both sizes are much smaller than the length of waves excited by the beam. The set of equations describing the interaction of the bunch and the eigenmodes of the studied structure is the system of Maxwell equations supplemented by the linearized continuity equation for the electrons of the bunch and the nanotube. On the surface of the nanotube, the continuity conditions are met for the tangential components of the electric field strength of the coupled waves. At the same time, the electric displacement vector and the tangential components of the magnetic field strength on the surface of the nanotube undergo jumps, caused by the presence of charges and currents on the surface. These charges and currents are associated with the electron beam and the conductive nanotube. The excitation of the structure eigenmodes by the beam occurs when the Cherenkov resonance condition is fulfilled. Following the method used in [2]-[3], we obtain the dispersion

equation for the coupled waves of the beam and the eigenwaves of the studied structure as well as the expression for the increment of the hydrodynamic instability. In Fig. 1, the dependences of the relative increment γ/ω of the hydrodynamic instability (ω is the frequency of the excited wave) and the number N of filled energy levels of the nanotube electrons on the muber $\eta = \Phi/\Phi_0$ of the magnetic flux quanta through the nanotube (here Φ_0 is the magnetic flux quantum) are presented. The excited wave is the EH_{11} bulk-surface wave [3].

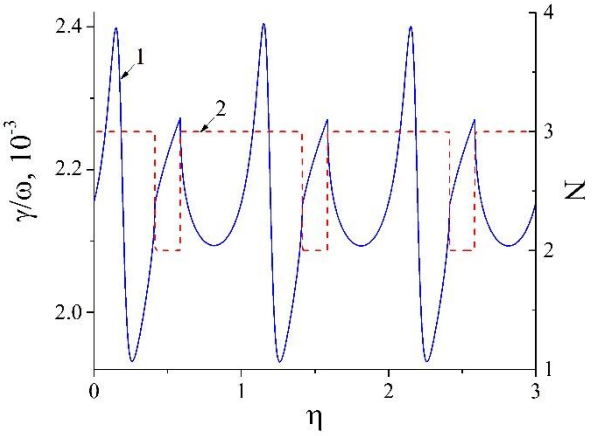

Fig. 1. Dependences γ/ω on η (blue solid curve 1) and $N(\eta)$ (red dashed curve 2)

It is evident from Fig. 1 that both the relative increment γ/ω and the value of N oscillate with growth of η with a period equal to one magnetic flux quantum. It is noteworthy that the highest values of the increment occur with the largest number of N. This result is important to create nanoscale oscilators of electromagnetic radiation without a need to provide an additional feedback in the system.

Authors gratefully acknowledge support from the National Research Foundation of Ukraine, Project No.2020.02/0149 ‘‘Quantum phenomena in the interaction of electromagnetic waves with solid-state nanostructures’’.

References

[1] Yu. O. Averkov, Yu. V. Prokopenko, V. M. Yakovenko, “Semiconductor nanotube eigenmodes and the Aharonov–Bohm effect,” Low Temp. Phys., vol. 48, pp. 32-36, Jan. 2022. DOI: https://doi.org/10.1063/10.0008961.

[2] Yu. O. Averkov, Yu. V. Prokopenko, V. M. Yakovenko, V. A. Yampol’skii, “Aharonov-Bohm effect in the spectrum of eigenmodes in semiconductor nanotubes with dielectric filling in DC magnetic field,” 2022 IEEE 2nd Ukrainian Microwave Week (UkrMW), 14-18 Nov., 2022. DOI: https://10.1109/UkrMW58013.2022.10037076.

[3] Yu. O. Averkov, Yu. V. Prokopenko, V. M. Yakovenko, V. A. Yampol’skii, “Quantum dispersion properties of eigenmodes in semiconductor nanotubes with dielectric filling in dc magnetic field,” Low Temp. Phys., vol. 49, pp. 3-13, Jan. 2023. DOI: https://doi.org/10.1063/10.0016471.

SELF-ASSEMBLY OF LONG RANGE ORDERED ANISOTROPIC SPATIALLY PERIODIC ADSORBATE STRUCTURES ON Mo(112) – A REVIEW

A. G. Fedorus*, A. M. Goriachko, A. G. Naumovets***, D. V. Rumiantsev***
**Department of Physical Electronics, Institute of Physics, The National Academy of Sciences of Ukraine, Prospect Nauky, 46, Kyiv 03028, Ukraine, e-mail: fedorus.gm@gmail.com*
***Faculty of RadioPhysics, Electronics and Computer Systems, Taras Shevchenko National University of Kyiv, Volodymyrska Str. 64/13, Kyiv 03127, Ukraine, email: goriachko@knu.ua*
****Presidium of the National Academy of Sciences of Ukraine, Volodymyrska, 54, Kyiv 01030, Ukraine, email: naumovets@nas.gov.ua*

The Mo(112) surface, which is unreconstructed and strongly anisotropic, can host a wide range of self-assembled adsorbate structures with lateral periodicity along one direction in mesoscopic range. These structures were a subject of detailed experimental investigations for already several decades by the members of physical electronics department at the Institute of Physics of the National Academy of Sciences of Ukraine. Here we review the existing body of experimental data, including those obtained at other institutions, provide a comparizon with the results of theoretical investigations, summarize all discovered physical mechanisms of self-assembly and point out the importance of such studies for modern and perspective high-tech applications.

Mo(112) as a playground for mesoscopic organization of adsorbates

The Mo(112) surface consists of ridges and troughs running in the [11-1] direction. Such structure facilitates the adsorbate atoms' anisotropic diffusion along this direction. In our recent works a number of adsorbates as diverse as Dy, Gd, Sr, Be, O were studied both as single adsorbates and co-adsorbed with each other on Mo(112), see [1-9] and references therein. These studies were performed experimentally by means of low energy electron diffraction (LEED), Auger electron spectroscopy (AES), contact potential difference (CPD) and theoretically by means of calculations within the framework of density functional theory (DFT). A number of ordered and unordered adsorbate phases were discovered, as well as phase transitions among them. The interactions among adatoms, which govern the formation of these phases are as following: direct interactions acting through the vacuum (exchange, van-der-Waals, electrostatic inter-dipole), indirect interactions acting due to the presence of the substrate (Friedel – through the substrate's electron gas, elastic – due to the substrate's outer layer deformation, electrostatic – due to the field between work function spots). A vivid manifestation of these interactions were some particularly outstanding adsorbate phases consisting of 1D atomic chains forming periodic arrays, thus corresponding to 1×n surface superstructures. The values of the integer n were found as high as 9, corresponding to lateral periodicities up to 2.5 nm.

(Ce+O)/Mo(112) System

In view of an ever increasing practical usage of rare earth metals in a wide variety of modern high-tech products (microchips, consumer electronics, nanocatalysts, high density energy storage, nanomedicine, etc) it was decided to continue the studies of rare earth adsorbates on Mo(112). The intriguing results obtained for Dy/Mo(112) and Gd/Mo(112) systems prompted a widening of this research effort, including further rare earth elements. A particular attention was payed to Ce – adsorbed individually or co-adsorbed with oxygen [10]. The (C+O)/Mo(112) has exceeded expectations displaying ordered structures (nanostripes phase) with extremely large (essentially mesosocpic) lateral periodicities between 6 and 11 nm, which, notably can be tuned by varying the amount of adsorbed Ce atoms. This phase is depicted schematically in Fig. 1, along with others appearing in the sequence of equillibrium surface structures as Ce coverage θ increases from 0 to 0.75 ($\theta = c_{Ce}/c_{Mo}$, $c_{Mo} = 8.25 \times 10^{14}$ cm^{-2}). The entire sequence consists of the following stages: island growth at constant mesoscopic periodicity (first order phase transition), growth of mesoscopic periodicity, superperiodic singularity, contraction of the uniform 1st atomic layer of Ce along the direction of ridges and troughs and finally the relaxation of Ce film into a double layer structure.

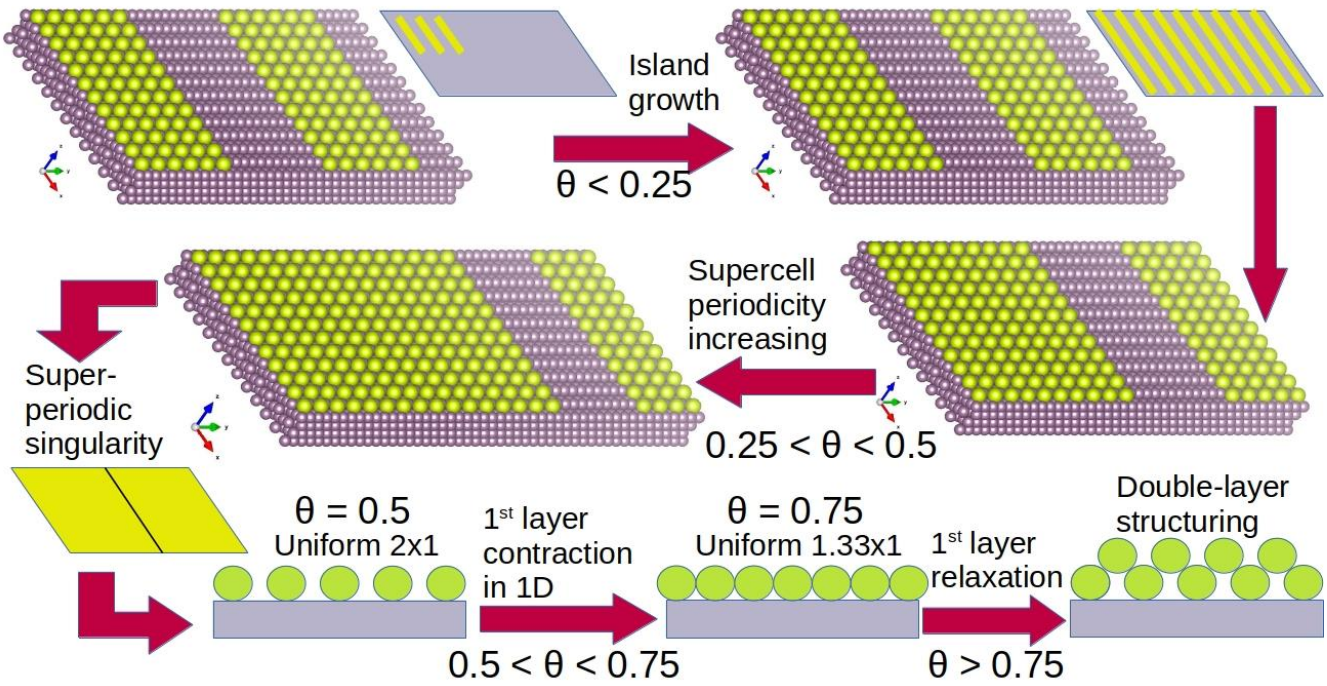

Fig. 1. A schematic diagram of variousequillibrium states of Ce film on Mo(112) for coverages θ < 1.

References

[1] C. Tegenkamp, H. Pfnür, A. Fedorus, A. Naumovets, "Two-dimensional glasses and their concentration dependent re-ordering: Dy on Mo(112)", Surface Science, vol. 601, pp. 978-985, 2007.

[2] A. G. Fedorus, A. A. Mitryaev, A. G. Naumovets, "Irreversible structure transitions in Gd monolayers on Mo(112)", European Physical Journal B, vol.71, pp. 47-54, 2009.

[3] A. A. Mitryaev, A. G. Naumovets, A. G. Fedorus, "Surface alloy formation and two-dimensional vitrification in adsorbed monolayers on Molybdenum (112) surfaces", Low temperature Physics, vol. 36, pp. 677-681, 2010.

[4] A. A. Mitryaev, A. G. Naumovets, A. G. Fedorus, "Surface alloy formation and two-dimensional vitrification in adsorbed monolayers on (112) molybdenum surface", Fizika Nizkikh Temperatur (Kharkov), vol. 36, pp. 854-860, 2010.

[5] A. G. Fedorus, A. A. Mitryaev, A. G. Naumovets, "Beryllium overlayers on Mo(112) and Mo(011) surfaces", Surface Science, vol. 606, pp. 580-589, 2012.

[6] A. G. Fedorus, A. A. Mitryaev, A. G. Naumovets, "Adsorption of oxygen on Mo (112) surface precovered with beryllium: Formation of overlayer and electronic properties", European Physical Journal B, vol. 86, 477, 2013.

[7] A. G. Fedorus, A. A. Mitryaev, A. G. Naumovets, "Interaction of oxygen with submonolayer beryllium films on Mo(112)", EPJ Applied Physics, vol. 68, 21302, 2014.

[8] T. V. Afanasieva, A. G. Fedorus, D. V. Rumiantsev, I. N. Yakovkin, "Honeycomb BeO monolayer on the Mo(112) surface: LEED and DFT study", Applied Surface Science, vol. 428, pp. 815-818, 2018.

[9] T. V. Afanasieva, A. G. Fedorus, A. G. Naumovets, D. V. Rumiantsev, "Coadsorbed oligolayers of beryllium and oxygen on molybdenum (112) surface: Formation and chemical composition, atomic structure and evaporation", Surface Science, vol. 682, pp. 14-24, 2019.

[10] T. V. Afanasieva, A. G. Fedorus, A. M. Goriachko, A. G. Naumovets, I. M. Neporozhnii, D. V. Rumiantsev, "Mesoscopic self-ordering in oxygen doped Ce films adsorbed on Mo(112)", Surface Science, vol. 705, 121766, 2021.

SCANNING TUNNELING MICROSCOPY / SPECTROSCOPY OF METALLIC NANOCLUSTERS DEPOSITED ON THE GERMANIUM (111) SURFACE

Andrii Goriachko*

**Faculty of RadioPhysics, Electronics and Computer Systems, Taras Shevchenko National University of Kyiv, Volodymyrska Str. 64/13, Kyiv 03127, Ukraine, email: goriachko@knu.ua*

The results of experimental investigation by means of ultra-high vacuum scanning tunneling microscopy /spectroscopy (STM) / (STS) of platinum-iridium alloy nanoclusters on an atomically clean Ge(111)-c(2×8) semiconductor substrate are reported. The obtained tunneling spectra in the normalized derivative representation show clear differences in an electronic structure between the pure germanium substrate and metallic nanoclusters, namely the presence and the absence of the band gap correspondingly.

Introduction

Germanium is an important semiconductor material for advanced nanoelectronic applications and is currently of great interest for spatially resolved electronic structure investigations. Scanning tunneling spectroscopy (STS) is an ultimate choice to conduct such investigations and had been employed to study the structure of both valence and conduction bands of the Ge(111) surface [1-2]. Also, using a scanning tunneling microscopy (STM) technique, it is possible not only to investigate but also create metallic nanostructures placed on atomically flat semiconductor surface with almost an atomic precission [3]. Therefore, the goal of the present work was to create such nanoclusters on the Ge(111)-c(2×8) atomically clean substrate and to study their electronic structure by means of STS.

Experimental

All experiments were performed in an ultra-high vacuum chamber with a base pressure of 3×10^{-10} mbar. A standard procedure applied for prepairing the Ge(111) surface in atomically clean state, which in thermodynamic equillibrium is reconstructed and characterized by the c(2×8) superstructure, was described elsewhere [4]. Metal nanoclusters were deposited at 300 K on such a substrate from the STM tip by means of a field evaporation technique as described in the previous work [3]. All STM images were obtained in the constant current mode. The STS measurements were performed by means of STM tip positioning above the location of interest on the sample's surface, stabilizing the tip-sample separation as in the constant current mode for the tunneling current typically in the range from 0.1 to 1 nA, cutting off the STM feedback circuit, sweeping the tunneling voltage in the desired range and simultaneously registering the tunneling current with an analog-to-digital convertor (ADC) and finally reestablishing the feedback loop in order to promptly regain the control over the tip-sample separation. One tunneling spectrum was typically obtained within some fraction of a second. All STM and STS measurements were performed at 300 K. Any processing of the obtained spectra was performed digitally using the raw data recorded in computer memory. Most common processing included smoothing of the spectra by means of simple interpolation between nearest neighbor data points and differentiation, also using nearest neighbor finite differences.

Results and Discussion

Fig. 1 shows the typical STM images and STS results. In a) one can observe an area on the sample where the tip material ($Pt_{0.8}Ir_{0.2}$ alloy) was locally field evaporated on the surface. The deposited material has formed a clearly noticable metallic nanocluster of irregular shape and characteristic lateral size of several dozen nm and several nm in height. Panel b) is an atomically resolved STM image of a smaller area of the sample, which was not covered by the cluster, where one observes the typical atomic arrangement within the c(2×8) surface superstructure of the pure Ge(111). The tunneling spectra were obtained on top of the nanocluster in a) and over the clean germanium substrate in b). The corresponding I(V) curves are shown in panels c-d) and they depict a basic exponential dependence of tunneling current on tunneling voltage, as expected for the tunnel junction. Please note, that in order to keep the tunneling current within the dynamic range of the ADC the tunneling voltage had to be kept between -2500 mV and 2500 mV for the case of the metallic nanocluster, which is a narrower range than between -3000 mV and 3000 mV for the case of the pure semiconductor substrate.

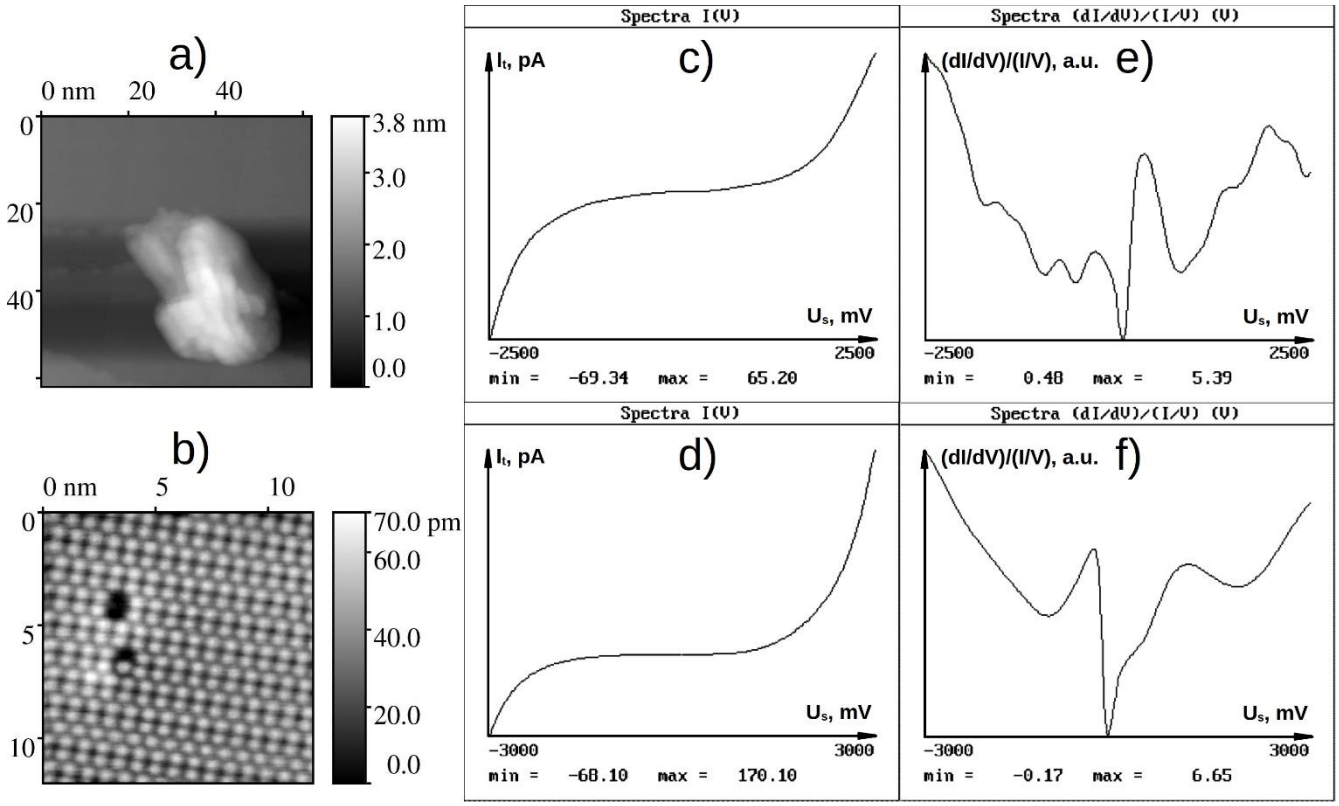

Fig. 1. The results of STM/STS investigation of the $Pt_{0.8}Ir_{20}$ nanocluster on the Ge(111)-c(2×8) substrate. STM images: a) 62 nm × 62 nm area of the substrate containing the nanocluster of irregular shape, tunneling voltage applied to the sample U_s = +2.0 V, tunneling current I_t = 0.3 nA; b) 12 nm × 12 nm area of atomically pure Ge(111)-c(2×8), U_s = +2.0 V, I_t = 0.3 nA. Tunneling spectra: c) spectrum obtained on top of the nanocluster shown in image (a); d) spectrum obtained on the area shown in image (b). Normalized derivatives of the tunneling spectra: e) obtained from the spectrum shown in (c); f) obtained from the spectrum shown in (d).

No spectral features are discernible on the unprocessed I(V) spectra in panels c-d), however they are vividly exposed at the normalized derivative plots, see panels e-f). These plots show a clear band gap in the case of pure Ge(111) and a clear metallic character in the case of an artificial metallic nanocluster.

References

[1] R. M. Feenstra, S. Gaan. G. Meyer, H. Rieder "Low-temperature tunneling spectroscopy of Ge(111)c(2x8) surfaces", Phys. Rev. B, Condensed matter, vol. 71, 125316, 2005.

[2] R. M. Feenstra, J. Y. Lee, M. H. Kang, G. Meyer, K. H. Rieder "Band Gap of the Ge(111)c(2x8) Surface by Scanning Tunneling Spectroscopy", Phys. Rev. B, Condensed matter, vol. 73, 035310, 2006.

[3] A. M. Goriachko "Scanning probe lithography on Ge(111)-c(2x8) surface", Semiconductor Physics, Quantum Electronics & Optoelectronics, vol. 25, pp. 379-384, 2022.

[4] A. Goriachko, P. V. Melnik, M. G. Nakhodkin "New Features of the Ge(111) Surface with co-existing c(2x8) and 2x2 Reconstructions Investigated by Scanning Tunneling Microscopy", Ukrainian Journal of Physics, vol. 60, pp. 1132-1142, 2015.

STUDY OF THE OXYGEN INTERACTION WITH (001) SILICON SURFACE COVERED WITH PREADSORBED METALS MONOLAYERS

Yaroslav Kulikovskyi*, Yurii Len**

Faculty of Radio Physics, Electronics and Computer Systems, Taras Shevchenko National University of Kyiv, 64/13, Volodymyrska Str., Kyiv, Ukraine, 01601

***kylikyar23@gmail.com**, ****lenyurii21@gmail.com**

Formation mechanisms of oxides on Si(001) surface with the adsorbed monolayer covering adsorbates in a wide range of expositions in the atmosphere of molecular oxygen are studied at room temperature. The oxygen sticking coefficient for the metal-coated surface at room temperature was calculated. The influence of the metal film on the oxidation rate of the silicon substrate has been studied.

1. Introduction

One of the key aspects of the interaction of metals with semiconductors is the interaction of oxygen with the interface between them. Oxide films formed as a result of this interaction can affect the electronic structure and physical properties of semiconductors. The study of the interaction of oxygen with the metal/semiconductor interface is an important area of research in nanoelectronics physics, as it can help to understand the processes occurring on the surface and deep within the semiconductor.

Since such boundaries are commonly found in a variety of devices such as solar cells, transistors, diodes, etc., understanding the physical processes at them can improve the efficiency and functionality of such devices. In addition, research on these topics can help in the development of new materials for the production of electronic devices with high stability and efficiency.

It should also be noted that very little information has been obtained about the interaction of the Metal/Si system with molecular oxygen. The purpose of this work is to study the rate of oxygen accumulation by the surface of Si (001) covered with metal monolayers.

2. Experiment

It is investigated experimentally mechanisms of creation of silicides and kinetics oxidations in systems Si(001)-Cr 1 monolayer (ML), Si(001)-Ti 1ML, Si(001)-Mn 1ML. The study of the system, which consists of a Si (001) substrate and a metal films on silicon surface, was performed in an ultra-high-vacuum installation using AES. More details on the conditions of the experiment can be found in [1].

3. Results and discussion

Formation mechanisms of oxides on Si(001) surface with the adsorbed monolayer covering adsorbates in a wide range of expositions in the atmosphere of molecular oxygen are studied at room temperature.

To determine the rate of oxygen accumulation on the surface of Si (001) coated with Metal, the sticking coefficients of molecular oxygen were calculated. The calculation method is given in [2]. The thickness of the metal film on the surface of the sample was around 0.25 nm. Dependence of the molecular oxygen sticking coefficient on the exposure dose (on the logarithmic scale) are shown in Fig.1. It is clearly seen from Fig.1 that the increase in the exposure of the sample in the atmosphere of molecular oxygen, the sticking coefficient of the molecular oxygen goes to 0. This is due to the increase in the thickness of the oxide film and the subsequent formation of saturated oxide.

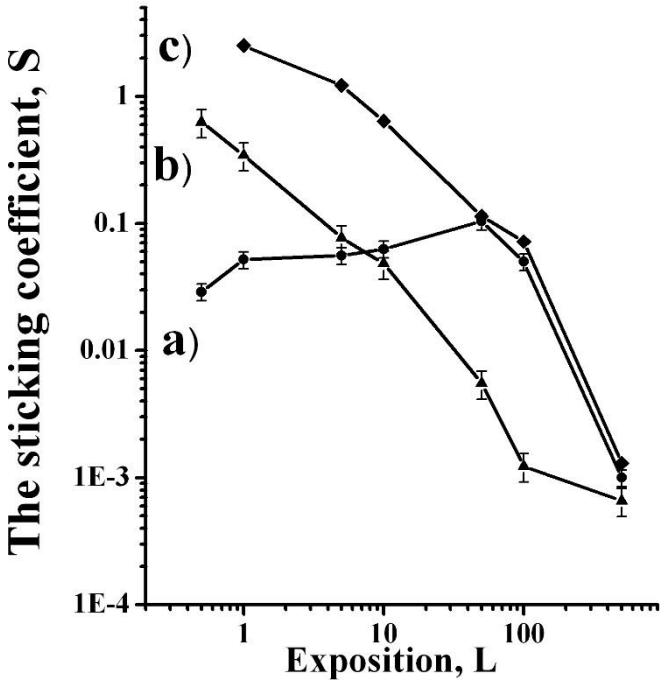

Fig.1 Dependence of molecular oxygen sticking coefficients on exposure on a logarithmic scale Si (001) – Metal 1ML at room temperature: a) Si(001)-Cr 1 ML, b) Si(001)-Ti 1ML, c) Si(001)-Mn 1ML.

It is established that manganese, titanium and chromium monolayer films, adsorbed on the Si(001) surface, at room temperature accelerate the process of silicon oxidation. It was found that titanium on Si(001) surface stimulates the oxidation of silicon surface not so effective as in the case of chromium films. This behavior of the sticking coefficient of indicates that in the system Metal/Si(001) there is an accumulation of oxygen. The oxidation of the sample is accompanied by characteristic changes in the Auger spectra.

Conclusions

As a result of the study of the Metal/Si(001) system, changes in the chemical properties of the surface were observed. The calculated of sticking coefficient and its behavior indicate the interaction of the test sample with molecular oxygen, as well as the possibility of the formation of some metal oxides at room temperature.

References

[1] Butariev K.O. Transformations in Submonolayer Coverages of Chromium and Titanium on Si(001) Surface / K.O. Butariev, I.F. Koval, Yu.A. Len, M.G. Nakhodkin // Journal of nano- and electronics physics (2013) Vol. 5 No 1, 01025(4pp).

[2] Koval I.P. Interaction of molecular oxygen with Si(001) surface covered with a chromium or titanium monolayer / I.P. Koval, Yu.A. Len, M.G. Nakhodkin et al. // Ukr. J. Phys. 2015. Vol. 60, No. 1. - P. 48-53

PHYSICS OF SEMICONDUCTORS AND DIELECTRICS, SEMICONDUCTOR DEVICES

MICROWAVE PROPERTIES OF COMPOSITE MATERIALS BASED ON POLYVINYL CHLORIDE AND OXIDATED ACTIVATED CARBON IN THE MICROWAVE BAND

D.O. Zhytnyk*, V.A. Moiseienko, Yu.V. Noskov***, I.P. Matushko*, O.V. Mischanchuk****, L.M. Grishchenko***

**Taras Shevchenko National University of Kyiv, Kyiv 01601, Ukraine, e-mail: radiodima2000@gmail.com*
***Independent Research & Development Laboratory "200k Electronics", Kyiv, Ukraine, e-mail: vamrpd@gmail.com*
****Kukhar institute of bioorganic chemistry and petrochemistry NAS of Ukraine, Kyiv 02000, Ukraine, e-mail: yuriy.noskov@gmail.com*
*****O.O. Chuiko Institute of Surface Chemistry of NAS of Ukraine, Kyiv 03164, Ukraine, e-mail: bigsnake@i.ua*

Films of composite materials PVC/AC-HNO_3 15% were obtained by the method of thermal pressing of powders of polyvinyl chloride (PVC) and oxidated activated carbon (AC) in different mass ratios. TGA, TPD IR and TPD MS methods were used to determine the concentration and study the thermal stability of oxygen-containing functional groups of AC. The morphology of AC was studied by the SEM method. When comparing the value of the EMW reflectance (S_{11}) of the studied material, a significant dependence of the change in the EMW reflectance value on the concentration of the added AC is observed.

High-frequency electromagnetic radiation and electromagnetic interference can threaten people's health and safety, as well as create serious problems for military and civilian facilities [1]. The rapid development of communication technologies, in addition to the benefits in human life, also led to the spread of strong electromagnetic pollution due to the use of electronic devices [2]. Therefore, the use, development and creation of practical and effective shielding materials becomes extremely important. Carbon materials are used as adsorbents, catalysts, catalyst carriers, they can also be used as an alternative to polymers in the processes of obtaining metal nanoparticles. In addition, carbon materials are widely used as fillers to create a wide class of composite materials for various applications, while their own microwave properties have been investigated very little [3]. At the same time, it is important to use such fillers to create composite materials that are capable of chemical modification. In the literature, there is not enough information on the effect of chemical modification of carbon materials on the ability to interact with electromagnetic radiation, which is important when creating materials with predetermined properties. The search for correlations between the composition of the carbon material, the nature and concentration of surface functional groups, its own physicochemical properties and the properties of the final product (composite material) is important for understanding the mechanisms of its interaction with electromagnetic radiation when creating materials with adjustable properties.

The purpose of this work was to obtain composite materials (CM) based on polyvinyl chloride (PVC) and a carbon-containing filler and to study the effect of oxidation of the latter on the ability of the obtained CM to interact with electromagnetic radiation in the ultra-high-frequency range.

Activated carbon made from apricot pits, the technology of which was developed at the Institute of Sorption and Problems of Endoecology of the National Academy of Sciences of Ukraine, with particle sizes of 0.5–1 mm, was used as the starting material. It has a large specific surface and a developed porous structure (Fig. 1). The main parameters of the initial samples of AC: sorption volume of pores by water V_S = 0.41 cm^3/g, specific surface area S_{sp} = 1350 m^2/g. The initial treatment of carbon was carried out by deashing with the help of repeated washing with HCl solution (3%). Then the samples were washed with distilled water until the pH of the washing water was 5.5–6.0. Oxidation with nitric acid was carried out as follows: the original AC was boiled with a solution of nitric acid in a sand bath for 2 hours with a reflux condenser in the ratio: per 2 g of carbon - 60 ml of 15% HNO_3, then the carbon was washed to neutral pH of washing water and air-dried in an oven at 120°C. The studies of the AC samples were carried out by thermogravimetric analysis (TGA) with IR spectroscopic registration of desorption products (TPD IR). The thermal stability was investigated in an argon atmosphere, at a flow rate of 50 ml min^{-1}, using a heating rate of 10°C min^{-1} in the temperature range of 30–

800°C. The thermal stability of AC samples was also studied by the TPD MS method, using the same heating rate and temperature range in which the studies were conducted as for the TGA method. The surface morphology was observed by scanning electron microscopy (SEM) using a Tescan Mira 3 LMU instrument with an acceleration voltage of 10 kV. To study the microwave properties, the microwave reflection (S_{11}) and microwave losses (S_{21}) were measured with a network analyzer (NA) consisting of generator and indicator blocks in the frequency range of X-band (8 – 12 GHz).

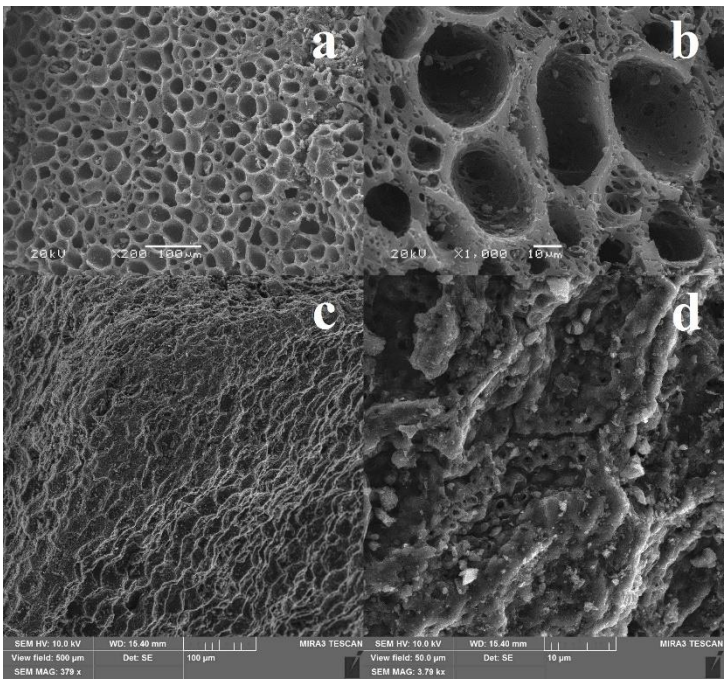

Fig. 1. SEM images of initial (a,b) and oxidated (c, d)

When studying the AC surface by the SEM method, it was established that the outer surface of the initial carbon granules contains mostly round channels of different depths with an average size of 20-30 μm, which are surrounded and/or contain a structure of smaller channels of 1-2 μm in size (Fig. 1 a, b). For the sample oxidated by nitric acid (Fig. 1 c, d), significant changes in surface morphology are observed - it becomes smoother, the shape of large channels changes, they lose their original round shape. The number of small holes in each large channel is significantly reduced, and in some cases they disappear completely. Therefore, oxidation with concentrated nitric acid is a rather aggressive method of modifying the surface layer of carbon materials, which leads to the destruction of the microporous structure of carbon.

Using TGA, TPDIR and TPDMS methods, it was established that as a result of oxidation, various oxygen-containing groups are formed on the carbon surface: carboxylic, anhydride, lactone, and phenolic groups, which are desorbed from the carbon surface in the form of CO and CO_2.

A series of samples of PVC/AC-HNO_3 15% composite materials were obtained in the form of films by the method of thermal pressing of polyvinyl chloride (PVC) powders and activated carbon in different mass ratios (0.2-30 wt% of AC-HNO_3 15%). First, carbon was ground in a mortar. Next, 0.2 g of PVC powder was mixed with the required amount of carbon. This mixture was ground by hand in an agate mortar to a relatively homogeneous state. Then it was poured into a mold on a polyamide substrate and 70 mg of dibutyl phthalate (plasticizer for PVC) was dripped. Then it was pressed at 175°C and a pressure of 10 MPa with a 1-minute holding time. All studied samples of pure and modified PVC had a thickness of 0.25 mm.

Table

Reflection of EM waves S_{11} and losses S_{21} for PVC/AC-HNO_3 15% composite material in the X-band.

Sample	S_{21}, dB			S_{11}, dB		
	Mean	Min.	Max.	Mean	Min.	Max.
PVC	-0.2	-0.4	-0.1	-22.1	-23.1	-21.1
PVC/AC-HNO_3 0.2 wt%	-0.1	-0.2	-0.1	-22.2	-23.0	-21.5
PVC/AC-HNO_3 0.5 wt%	-0.1	-0.2	-0.1	-21.9	-22.9	-20.9
PVC/AC-HNO_3 1.0 wt%	-0.1	-0.2	-0.1	-21.6	-22.5	-20.6
PVC/AC-HNO_3 5.0 wt%	-0.1	-0.1	0	-20.5	-21.4	-19.6
PVC/AC-HNO_3 10 wt%	-0.2	-0.2	-0.1	-18.9	-19.6	-18.3
PVC/AC-HNO_3 20 wt%	-0.7	-0.7	-0.6	-14.3	-14.7	-13.9
PVC/AC-HNO_3 30 wt%	-1.0	-1.0	-0.9	-11.8	-12.2	-11.5

When comparing the value of EMW transmission (S_{21}) through the studied samples, no significant dependence of the change in EMW transmission value on the concentration of added AC is observed. The maximum change in the value of transmission (compared to the original PVC) belongs to the sample with 30% of AC and is 0.8dB. It can be argued that an increase in the concentration of AC leads to a decrease in transmittance, which can be justified by an increase in the specific conductivity of the material under study. It is important to note that the dependence of the amount of passage on the concentration is not monotonic for all studied concentrations of AC and at all frequencies of the X-band, which does not allow us to speak of a certain tendency of such dependence. When comparing the value of the EMW reflectance (S_{11}) of the material under study, a significant dependence of the change in the EMW reflectance value on the concentration of the added AC is observed. The maximum change in the amount of reflection (compared to the original PVC) -10.3 dB belongs to the sample with 30% AC. It can be argued that an increase in the concentration of AC leads to an increase in the reflection value at a concentration of AC greater than 1%, which can be justified by an increase in the specific conductivity of the material under study. The maximum value of the reflection is reached at a concentration of AC of 30% is -11.8dB, and the reflection increases with an increase in the concentration of AC. Therefore, the dependence of the reflection value on the concentration is not monotonic for all investigated concentrations of AC. This is also confirmed by the values of the reflectance value for samples of 0.2 and 0.5%, whose graphs intersect at several points of the X-band.

The obtained results of the study of the amount of EMW reflection from the material can be used for a given change in the reflection of PVC in the X- frequency band for concentrations of AC from 1 to 30%. The results demonstrate a noticeable effect of the AC in the composition of PVC on the microwave properties of the material for concentrations greater than 1%.

References

[1] F. Ruiz-Perez, S. M. Lopez-Estrada, R. V. Tolentino-Hernandez, F. Caballero-Briones, “Carbon-based radar absorbing materials: A critical review”, J. Sci.-Adv. Mater. Dev., vol. 7, iss. 3, p. 100454, Sept. 2022.

[2] Z. Zahid, A. A. Rizvi, ”Estimation of microwave pollution”, Optik, vol. 127, iss. 3, pp. 1307-1311, Feb. 2016.

[3] B. Newman, C. Creighton, L. C. Henderson, F. Stojcevski, “A review of milled carbon fibres in composite materials”, Compos. - A: Appl. Sci. Manuf., vol. 163, p. 107249, Dec. 2022.

ANALYTICAL MODEL FOR A SUBTHRESHOLD SWING IN A MOSFET WITH A SOURCE BASED ON COLD METAL

K.O.Korzh* , M.V.Strikha**
**Taras Shevchenko National University of Kyiv*
Volodymyrska Str. 64/13, 01601 Kyiv – Ukraine, e-mail: korzh.katia14@gmail.com
***Taras Shevchenko National University of Kyiv*
Volodymyrska Str. 64/13, 01601 Kyiv – Ukraine, e-mail: maksym.strikha@gmail.com

In the framework of Landauer-Datta-Lundstrom generalized transport model we obtained an analytical formula for the subthreshold swing in MOSFET with a source fabricated from a cold metal, where the electrons injected into the FET channel has no longer a "hot" Boltzmann "tail" in their energy distribution. It was demonstrated that for such a case the subthreshold swing becomes lower at ambient conditions than the limit value $S \equiv ln10\ kT/e \approx 60$ mV per decade. This effect can be used for the lowering of the voltage supply and for the further MOSFET scaling.

Summary

In the framework of Landauer-Datta-Lundstrom generalized transport model we obtained an analytical formula for the subthreshold swing in MOSFET with a source fabricated from a cold metal.

The subthreshold swing *S* is a fundamental characteristic of MOSFET transistors. It shows how many times the gate voltage V_g must be increased in the subthreshold region in order to achieve an increase in the drain current I_d by an order of magnitude: $S \equiv \ln 10 \frac{dV_g}{d(\ln I_d)}$ [1]. At room temperature in a high-quality transistor with a large value of sub-gate capacitance, the threshold value of this parameter is equal to $S \equiv \ln 10 \frac{kT}{e} \approx 60$ mV/decade, where *e* is the electron charge, *k* is the Boltzmann constant, and *T* is the temperature in Kelvins.

The importance of this parameter lies in the fact that its smallest threshold value determines the minimum possible operating voltage of the transistor supply(Fig.1). Therefore, a decrease in *S* below the fundamental limit would theoretically open up great prospects for further reducing power consumption and scaling transistors.

For this purpose, in particular, it was previously proposed to use the effect of negative capacitance in a ferroelectric that forms the gate dielectric layer. However, the futility of such attempts has been proven on the basis of fundamental thermodynamic principles and numerical calculations of real systems.

Therefore, another, much more physical way to overcome the fundamental limit was proposed: to use a cold metal source for electron injection into the MOSFET channel, where, due to the small width of the valence band, the electrons injected into the channel no longer have a "hot" Boltzmann "tail" in their energy distribution[2-3]. Transistors with a monolayer sub-10-nanometer MoS_2 channel and drain and source on the basis of NbS_2 and TaS_2 with a subthreshold swing below the fundamental limit have already been realized experimentally. However, a visual analytical model that would allow us to estimate the magnitude of the expected effect has not yet been created.

Within the framework of the LDL formalism, we have derived an analytical expression for the subthreshold swing *S*, which implies that *S* is generally somewhat smaller than the fundamental limit, and the degree of its decrease is determined by the ratio of the energy *kT* (26 meV at room temperature) to the value of the energy interval between the top of the valence band of the source material and the value of the surface potential in the transistor channel. The formula can be used to estimate the magnitude of the effect under study in real state-of-the-art electronics systems.

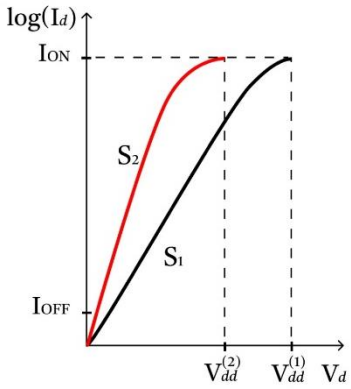

Fig. 1. The output I–V curve of the MOSFET shows the relationship between the supply voltage V_{dd} (corresponding to the maximum current through the drain I_{ON}) and the value of the subthreshold spread S. For the curve with $S_2 < S_1$ we have a decrease in $V_{dd}^{(2)} < V_{dd}^{(1)}$.

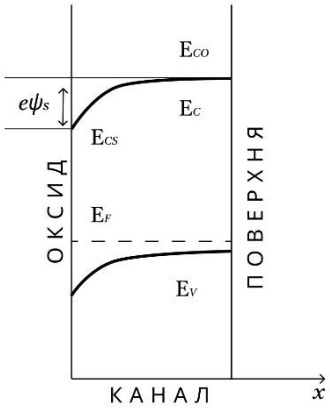

Fig. 2. Energy structure of the conduction channel in the direction perpendicular to the surface.

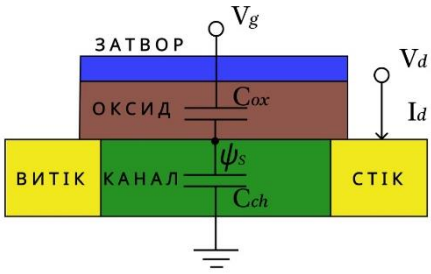

Fig. 3. Capacitive equivalent circuit of a MOSFET transistor.

References

[1] Y.O. Kruglyak, M.V. Strikha. Physics of nanotransistors: structure, metrics and control. Sensor Electronics and Microsystem Technologies. vol. 83, pp. 95-108, Mar. 1961.
[2] R. Landauer. Can capacitance be negative? *Collect. Phenom.*, **2**, 167-170 (1976).
[3] S. Salahuddin, S.Datta. The era of hyper-scaling in electronics. *Nat. Electron.* **1**, 442-450 (2018).

ADHESIVE PROPERTIES OF THE BROKEN SURFACE LAYER OF PZT PIEZOCERAMICS

S.P. Lushchin
National University Zaporizhzhia Polytechnic, 64, Zhukovskogo Street, Zaporizhzhye 69063, Ukraine, e-mail: luschin@zntu.edu.ua

The adhesive properties of the broken surface layer of PZT piezoceramics were investigated. The adhesive strength of the broken surface layer of PZT piezoceramics was determined by the method of normal separation. The value of the film separation wark per unit area of contact with the broken surface layer of PZT piezoceramics was determined. The structure of microparticles of the broken surface layer was investigated by optical microscopy.

Introduction

The quality of work of piezoceramic transducers is largely determined by the condition of the surface of the piezoceramic samples, on the surface of which metal electrodes are applied. The presence on a surface of the PZT sumples the broken surface layer has a negative effect on the quality of metallization, which causes the deterioration of electrophysical characteristics of piezoelectric transducers. The surface broken layer occurs during mechanical treatment in the process of piezoceramic samples manufacturing, as well as a deviation from the technology of making piezoceramics [1]. Analysis of the physical characteristics of particles of this surface layer allows you to take into account their influence on the electrophysical parameters of piezoelectric material and adhesive properties of metal electrodes.

The purpose of the work

The purpose of the work is to investigate the broken surface layer of PZT piezoceramics and to determine its strength properties to improve the quality of metallization of the surface of piezoceramic samples.

Methodology of investigation

Studies of the broken surface layer were perfomed on industrial samples of PZT-36, PZT-19, PZTB-3 (analogue of PZT-4). The separation of the surface layer was carried out with the help of a transparent sticky tape "Scotch". The method of normal separation was evaluated by the adhesive strength of the broken surface layer of the PZT piezoceramics. The microstructure of the surface broken layer was investigated by means of optical microscopy with microscope MIM-8 with a magnification of x100 to x600.

Results and discussion

The adhesive strength of the surface broken layer was determined. Its value was of $\sigma_{tension}$ = 5 kPa. The obtained value of adhesive strength is much less than the mechanical strength of the tension strength of monolithic PZT piezoceramics, which is for PZTB-3 $\sigma_{tension}$ = 21.6 MPa. This fact proves the need to remove the broken surface layer, which can significantly reduce the adhesive strength of the applied metal electrodes.

Work of a film separation per unit area of contact, or adhesion energy, was determined by the formula [2]:

$$W_a = \frac{F_{sep}}{b}(1-\cos\theta),$$

where F_{sep} – the force of separation of the film from the base; b – the width of the film; θ – the angle of the film separation.

The value of the separation force F_{sep} was determined experimentally and was 1.5 N at the width of the film $b = 15 \cdot 10^{-3}$ m. Then the values of the film separation work per unit area of contact are $W_a = 10^2$ J/m^2. This value of the separation can be considered as the energy of adhesion of particles of a broken surface layer of PZT pesoceramics.

The structure of the broken surface layer of PZT piezoceramics is a totality of microcrystallites grains of different sizes. The size of the grains ranges from 1-30 μm. The form of grains is mainly symmetrical - spherical and oval.

Conclusions

The value of adhesive strength of the surface broken layer of PZT pesoceramics is $\sigma_{tension}$ = 5 kPa. The obtained value of adhesive strength is much less than the mechanical strength of the tensile strength of the monolithic PZT piezoceramics, which proves the need to remove the surface of the broken layer to improve the adhesive contact with the electrode. The values of the film separation work per unit area of contact are W_a = 10^2 J/m^2. The structure of the broken surface layer of PZT piezoceramics is a totality of microcrystallites grains of different sizes. The size of the grains ranges from 1-30 μm. The above method of research of the broken surface layer can be used to control the quality of processing of piezoceramic samples in the technology of piezoelectric transducers manufacturing.

References

[1] И.А. Глозман, *Пьезокерамика*. М.:Энергия,1972.

[2] А.Д. Зимон, *Адгезия пленок и покрытий*. М.: Химия, 1977. 352 с.

MICROWAVE PROPERTIES OF COMPOSITE MATERIALS BASED ON POLYURETHANE AND CARBON NANOMATERIALS

D.O. Zhytnyk*, V.V. Trachevskiy, V.A. Moiseienko***, A.N. Zaderko*, L.M. Grishchenko***
** Taras Shevchenko National University of Kyiv, Kyiv 01601, Ukraine, e-mail: radiodima2000@gmail.com*
*** National Academy of Sciences of Ukraine Institute of Macromolecular Chemistry, 48, Kharkivske Shosse, Kyiv, 02155, Ukraine, e-mail: meches49@ukr.net*
**** Independent Research & Development Laboratory "200k Electronics", Kyiv, Ukraine, e-mail:vamrpd@gmail.com*

In this work, composite polymer materials (CPM) based on polyurethane and carbon nanomaterials (CNM) as fillers were obtained. Carbon nanoparticles (CNP) and carbon nanotubes (CNT) were used as nanomaterials. CNP samples were synthesized by the solvothermal method using urea, citric acid, and 3-(trifluoromethyl)aniline. Three types of CNP were synthesized and used as fillers: oxygen-, nitrogen-, and fluorine-containing ones. Carbon nanotubes were obtained by means of catalytic chemical vapor deposition, by pyrolysis of hydrocarbons on complex metal oxide catalysts. The radio-absorbing properties of the obtained CPM in the X-band were investigated.

Wide use of polyurethane composition materials (PCM) is due to the fact that this class of polymers is characterized by a combination of high wear resistance, hardness and strength of the material with good elasticity and adhesion to various substrates [1]. Using monomers or oligomers of different chemical composition, molar mass, structure and functionality in the synthesis of polyurethanes, it is possible to create end products with properties that vary widely from soft and elastic materials to hard and brittle ones.

Higher-order carbon nanostructures with transitional forms of carbon are used as nanosized polymer fillers: fullerenes, fullerites (fullerenes in the crystalline state), astralenes (fulleroid multilayer carbon nanoparticles), single- and multilayer nanotubes, nanofibers, nanocarbon blacks [2]. It is such composites with nano- and micro-sized filler particles that significantly increase the scattering effect of electromagnetic radiation compared to larger metal particles or other types of carbon materials as fillers. Similar composite systems can also be widely used in medicine, as composite pastes, electromagnetic and electronic engineering, etc.

The purpose of this work was to obtain composite materials based on polyurethane (PUR) and carbon nanomaterials *(*CNM) as fillers and to study the interaction of the obtained PCM with electromagnetic radiation in the ultra-high-frequency range (X-band).

In this paper, a polymer composition consisting of polyol (Laprol 3603-2-12), triisocyanate (TT-75) with a ratio of NCO/OH = 1.2 and the required amount of CNM (0.1 – 0.5 %wt.). Schematically, the reaction of polyurethane polymer formation can be represented:

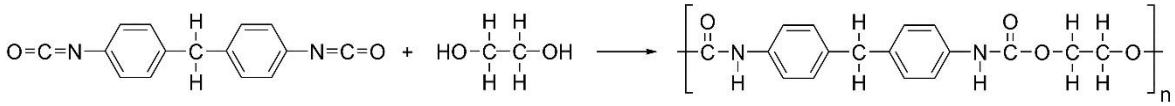

Carbon nanoparticles (CNP) samples were synthesized by the solvothermal method. The methodology of the synthesis is given in detail in the work [3].

Carbon nanotubes (CNT) were obtained by catalytic chemical vapor deposition, by pyrolysis of hydrocarbons on complex metal oxide catalysts. Synthesis of CNT was carried out in equipment with a reactor with a volume of 30 dm^3 and a yield of about 1.5 kg of product per day. According to the Ukrainian standard the average CNT diameter is 10-20 nm, the specific surface, which was determined by argon desorption, is 200-400 m^2/g, bulk density - within 20-40 g/dm^3 [4].

All samples were prepared in the same way in the form of films according to the following technology. For the maximum possible degree of dispersion of agglomerates of nanostructures, the method of ultrasonic

treatment of CNM with simultaneous functionalization of the surface of nanoparticles with a surface-active substance was used. First, carbon nanomaterials were dispersed in isopropyl alcohol with the addition of 1 wt.% carboxymethylcellulose. Then the CNM were dried in a vacuum oven at 75°C. Next, CNM were dispersed in liquid polyol at a temperature of 80°C using ultrasound (22 kHz) for 10 minutes, and triisocyanate was added in the required quantitative ratios. Designation of samples: PUR - original polyurethane, CD3011-oxygen-containing CNP, CDN19-nitrogen- and CDF19-fluorine containing CNP.

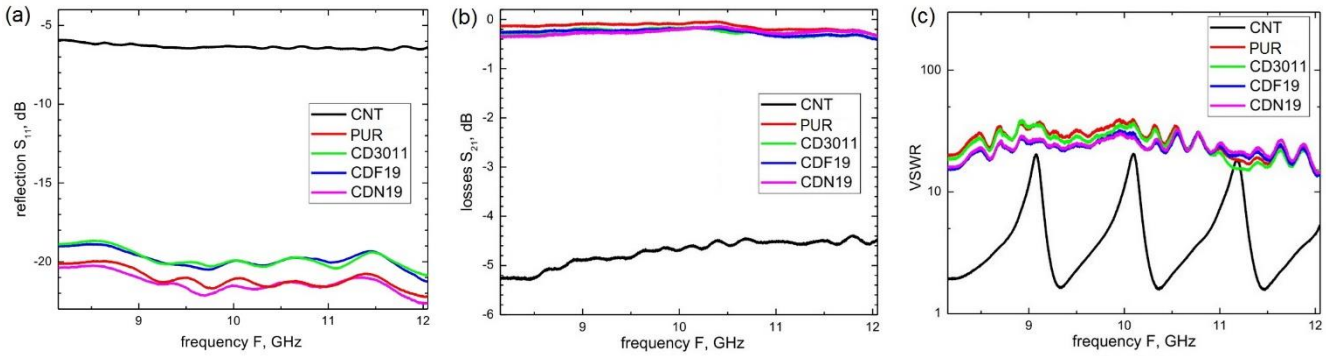

Fig. 1. The results of the microwave properties of the obtained composites

When studying the reflection of electromagnetic signals from the studied materials (Fig. 1. a), it was found that for the CNT sample, the value of S_{11} in the microwave X-band is uniform and equals -6 dB. A better picture is observed for samples: CD3011, PUR, CDN19 and CDF19, for which S_{11} reaches -20 dB. It is worth noting that in the entire investigated X-band, the amount of reflection of electromagnetic radiation is almost independent of the frequency. When studying the absorption of electromagnetic radiation by the materials (Fig. 1. b), it was established that only the CNT material containing carbon nanotubes exhibits significant absorption in the amount of approximately 5 dB or 3 times. For all other materials, absorption does not exceed 5%. The amount of absorption is also uniform in the entire studied frequency band. The measured voltage standing wave coefficient (VSWR) for all samples (except CNT) is of the order of 30 (Fig. 1. c). For the CNT sample, it has a pulsating character depending on the frequency of electromagnetic waves and varies from 1.6 to 20. This behavior of the VSWR value is related to the measurement method , during which conditions are established for the emergence of a standing wave, which leads to the appearance of similar pulsations.

References

[1] A. D. Padsalgikar, “Structure and Properties of Polyurethanes,” in *Applications of Polyurethanes in Medical Devices. Plastics Design Library*. Norwich, NY, U.S.A: William Andrew Publishing, 2022, pp. 43–81. https://doi.org/10.1016/B978-0-12-819673-1.00003-X.

[2] T., Gatti, N., Vicentini, M., Mba, E. Menna, “Organic Functionalized Carbon Nanostructures for Functional Polymer-Based Nanocomposites,” *Eur. J. Org. Chem*., vol. 2016, iss. 6, pp. 1071–1090, Feb. 2016, doi:10.1002/ejoc.201501411.

[3] A. Zaderko, “The process for obtaining of fluoralkylated carbon quantum dots,” Patent WO/2020/121119, Jul. 18, 2020. https://patentscope.wipo.int/search/en/detail.jsf?docId=WO2020121119.

[4] CARBON NANOTUBES. Ukrainian Standard: TU U 24.1-03291669-009:2009 (ISC NAS of Ukraine)].

GAS SENSOR BASED ON THE SPECTRAL SURFACE PLASMON RESONANCE EFFECT WITH COLORIMETRIC REGISTRATION

OLEKSANDR RIABCHENKO, OLEKSANDR KUKLA, ANTON BILETSKIY
V.E. Lashkaryov Institute of Semiconductor Physics of the National Academy of Sciences of Ukraine

Abstract: An optoelectronic gas sensor was developed based on spectral surface plasmon resonance (SPR) in the chromatic mode. It utilized a thin silver film on the prism's base face in the Kretschmann geometry, enabling full visible spectral range SPR. Optical responses were colorimetrically registered using an RGB webcam, eliminating the need for mechanical parts for spectrum acquisition. A laboratory prototype was created and tested for the detection of various organic analyte vapors. The sensor's principle relies on refractive index changes in the surrounding medium, impacting spectral SPR parameters. Additionally, a comparison between pristine and modified silver films with a calixarene-sensitive layer was carried out.
Index terms: spectral SPR, chromatic mode, white light source, optical gas sensor, silver film, colorimetric registration, R, G, B components, visible wavelengths range.

INTRODUCTION

Surface plasmon-polariton resonance (SPR) is a vital tool in sensor tech, detecting gas and biomolecule interactions on thin metal films. The common method involves SPR in Kretschmann geometry, varying the angle of incidence for p-polarized monochromatic light. Changing the medium's properties shifts the resonance angle. Instead of adjusting the angle, we control the reflection spectrum with different wavelengths. This work aimed to develop a gas molecule detection prototype using spectral SPR in a chromatic mode, registering R, G, B components of reflected light.

OPTICAL SCHEME AND EXPERIMENTAL SETUP

The used approach are based on the well-known expression describing the condition for the minimum of internal reflection in the Kretschmann geometry [1]:

$$n_p \sin\theta_{sp} = \sqrt{\frac{\varepsilon_m(\lambda)\varepsilon_d}{\varepsilon_m(\lambda)+\varepsilon_d}}$$

where θ_{sp} – angle of incidence of a *p*-polarized beam with a wavelength λ at which the plasmon resonance is observed, n_p – refractive index of the glass prism, ε_m – real part of the dielectric function of the metal (negative), ε_d – dielectric constant of the medium. As follows from above expression, such a change can be registered using SPR in two ways – either by changing the angle of incidence of light θ_{sp}, at which a minimum of resonance is observed, or by changing the wavelength λ of the incident light at a constant angle of incidence.

As system parameters like prism refractive index, light source, film thickness, and environment remain constant, we determine the plasmon-polariton resonance angle. We achieve this using the freely available WinSpall 3.02 program [2]. In the spectral SPR setup (Figure 1), white light from a Cree XTE Star 3W LED enters through the glass prism's lateral facet. It then goes through a glass plate with a thin silver layer, separated by an immersion layer. A collimator makes the outgoing light slightly divergent. Finally, the spectrum passes through a p-polarizer before reaching the screen.

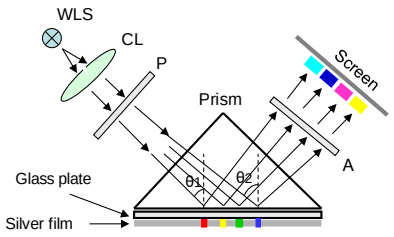

Figure 1: Optical scheme for the implementation of spectral SPR in the Kretschmann geometry: WLS – white light source, CL – collimator, P – polarizer, A – analyzer.

We tested isopropyl, ethyl, and butyl alcohol as organic analytes in a three-stage flow experiment. First, clean air established the equilibrium state. Then, we introduced saturated analyte vapors into the air, and

finally, we purged the cuvette with ambient air. Figure 2 illustrates a typical spectrogram of reflected light, with each point corresponding to R, G, and B parameters.

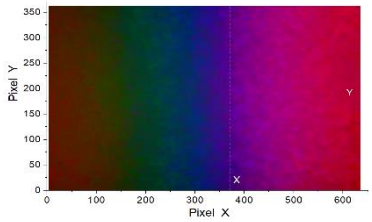

Figure.2: Output spectrum of color bands of reflected light recorded by webcam Logitech C-170 at a resolution of 640x360 pixels (green, blue, magenta and pink bands).

RGB DATA PROCESSING TECHNIQUE

The processing of the obtained color images was performed using software based on the high-level language MATLAB. In order to prevent the influence of light intensity fluctuations on the response ratios, the actual color component values R, G, and B were replaced with the cosine values of the angles α_R, β_G, γ_B of the color vector in the three-dimensional RGB space [3]:

$$\cos\alpha_R = \frac{R}{L}; \quad \cos\beta_G = \frac{G}{L}; \quad \cos\gamma_B = \frac{B}{L}; \quad \text{where } L = \sqrt{R^2 + G^2 + B^2} \tag{2}$$

where α, β, γ – are the angular positions of the color vector with respect to the R, G, B axes, respectively, and L is the absolute value of the color vector in the RGB space. The response signals of individual color components to the gas substance influence were taken as the difference between the corresponding cosines before and after the analyte exposure at the analyzed points of the spectrum. Then the integral response for all three components was calculated as the sum of squared differences of the corresponding cosine values.

RESULTS

Figure 3 shows the curves of integral responses for three investigated types of alcohols.

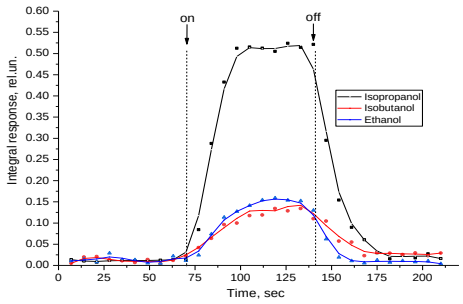

Figure.3. Integrated responses to saturated vapors of isopropanol, isobutyl, and ethanol.

As seen from the figure, the averaged maximum responses were 0.1418 for ethanol, 0.1566 for isobutyl, and 0.5188 for isopropanol. These values correspond to 8%, 9%, and 29.9% of the theoretically maximum response, respectively.

References

[5] Erwin Kretschmann. “The determination of the optical constants of metals by excitation of surface plasmons”, *Zeitschrift für Physik A Hadrons and nuclei*, 1971, 241, pp. 313–324.

[6] Resonant Technologies GmbH. http://www.res-tec.de (accessed 30.06.2023).

[7] O.L. Kukla, A.N. Fedchenko, O.A. Vahula, Yu.M. Shirshov, E.R. Surovtseva. Detection of gas molecules using colorimetric registration under conditions of excitation of SPR in silver films in chromatic mode, *9th International Scientific and Technical Conference "Sensor Electronics and Microsystem Technologies"*, September 20-24, 2021, Odesa, Ukraine, p. 103.

MEDICAL PHYSICS

MODIFIED NANOSTRUCTURED TITANIUM OXIDE ELECTRODES FOR DNA HYBRIDIZATION SENSOR

Schurenko A.I.[1], Khomich V.A.[1], Dobrovolskiy A.M.[1], Mamykin A.V.[2], Doroshenko T.P.[2], Kukla O.L. [2], Grynko D.O.[2,3]

[1] *Institute of Physics, National Academy of Sciences of Ukraine, 46, Nauki Av., Kyiv 03028, Ukraine*

[2] *V.Ye. Lashkaryov Institute of Semiconductor Physics, National Academy of Sciences of Ukraine, 41, Nauki Av., Kyiv 03028, Ukraine*

[3] *Institute of Molecular Biology and Genetics, National Academy of Sciences of Ukraine, 150, Zabolotnogo Str., Kyiv 03143, Ukraine; e-mail: dgrynko@gmail.com*

On the way toward individual gene medicine: observation of DNA hybridization at electrode surfaces modified with thiol-tethered oligonucleotide capture probes and co-assembled with short-chain thiol derivatives requires a careful design of the electrode/electrolyte interface as well as an understanding of the processes at the interface during DNA hybridization. The influence of the pretritment of nanostructured titanium oxide electrode surface potential, redox potential and the ionic strength of electrolyte, are shown to have a significant impact on the impedance spectra and makes it possible to reduce the detection limit of specific nucleic acid sequences to values below pM.

Detection of specific sequences of nucleic acids of pathogens such as viruses and bacteria is very important for the early diagnosis of infectious diseases and the development of effective therapeutic strategies. Also actual are the use of DNA sensors in the field of monitoring human blood banks and the manufacture of medical drugs based on donor blood. Detection of specific DNA sequences in very low quantities may register the aerosol trail of individuals and can revolutionize criminalist examination protocols.

Therefore our research team develops hybridization DNA sensors based on the specific binding of target DNA with corresponding oligonucleotides-probes, previously immobilized on the sensor surface. For the formation of sensor signals, electrical impedance spectroscopy (EIS) is used.

The standard way to increase the sensitivity of EIS is the use of electrodes with developed surfaces and optimized molecular surface coverage. A new low-cost technology for the production of porous nanostructured semiconductor electrodes is proposed [1], which may be the basis for the production of highly informative DNA sensors. Functionalization of such electrodes with a predetermined oligonucleotide provides selectivity of hybridization with the corresponding nucleotide sequence of DNA (target DNA). As a basis for such a sensor used porous film of anodically oxidized titanium with different morphology (nano-tubs with a depth of 0.1 - 7 μm and a diameter of 30 - 60 nm). The technique of immobilization of oligonucleotides on the surface of porous titanium oxide with thiolated oligonucleotides and low molecular weight thiols has been optimized with hydrogen-reducing plasma additional treatment of the semiconductor surface before immobilization.

Achieving dynamic equilibrium between a surface-charged nanostructured electrode and a bio-electrolyte is very important for the technique since the analysis is based on the evolution of the EIS spectrum over time. Using traditional SSC hybridization buffers in contact with modified titanium oxide electrodes was difficult because of long-time surface charging. The use of buffered electrolytes based on Tris and NaCl is more efficient for EIS since the energy of the Fermi level of modified titanium oxide is close to the redox level of Tris in bio-electrolyte.

Observation of oligonucleotide hybridization on molecular-semiconductor electrodes realized with oligonucleotide P1, which is complementary to modPh, on the surface of nanostructured titanium oxide with the immobilized modPh layer. The range of experimentally tested P1 concentrations was 0.1 - 100 nM in Tris-NaCl buffer solution. Peculiarities of interaction are investigated for immobilized probe oligonucleotide modPh with complementary (P1), partially complementary (BCRex14), and non-complementary (npt02) nucleic acid sequences. The use of such electrodes makes it possible to reduce the detection limit of specific nucleic acid sequences to values below pM.

[1] *A. I. Schurenko, V. I. Styopkin, D. O. Grynko, and A. M. Dobrovolskiy*, Self-Organized Anatase-Nanotubes' Array // Nanosistemi, Nanomateriali, Nanotehnologii. - 2020.-V. 18, № 3, P. 529

HARNESSING PHYSICALLY-INFORMED NEURAL NETWORKS FOR NOISE REDUCTION

Sliusarenko D. G.*, Netreba A. V.**
**Faculty of RadioPhysics, Electronics and Computer Systems Taras Shevchenko National University of Kyiv, Kyiv 01601, Ukraine, email: d.fulhem@gmail.com*
***Faculty of RadioPhysics, Electronics and Computer Systems Taras Shevchenko National University of Kyiv, Kyiv 01601, Ukraine, email: avn@univ.kiev.ua*

The concept of developing learning machines that incorporate a systematic consideration of physical laws, along with structured prior knowledge about potential solutions, can be traced back to earlier research that identified a promising technique for effectively applying such prior knowledge. What sets Finite Element Neural Networks (FINNs) apart is their unique approach. Instead of solely relying on data and attempting to derive solutions by approximating sets of input-output pairs using a neural network, FINNs initially consider the underlying physical description of the problem, including partial or ordinary differential equations, in other words, the physics governing the problem. This approach places a strong emphasis on incorporating the physics of the problem, rather than solely relying on data-driven approximations.

Introduction

The uniqueness of PINNS lies in their primary consideration of the underlying physical interpretation of equations involving partial or ordinary derivatives, which encapsulates the physics governing the problem. Instead of attempting to derive a solution exclusively from data through neural network approximations (NS), PINNS models incorporate equations in partial/ordinary derivatives (UCP - PDE/ODU) and their initial/boundary conditions within the learning process, forming what can be described as "soft" networks that account for the physics of the problem through learning losses.
In the realm of applying deep machine learning to create hybrid physical models, there are two main paradigms:

- Physically Informed Neural Networks (PINNS).
- Neural Networks with Physical Constraints (NSFO).

PINNS models encompass equations involving partial/ordinary derivatives (UCP - PDE/ODU) and their initial/boundary conditions, treating them as integral components of the learning process, while NS with physical constraints, often referred to as NS "without data," introduce initial/boundary conditions ("hard" NC) through a user-defined architecture of the NS when incorporating the UCP into the learning loss functions. This soft-form approach is elaborated on in [3], where the term "Physics-Informed Neural Network" (PINN) was coined to describe this methodology.

Proposed methodology and results

A new method of using physical informed network for denoising medical images is proposed. To incorporate physical awareness into the loss function for medical images, the difference between original and reconstructed images can be used based on physical principles. One simple way to do this is to use a loss function that calculates the mean squared error (MSE) between the products of pixel intensities in the original and reconstructed images.

Physical awareness in the context of medical image processing can be expressed through a constraint that is based on physical or biological knowledge about the objects that are represented in the image. In our case, physical awareness can be expressed through the law of conservation of energy. Mathematically, it is possible to describe the loss function considering physical awareness as follows:

Let y represent the original image and ẏ the reconstructed image, both in matrix format, where each element is a pixel intensity.

First, we calculate the mean squared error (MSE) between y and ẏ, which is the standard component of the loss function:

$$MSE = \frac{1}{N}\sum_{i=1}^{N}(y[i] - \dot{y}[i])^2$$

Where N is the number of pixels in the image.

Then we calculate the physical awareness using the difference between the products of pixel intensities on the original and restored images:

$$PhysLoss = \frac{1}{N}\sum_{i=1}^{N}(y[i] \cdot \dot{y}[i])$$

This part of the loss function evaluates the extent to which physical information is preserved in the reconstructed image. It evaluates how well the reconstructed image preserves pixel values and their interactions. The physics weight factor is used to adjust the importance of physics awareness in the loss function. It indicates how important it is to preserve the physical structure of the image compared to conventional MSE. The larger the physics weight, the more weight is given to physics information.

The overall loss function is calculated as a combination of MSE and physical awareness:

$$P = MSE + w \cdot PhysLoss$$

Where w is the physics weight.

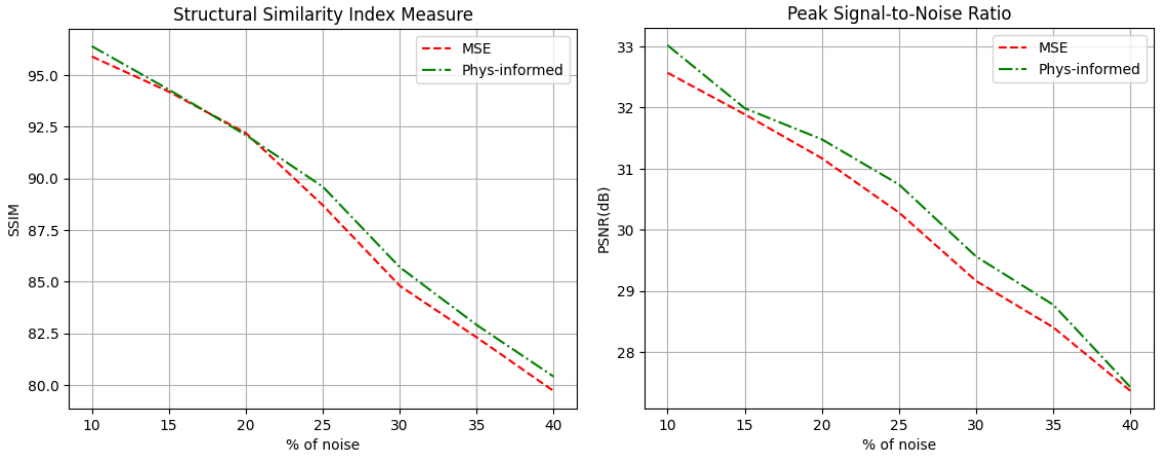

Graph 1. PSNR and SSIM for image denoising with autoencoder(a) and with changed loss-function

Graph 1 (a, b) shows a qualitative assessment of the denoising results using a conventional autoencoder with MSE loss and with a modified loss function, respectively.

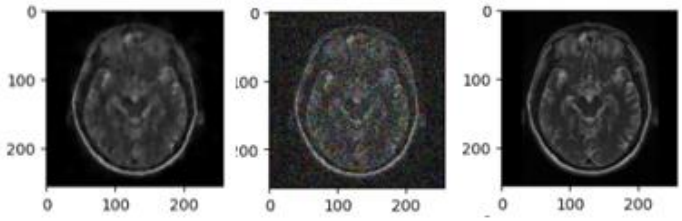

Figure 1. An example of noise reduction. Restored, noisy, original images.

Conclusions

The primary objective was to achieve equivalent or superior results through the utilization of physically informed network when compared to a conventional autoencoder, all while diminishing the quantity of data required for training a new network. Consequently, it became possible to reduce the volume of training data by a factor of 5, while still attaining outcomes that align with those achieved by the autoencoder.

References

1. Thuerey N., et al. Physics-based Deep Learning. arXiv:2109.05237. 2022. Available at: https://arxiv.org/pdf/2109.05237.pdf (accessed 19.05.2022).
2. Emmanouil Xypakis, Valeria de Turris, Fabrizio Gala et al. Physics-informed deep neural network for image denoising, 30 September 2022, PREPRINT (Version 2) available at Research Square [https://doi.org/10.21203/rs.3.rs-2049014/v2]
3. Raissi M., Perdikaris P., Karniadakis G.E. Physics-informed neural networks: A deep learning framework for solving forward and inverse problems involving nonlinear partial differential equations. Journal of Computational Physics. 2019; 378:686-707. doi: https://doi.org/10.1016/j.jcp.2018.10.045

LASER PULSE RADIUS EFFECT ON GENERATION OF RAMAN SCATTERING IN SELF-FOCUSING LOQUID

Oleksandr Mokhonko*, Anatoliy Ivanisik**
**Taras Shevchenko National University of Kyiv, e-mail: sashamohonko@gmail.com*
***Taras Shevchenko National University of Kyiv, e-mail: anatoliyivanisik@gmail.com*

Self-focusing is an important physical phenomenon that is used in various modern optical systems and technologies, such as optical microscopy, laser material processing, and optical telecommunications. The study of self-focusing conditions contributes to a deeper understanding of the phenomena that occur when an optical field interacts with various media, including complex optical systems . In addition, the study of this phenomenon can contribute to the development of new methods and technologies that are used in various fields of science and technology.[1]

Absolute saturation effect

Self-focusing occurs when a high-intensity laser beam is introduced into the optical system, which changes the refractive index of the medium. This can lead to a decrease in the radius of curvature of the wave front, which, in turn, contributes to an increase in the intensity of the beam in the center of the focusing area. [2] It is also experimentally observed that self-focusing depends on the power of the exciting radiation and a number of other factors, however, in practice, a situation sometimes arises when the efficiency stops increasing or even decreases with further power increase. This effect was called the "absolute saturation effect". However, there are situations when the phenomenon of absolute saturation is not desirable and sometimes even harmful. Therefore, the purpose of this work is to consider the dependence of the initial radius of the laser beam on the phenomenon of self-focusing.

The influence of the initial radius of the laser beam

The change in the radius of the laser beam a_z during its propagation through the self-focusing medium can be described as follows (1): [3]

$$a_z^2 = a_0^2 \cdot \left[\left| 1 - \left(z / z_f \right)^2 \right|^{\mu/2} + \left(a_f / a_0 \right)^2 \right], \qquad (1)$$

The modified plane wave approximation was used to calculate the power of Stokes and laser waves at an arbitrary point of the medium with length L and at the exit from the medium at given input powers. During pulse pumping, the energy of pulses, laser $E_{\ell L}$ and Stokes E_{sL} radiation at the exit from the medium was calculated according to the formulas (2) :

$$E_{\ell L} = \int_{-\infty}^{\infty} P_{\ell L}\, dt, \qquad E_{sL} = \int_{-\infty}^{\infty} P_{sL}\, dt, \qquad (2)$$

For the calculation, the parameters typical for the reconstruction of the multimode radiation of a ruby laser in toluene were used: a_0=113 mkm; a_f =5 mkm; λ_ℓ =649,3nm; λ_s=746,3nm; P_{cr}=25 kW; n_0=1,49052; L=25 cm; G=1,17cm/MW. [4] The Wolfram Mathematica program was used to construct the energy dependence. Figure 1 shows the resulting graph of the dependence of the energy of the Stokes pulse on the energy of the laser pulse.

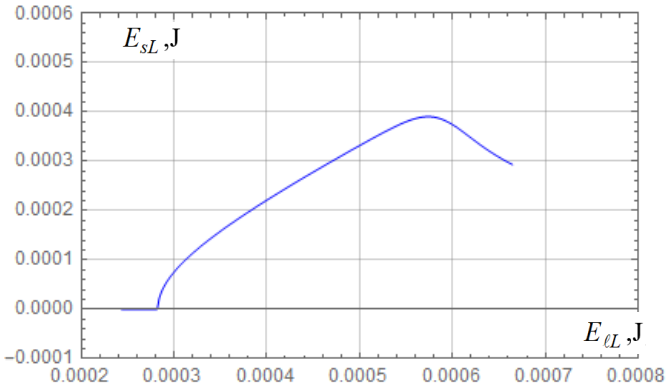

Fig.1. Dependence of the energy of the Stokes E_{sL} *pulse on the energy of the laser* $E_{\ell L}$ *pulse.*

With similar values of the parameters of the experiment, the radius of the initial beam was changed green 120 mkm red 130 mkm Figure 2 shows a comparison of the obtained graphs. It can be observed that with an increase in the radius of the initial beam, the effect of absolute saturation is achieved at higher laser pulse energies.

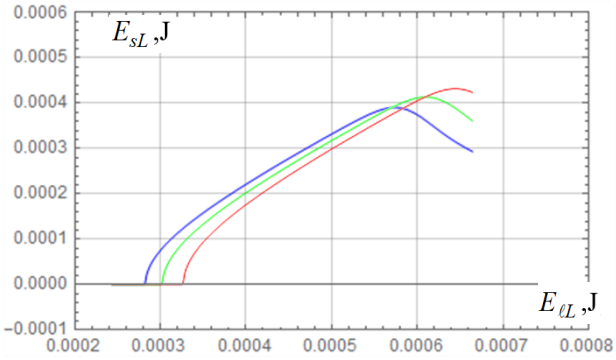

Fig.2. Bependence of energies with different initial radius (blue-113 mkm green-120 mkm red-130 mkm)

The effect of "absolute saturation" is associated with the breakdown of the transformation of laser radiation into a Stokes component at instantaneous pump powers that exceed some fixed value at given parameters, and has nothing to do with pump depletion. Disruption is caused by excessively rigid self-focusing, which leads to a reduction in the length of the focal region.To prevent the effect of absolute saturation in self-focusing conditions, the method of increasing the initial diameter of the pump beam can be used: as the initial diameter of the pump beam increases, its instantaneous power is distributed over a larger area, which reduces the probability of the saturation effect

References

[1] Ding C., Wang Y., Liu Y., Cao W. (2019) Review on stimulated Raman scattering and self-focusing in optical fiber communication systems. IEEE Photonics Journal, 11(4), 1-13.].

[2] . Self-focusing: Past and Present - Fundamentals and Prospects G. Fibich A. L. Gaeta, опублікована "Optics Express" 2015

[3] J. H. Davis and J. R. Cogdell, “Calibration program for the 16-foot antenna,” Elect. Eng. Res. Lab., Univ. Texas, Austin, Tech. Memo. NGL-006-69-3, Nov. 15, 1987.

[4] Ivanisik A. I., Maly V. I., Ponezha G. V. Forced Raman scattering in self-focusing media: new methods of experimental research//Bulletin of Kyiv University: Ser: f.-m. N. -1997. -B.4. -WITH. 239.

BUILDING A SYSTEM FOR RECORDING AND PROCESSING ELECTROENCEPHALOGRAPHIC DATA IN REAL TIME

Roman Piven*, Oleksandr Sudakov**

**Faculty of RadioPhysics, Electronics and Computer Systems Taras Shevchenko National University of Kyiv, Kyiv 01601, Ukraine, email romapivev@knu.ua*

***Faculty of RadioPhysics, Electronics and Computer Systems Taras Shevchenko National University of Kyiv, Kyiv 01601, Ukraine, email* saa@knu.ua

Portable electroencephalographic system for real-time signal recording is described. System may be used for detection and prediction of epileptic seizures.

Introduction

Electroencephalography is a common method of examining the functional state of the brain. The electrical activity of the brain reflects physiological processes in brain structures and the presence of pathological conditions of the central nervous system. Electroencephalography (EEG) is a method of studying brain activity by recording the electrical activity of brain cells recorded on the surface of the head. The research method is based on graphical recording of the received electrical signals and their interpretation [1].

In medicine, an electroencephalogram allows a specialist to see signs of various brain disorders and assess their nature. EEG allows diagnosing any disorders that occur in the brain, that affect its functional activity and change the pattern of electrical potentials generated by it. Among the pathological conditions diagnosed by the EEG method are the following mental development disorders in children sleep disorders OR epilepsy.

Brain interfaces are divided into invasive and non-invasive. Invasive ones are neuroimplants that are implanted directly into the brain, like Neuralink. Non-invasive interfaces are equipment that can be worn and used as ordinary wearable electronics. These are headsets, helmets, etc. that have evolved from equipment cabinets to mini headsets the size of regular headphones. However, the idea of a two-way communication between a computer and a person, which would allow transmitting and receiving signals directly to the brain, has not yet been properly implemented.

EEG operation

The Emotiv EPOC+ signal is measured using a monopolar output circuit, which is carried out by measuring the difference in potentials from one active point - from the electrode on the surface of the scalp over the corresponding brain area and another point, conditionally taken as indifferent. [2]

From the Emotiv Epoc + encephalograph, the signal is transmitted to the Bluetooth chip, which is connected to the Raspberry pi Operating at a frequency of 2.4 Gigahertz, the Bluetooth chip allows for communication within 100 meters. The received signal is transmitted using the CyKit program to the local server. After that, the data is visualized in a browser. From the local server, you can receive a stream of raw data and write it to a file, or send it to other recognition or automatic diagnostic programs (Figure 1).

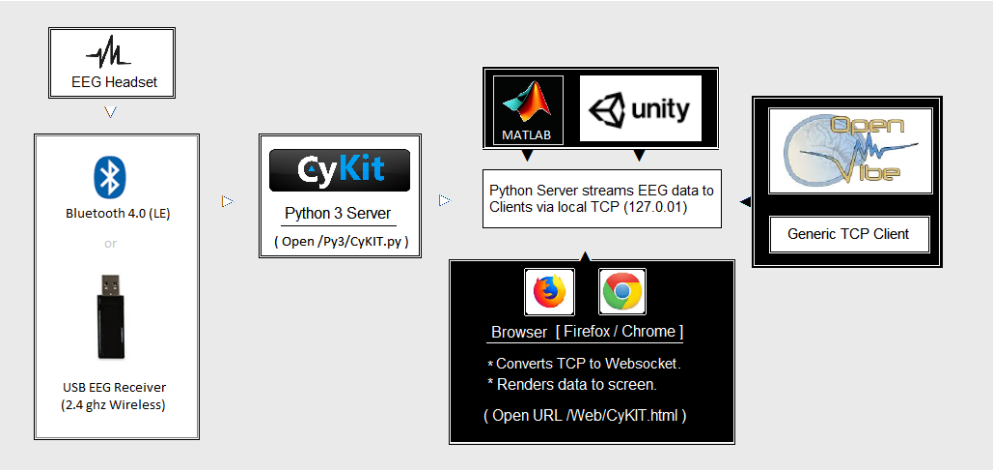

Fig. 1. Program flowchart

During the expert evaluation, it was found that facial expressions have a great impact on the data results. This is clearly shown in the sensor signal (Figure 2). These artifacts can be filtered out by third-party programs, but this was not the purpose of our experiment. Also, dry sensors, displaced electrodes, interference from working devices - all this affects the EEG recording.

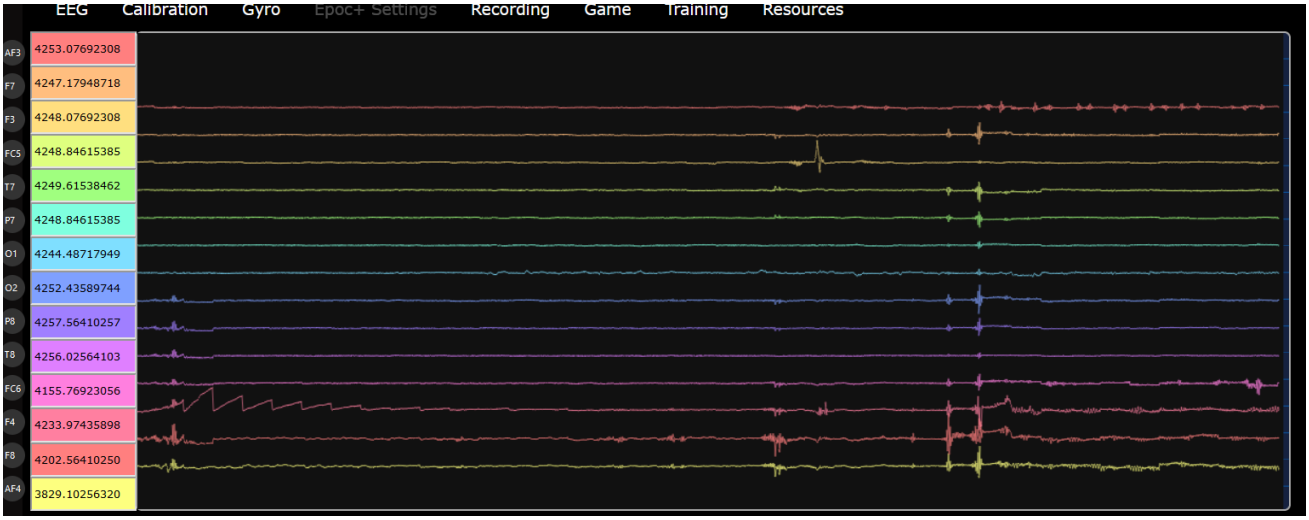

Fig. 2. Data visualization through the browser

The Epoc+ encephalograph can be used to create systems for the real-time processing of electroencephalographic data for the MS Windows operating system which is confirmed by the examples given in this paper. Together with Raspberry PI, running under the Linux operating system, it can be used after fixing Bluetooth problems.

References

[1] Guselnikov V. I. Electrophisiology of the brain, 1976 (in Ukrainian: Гусельников В. І., Електрофізіологія головного мозку. — М.: Вища школа, 1976).
[2] Emotiv Epoc + encephalograph https://emotiv.gitbook.io/epoc-user-manual/introduction-1/about

RESEARCH OF LOW TEMPERATURE REDUCED PRESSURE PLASMA FOR AGRICULTURAL PURPOSES

U. Palianytsia, Yu. Veremii, V. Cherniak, V. Yukhymenko
Faculty of RadioPhysics, Electronics and Computer Systems Taras Shevchenko National University of Kyiv, Kyiv 01601, Ukraine, e-mail: yu.veremii@knu.ua

The work is devoted to a detailed analysis of the composition of low-temperature, low-pressure plasma for agro-industrial purposes. The population temperature of excited electronic levels was determined according to the atomic spectra of Oxygen, the temperature of population of excited vibrational and rotational levels was determined according to the molecular spectra of the Nitrogen second positive system, and the influence of the discharge parameters on the temperature change was shown.

Plasma technology has found widespread applications in various aspects of seed enhancement, such as improving seed scarification, deactivating pathogens, and activating antioxidant systems. These applications have shown clear benefits for enhancing seed quality and seedling establishment in controlled settings like laboratories and greenhouses. Furthermore, optimal exposure to plasma can enhance a crop's ability to withstand stressors like drought, plant diseases, and oxidative stress by altering the seed surface environment through scarification and pathogen inactivation and by stimulating physiological processes like bolstering the antioxidant system and activating defense mechanisms in seeds.

This innovative technology holds great promise for mitigating the negative impacts of environmental stressors on seed germination and seedling growth in agricultural production. However, it's worth noting that current understanding of the effects of plasma applications under stressful conditions is limited, as most studies have been conducted on a limited number of crops in controlled laboratory environments. Further research is needed to comprehensively assess the effectiveness of plasma treatments across a wide range of stressors, particularly in real-world field and greenhouse conditions.

The experimental setup consists of two parts: a system for plasma generation and a spectrometer. The plasma generation system consists of electrodes, the iron container is the external electrode that is grounded. Inside is an electrode to which voltage is applied, which changes with the frequency of the processing chamber. The system is able to reduce the pressure with a pump, so measurements are made at values of 50 Pa and 100 Pa. On this system, a radio frequency discharge is installed, which has the following characteristics: electric current 400 mA - 600 mA, voltage 1200 V. During the experiment, a different frequency of the plasma discharge is adjusted: 20 - 90 kHz. The introduction of light radiation into the spectrometer is carried out with the light guides. To work with the spectrometer, you need to connect it to the light source, connect it to the USB port of the computer and run the PSI-Line control program. The emission spectra of plasma radiation were measured at the experimental setup. Figure 1 shows the measured spectrum taking into account the background component and the sectoral sensitivity of the setup. Lines and bands were identified on the spectrum, where overlap with other spectral lines and bands is absent or minimal.

Ornshtein's method was used to calculate the population temperature of the electronic levels of the measured spectra along the oxygen atomic lines (wavelengths 777 nm, 844 nm, and 926 nm). It was established that the temperature is of the order of Te=4000K±500K, is approximately the same within the margin of error and practically does not depend on the frequency and pressure in the specified values.

To determine Tv, the spectra of N2 (C-B) were simulated in the Specair program in the range of 320–380 nm for different temperatures of the population of excited vibrational levels at a fixed temperature of the rotational levels, and spectral intervals sensitive only to a change in one of the temperatures were determined, and calibration curves were constructed as a function temperature, according to the ratio of unchanged peaks to variable ones. Using the method of overlaying experimental data on the calibration curves, it was determined that the population temperature of the excited vibrational levels is Tv=4500K±500K and slightly increases with increasing pressure.

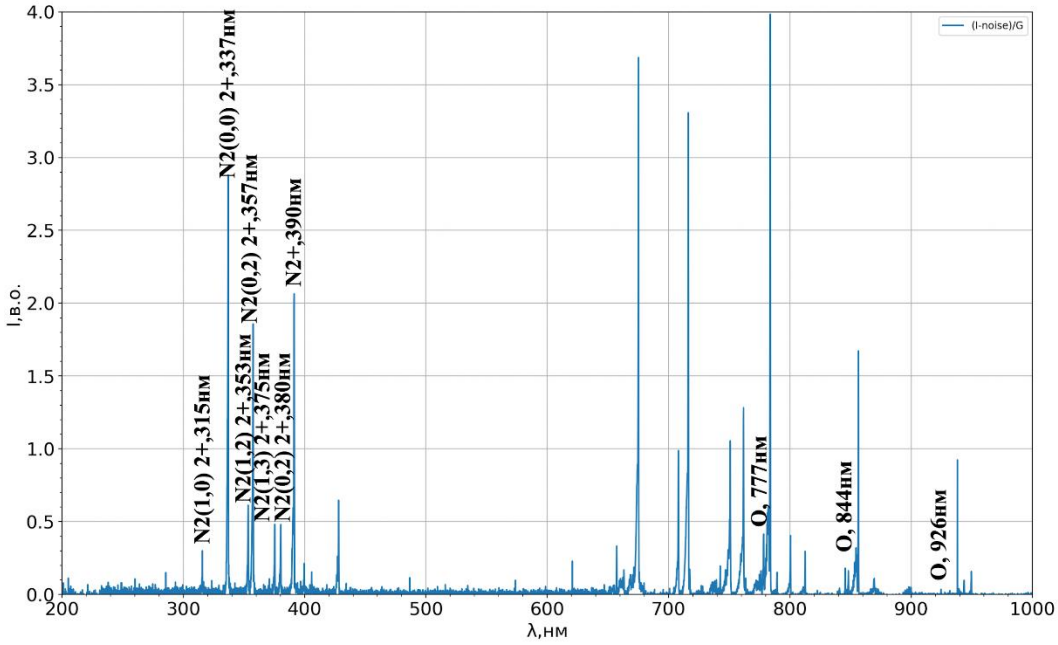

Fig. 1. Measured spectrum

In a similar way, the spectra were constructed for different temperatures of the occupancy of the rotational levels at a fixed temperature of the vibrational levels. Using the method of superimposing experimental data on modeled curves, the population temperature of excited rotational levels was determined and it was established that the temperature of population of excited rotational levels is of the order of Tr ≈300K and weakly depends on the specified discharge parameters. In particular, the temperature decreases with a decrease in pressure.

The obtained results make it possible to understand exactly what processes take place in the plasma-forming gas and how they affect the efficiency in increasing seed germination.

References

[1] Song J-S, Kim SB, Ryu S, Oh J andKim D-S (2020) Emerging PlasmaTechnology That Alleviates CropStress During the Early Growth Stagesof Plants: A Review.Front. Plant Sci. 11:988.doi: 10.3389/fpls.2020.00988

[2] Касабов Г. А., Елисеев В. В. Спектроскопические таблицы для низкотемпературной плазмы: Справочник // М.: Атомиздат. 1973. 160 с.

[3] Specair Version 2.1., http://www.specairradiation.net.

[4] Kramida, A., Ralchenko, Yu., Reader, J., and NIST ASD Team (2022). NIST Atomic Spectra Database (ver. 5.10), [Online]. Available: https://physics.nist.gov/asd [2023, May 4]. National Institute of Standards and Technology, Gaithersburg, MD. DOI: https://doi.org/10.18434/T4W30F

PLASMA PHYSICS

THE INFLUENCE OF SINTERING TEMPERATURE ON THE EROSION RESISTANCE OF Cu-W COMPOSITE MATERIALS

A. Murmantsev[1], A. Veklich[1], V. Boretskij[1]
[1]Taras Shevchenko National University of Kyiv, 63/13, Volodymyrska str., Kyiv 01601, Ukraine
**murmantsev.aleksandr@gmail.com*

This work is a part of wide investigation of interaction of Cu-W composite materials with thermal electric arc discharge plasma. The emission of electric arc discharges plasma between pairs of composite Cu-W electrodes was investigated by optical emission spectroscopy. Electrodes manufactured of Cu-W50 vol.% composite materials by shock sintering technology at temperatures of 750, 850, 950 and 1050°C have been used. Previously determined plasma parameters, such as temperature and concentrations of metal atoms, were used to calculate the equilibrium composition of plasma with copper and tungsten vapour admixtures.

Introduction

Tungsten-copper composite materials find applications in the electrical and electronics industries, such as medium- and heavy-duty electrical contacts, electrodes for resistance welding and electric discharge machining, in the production of microelectronic circuit boards [1-3], etc. Despite their wide popularity and extensive use, there is still ongoing research aimed at enhancing the production technology of these materials. Previous research [4] revealed a connection between the erosion intensity of composite material components (copper and tungsten) and manufacturing technology, specifically the shock sintering temperature. However, such a conclusion has been drawn based on radial distributions of just atoms concentrations.

This study focuses on calculating the equilibrium composition of each type of plasma under investigation to clarify the impact of shock sintering temperature, a technological parameter in composite material manufacturing, on the materials' resistance to thermal erosion caused by electric arc discharge.

Experimental methods

The vertically oriented free-burning arc was ignited in an air atmosphere between the end surfaces of uncooled composite electrodes manufactured on the basis of copper and tungsten (with a volume ratio of 1:1) by the shock sintering method at temperatures of 750, 850, 950, and 1050°C. Electrodes with a square cross-section (5×5 mm) were used. The discharge gap in all experimental studies was 8 mm, the discharge current was kept constant at 3.5 A. The plasma of each type of discharges was investigated by means of optical emission spectroscopy [4]. The excitation temperature of copper atoms (which is equal to the plasma temperature under the assumption of local thermodynamic equilibrium) and concentrations of copper and tungsten atoms have been determined using the Boltzmann plot technique based on the absolute intensities of Cu I and W I spectral lines [5]. These parameters have been used to obtain the equlibrium compositions of discharge plasma between each type of Cu-W composite electrodes by system of equation presented in [6].

Results and Discussion

The radial distributions of the equilibrium compositions of discharge plasma between each type of Cu-W composite electrodes are shown in Fig. 1. One can see that the highest concentretions of both copper and tungsten vapour admixtures is inherent to the plasma of electric arc discharge between electrodes that manufactured at temperature of 850°C. It is also observed that these concentrations decrease with increasing of shock sintering temperature, namely the plasma of arc discharge between composite materials sintered at a temperature of 1050°C exhibit the lowest concentrations of both copper and tungsten vapour admixtures. Thus it can be concluded that the Cu-W composite materials manufactured at the temperature of 1050°C exhibit the highest resistance to thermal action of electric arc discharge plasma and, consequently, erosion resistance. These results confirm the conclusions of previous work [4] that shock sintering temperature in composite material manufacturing affects the total content of metal vapour admixtures in plasma and, consequently, the erosion resistance of the materials. In addition, it is clearly observed, that in plasma of arc discharge between Cu-W electrodes manufactured at temperature of 1050°C the value of concentrations of copper and tungsten

atoms as well as ions are equal. It can be concluded that both components of the composite material, manufactured at 1050°C, evaporate and inject into the plasma in equal amounts.

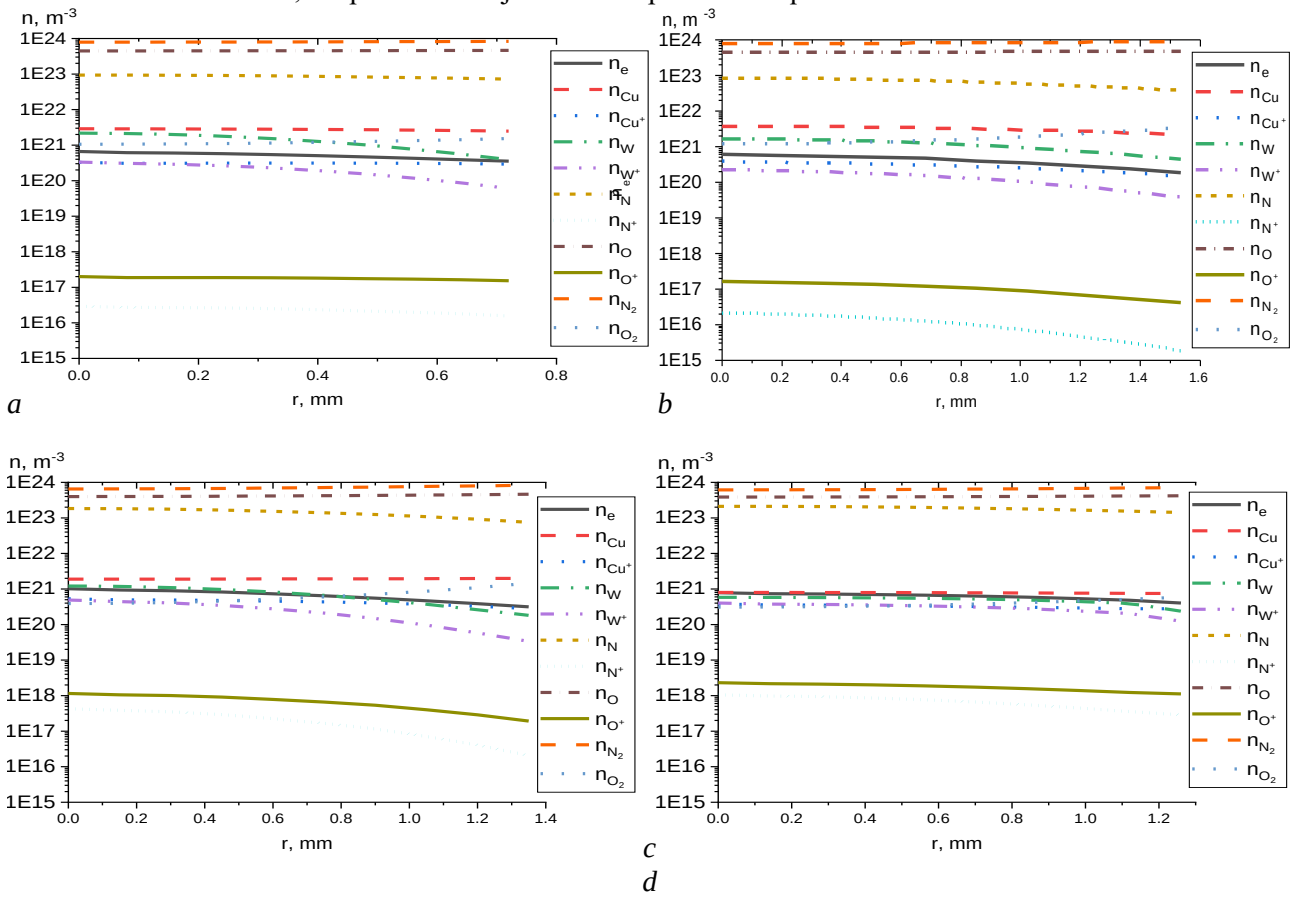

Fig. 1. Radial distributions of equilibrium composition of plasma of electric arc discharges between Cu-W composite electrodes manufactured at shock sintering temperature of (a) 750, (b) 850, (c) 950 and (d) 1050°C

Acknowledgment

This work has been partially carried out within the framework of the EUROfusion Consortium, funded by the European Union via the Euratom Research and Training Programme (Grant Agreement No 101052200 — EUROfusion). Views and opinions expressed are however those of the author(s) only and do not necessarily reflect those of the European Union or the European Commission. Neither the European Union nor the European Commission can be held responsible for them.

The authors are grateful to Dr. Oleksandr Tolochyn from the Frantsevich Institute for Problems of Materials Science NAS of Ukraine for the materials provided under the cooperation agreement.

References

[1] M. Mohammadijoo, S. Kenny, L. Collins, et al. Influence of cold-wire tandem submerged arc welding parameters on weld geometry and microhardness ofmicroalloyed pipeline steels // I*nt J Adv Manuf Technol*. 2017, v. 88, p. 2249-2263.

[2] B. Acherjee. Hybrid laser arc welding: State-of-art review // *Optics and Laser Technology*. 2018, v. 99, p. 60-71. https://doi.org/10.1016/j.optlastec.2017.09.038.

[3] V. Shchitsyn, D. Belinin,Yu. Shchitsyn.Plasma Welding of Aluminum Alloys with the Use of Two Direct ARCS on Reverse-Polarity Current // *Metallurgist*. 2016, v. 59, p. 1234-1237.

[4] A. Murmantsev, A. Veklich, V. Boretskij, S. Fesenko, M. Kleshych, and O. Tolochyn. Investigation of thermal plasma of arc discharge between novel composite Cu-W materials // *Problems of Atomic Science and Technology*. *Series: Plasma Physics (29)*. 2023, v. 143(1) p. 74–78.
[5] A. Murmantsev. Investigation of Spatial Distribution of Metal Vapours Admixtures in The Plasma of an Electric Arc Discharge // *Problems of Atomic Science and Technology*. 2023, v. 146(4), p. 139-146.
[6] I. Babich, V. Boretskij, A. Veklich, R. Semenyshyn. Spectroscopic data and stark broadening of Cu I and Ag I spectral lines: Selection and analysis// *Advances in Space Research*. 2014, v. 54, p. 1254-1263.

EFFECT OF AN GENERATED PUMP ELECTRIC FIELD ON A GROWTH INCREMENT OF THE INPUT SIGNAL IN THE PARAMETRIC SUPERHETERODYNE FREE ELECTRON LASER IN QUADRATIC NONLINEAR APPROXIMATION

Stanislav Ilin, Alexander Lysenko
Faculty of Electronics and Information Technology Sumy State University, Sumy 40007, Ukraine,
e-mail: sequell3@gmail.com

We present our study of the effect of an generated pump electric field on the amplification of the input electromagnetic signal by the parametric superheterodyne free electron laser. We found that this field significantly enhances the input signal growth increment in a wide range of the electron beam energy and input signal frequency. We believe that this advantage of the electrostatic undulator allows us to achive significant amplification of electromagnetic waves with frequencies from a few THz to at least several tens of THz.

Introduction

Free electron lasers (FELs) are devices that generate or amplify the electromagnetic waves over an extremly wide range of frequencies. THz FELs are one of the most important sources of the THz radiation which occupy many areas of human activity. But many of the powerful FELs require a lot of space to be placed, limiting their use in, for example, compact scientific or medical laboratories. Superheterodyne FEL with an electrostatic undulator [1] is one of promising technologies that makes it possible to solve this problem of existing THz FELs while maintaining their power at a sufficient level.

Model

The object of our research is the model of the amplification section of the FEL which you can see on the Fig. 1. This section mainly consists of the magnetic undulator 2 which creates periodic transverse magnetic field, and electrostatic undulator 3 which creates periodically reversible longitudinal electrostatic field. Electromagnetic signal as a planar wave travels in the amplification section passing through the relativistic electron beam (REB) 1. As is known, the interaction of the electromagnetic wave, REB, and a periodic magnetic field leads to the space charge waves (SCWs) excitation in the electron beam. Then the electrostatic undulator field stimulates the growth of SCWs [2] and thus we obtain powerful SCWs, the energy of which is transferred to the initial electromagnetic signal.

Generated pump electric field is the electrostatic field generated by the REB in process of its interaction with the undulator external electric field [2]. This field enhances the total pump electric field by ~33% [2].

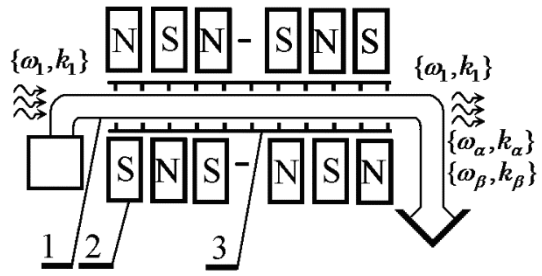

Fig. 1. Scheme of a superheterodyne parametric FEL with a longitudinal electrostatic undulator. Here 1 – electron beam; 2 – magnetic undulator; 3 – electrostatic undulator

Analysis

Delving into our study of the generated pump electric field [2] we researched how this phenomena affects on the input electromagnetic signal and found a few significant effects.

Firstly we reseached the behavior of the dependence of the input signal growth increment Γ on the beam Lorentz factor γ_0 with (Fig. 2 a, curve 2) and without (Fig. 2 a, curve 1) the generated pump electric field under

certain system parameters. We see that generated electric field increases the input signal growth increment by 28% at the γ_0=2.0 and by 10% at the γ_0=4.0.

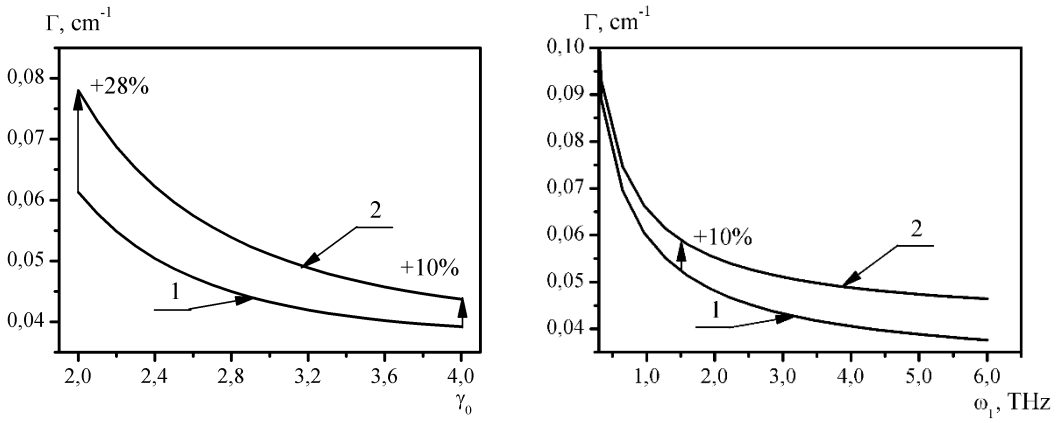

Fig. 2. Dependencies of the growth increment Γ on: electron beam Lorentz factor γ_0 (a); input signal frequency ω_1 (b). Curve 1 defines the behavior of Γ without the effect of the generated pump electric field; curve 2 – with the effect of the generated pump electric field.

Secondly we found similar effect in the dependence of the input signal growth increment Γ on the input signal frequency ω_1 with (Fig. 2 b, curve 2) and without (Fig. 2 b, curve 1) the generated pump electric field. In this case the generated pump electric field gradually increases the signal growth increment. At signal frequency ω_1=1.5 THz the increment Γ with an effect of the generated pump electric field is by ~10% more than the signal growth increment without this effect.

Conclusion

Continuing our study of the generated pump electric field [2], we carried out a comparative analysis of the input signal growth increment when it is amplified with the participation of the electrostatic undulator field without and with an generated pump electric field. We found that the generated pump electric field enhances the overall growth increment and this occurs most effectively at a lower Lorentz factor of the electron beam (by 28% at γ_0=2.0 and the more, the smaller γ_0) (Fig. 2, a) and at a higher frequency of the input signal (by 10% at ω_1=1.5 THz and the more, the more ω_1) (Fig. 2, b).

References

[1] V.V. Kulish, A.V. Lysenko, I.V. Gubanov, A.Yu. Brusnik, Pat. 87750 , Ukraine, MPK(2009): H05H 9/00, publ. 10.08.2009, bull. No 15/2009.

[2] A.V. Lysenko, S.S. Ilin, "Multiharmonic Interactions of Longitudinal Waves in Amplification Section of Superheterodyne Free Electron Laser," J. Nano- Electron. Phys., vol. 14, no. 5, pp. 05006-1–05006-6, 2022

GROWTH AND DIFFUSION OF CLUSTERS IN THE CYLINDRICAL MAGNETRON CHAMBER

O.Yu.Abakumenko, O.A. Demeshko, O.Yu. Kravchenko
Taras Shevchenko Kyiv University, Volodymirs'ka Str. 64, 01601, Kyiv, Ukraine, kay@univ.kiev.ua

Abstract. *The nucleation, growth and diffusion of clusters in cylindrical magnetron chamber are studied at different buffer gas pressures. It is shown that the concentration of metal atoms monotonically decreases with distance from the erosion zone, and the concentration of clusters has a maximum at a certain distance from the cathode. Cluster size distributions are obtained, which show an increase in the number of large clusters with increasing gas pressure.*

Introduction

Metal nanoparticles to be useful for many applications such as antibacterial activities, fluorescence, catalysis, and plasmon-based sensor [1,2]. The unique physical, optical, and chemical properties of nanoparticles are originated from their very high surface-to-volume ratio and the number of atoms in the nanoscale size. Several synthesis techniques have been used to synthesize nanoparticle, including chemical reduction, green synthesis, laser ablation. However, most of them have always struggled with size and shape controllability as well as their aggregation. Therefore, further progress on applications of nanoparticles essentially relies upon the development in synthesis technique to solve such problems.

Recently, in [3] it was reported on growth of metal nanoparticles, using direct current sputtering systems. The metal targets were sputtered onto ionic liquids to form self-assembly of metal nanoparticles on carbon supports in the liquid. This technique reduces the complexity of synthesis processes and facilitates control over size, shape, and aggregation of the nanoparticles. The disadvantage of this method is the low productivity of nanoparticle formation, which requires additional research to increase it.

The purpose of this work is to simulate the process of nucleation and growth of metal clusters, as well as their diffusion in a magnetron discharge chamber.

Model and simulation method

In our model, the magnetron discharge chamber is a cylinder filled with argon under pressure p. From the cathode, which is a round titanium disc, atoms are emitted into the chamber as a result of ion bombardment. As shown in a number of studies, the cathode erosion zone is shaped like a ring. If the concentration of metal atoms in the chamber exceeds the concentration of saturated vapor, clusters may form.

The kinetic equation for the number density f_n of clusters containing n atoms has the form [4]

$$\frac{\partial f_n}{\partial t} = Nk_{n-1}f_{n-1} - Nk_n f_n - \nu_{ev}(n) f_n + \nu_{ev}(n+1) f_{n+1},$$

where N is the number density of free metallic atoms, k_n and $\nu_{ev}(n)$ are the rate constants attachment of atom to a cluster and evaporation of atoms from clusters consisting of n atoms. The rate of attachment has form $k_n = k_0 \cdot n^{2/3}$ within the framework of the liquid drop model, where $k_0 = \sqrt{\frac{2T}{\pi m}}\pi r_w^2$, T is the gas temperature, m is the mass of titanium atom, and r_w is the Wigner-Seitz radius of a bulk material. The evaporation rate can be determined through a constant rate of attachment of atoms based on the principle of detailed equilibrium: $\nu_{ev}(n+1) = k_n N_{sat}(T) \exp\left(-\frac{\varepsilon_{n+1} - \varepsilon_0}{T}\right)$. Here $N_{sat}(T)$ is the concentration of saturated metal vapor at temperature *T*, $\varepsilon_n = \varepsilon_0 - \Delta\varepsilon/n^{1/3}$ is the energy of connecting an atom in a cluster consisting of *n* atoms, $\Delta\varepsilon = 2A/3$, ε_0 is the atom binding energy for the surface, *A* is the specific surface energy of the cluster.

The spatial and temporal distributions of titanium atom density N and cluster number density f_n are described by the diffusion equations

$$\frac{\partial N}{\partial t} - \nabla\left(D\nabla N\right) = \int_2^{n_{\max}} f_n n dn ,$$

$$\frac{\partial f_n}{\partial t} - \nabla\left(D_n \nabla f_n\right) = \left(\frac{\partial f_n}{\partial t}\right)_{col}, \quad n = 2,\ldots n_{\max}..$$

Here D is the diffusion coefficient of titanium atoms in argon, D_n is the diffusion coefficient of clusters, containing n atoms. The right parts in these equations describe the change in particle concentrations as a result of reactions with the formation of clusters, $n_{\max}$ is the maximum number of types of clusters.

Results and discussion

We have simulated the diffusion of metal atoms in a magnetron discharge chamber, as well as the process of cluster formation and diffusion at buffer gas pressure $p = 0.1 - 1 Torr$. The flux density of titanium atoms from the erosion zone of the cathode was $\Gamma_0 = 10^{14}\ cm^{-2}s^{-1}$. Sometime after the start of the injection of metal atoms, stationary distributions of their concentration and the concentration of clusters in space were established.

Fig. 1 shows the spatial distribution of clusters containing five atoms after establishing a steady state under buffer gas pressure $p = 0.5 Torr$.

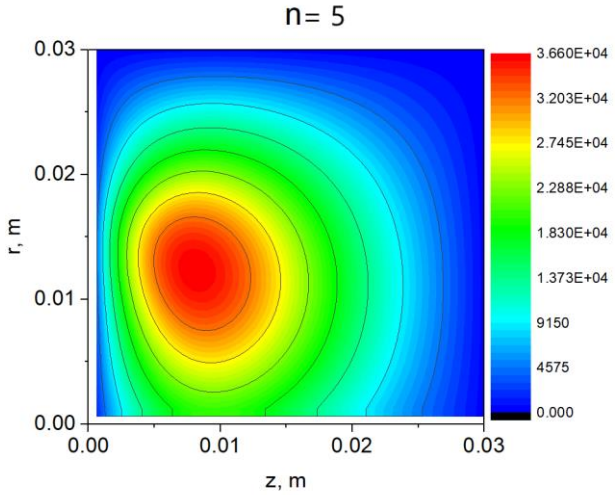

Fig.1. Spatial distribution of clusters (n=5) at $p = 0.5 Torr$.

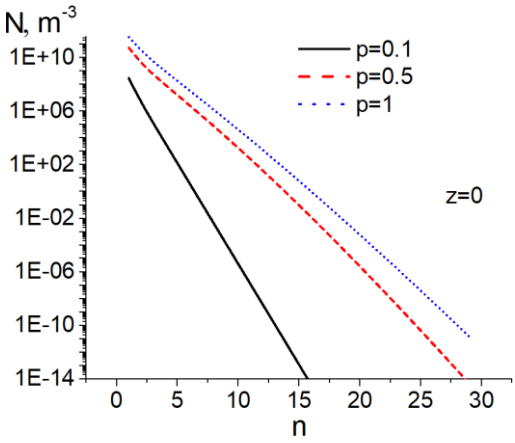

Fig.2. Distribution of clusters by size near the cathode erosion zone at different gas pressure.

It can be seen that the maximum concentration of clusters is formed at some distance from the erosion zone on the cathode, which in our model corresponded to $0.01 m \le r \le 0.02 m$.

Fig. 2 shows that as the gas pressure in the chamber increases, the number of large clusters increases.

References

1. H. Xu and K. S. Suslick. Water-soluble fluorescent silvernanoclusters // Advanced Materials,. -2010. V. 22, N. 10.- P. 1078–1082.
2. M. Guzman, J. Dille, and S. Godet. Synthesis and antibacterial activity of silver nanoparticles against gram-positive and gram-negative bacteria //Nanomedicine,. -2012, V. 8. -P. 37–45.
3. C.-H. Liu, B.-H. Mao, J. Gao et al. Size-controllable selfassembly of metal nanoparticles on carbon nanostructures in room-temperature ionic liquids by simple sputtering deposition // Carbon. -2012, V. 50. -P. 3008–3014.
4. B.M.Smirnov. Clusters and Small Particles in Gases and Plasmas. Springer Science & Business Media. -2000.- 279 p.

FORMATION OF THE CHANNEL IN A DENSE PLASMA BARRIER VIA THE BEAM OF STRONG ELECTROMAGNETIC WAVES

B.R. Mykhailenko, I.O. Anisimov
Taras Shevchenko National University of Kyiv, Faculty of Radio Physics, Electronics and Computer Systems
E-mail: mihaylenko.bogdan12@gmail.com

A supercritical plasma layer transillumination by a strong electromagnetic wave simulation results is presented. Temporal changes in the profile of the standing electromagnetic wave formed by the incident beam has been studied. Was shown that the channel formation occurs in next stages: the formation of a spherical mirror, a conical pit, and then a narrow cylindrical channel. We can observe the flow of electrons leaving the barrier before the channel formation finishes, which requires further study regarding the existence of the informational transparency phenomenon.

Transport of the various types of waves through plasma regions, which are opaque to them in the linear hydrodynamics model, have attracted interest for several decades [1]. In addition to the purely scientific aspects, such problems are also interesting for a number of applications: space communications development, radio physical plasma diagnostics methods, and others. These tasks are also relevant to the laser thermonuclear fusion problem. In our previous works [2-3] we performed plasma barrier transillumination simulation during interaction with a strong electromagnetic beam, accompanied by the channel formation with a reduced plasma density. This paper presents preliminary results concerning the change in the plasma electrons impulse during such transillumination.

The simulation was performed by the particles in cells method using the PIConGPU software package [4]. In our previous study, we showed that transition from 2.5D to 3D simulation leads to a decrease in the scattering of the plasma barrier. And that plasma channel formation is possible even at 10 times lower amplitude of the incident electromagnetic wave in comparison with moderate wave in [2-3]. Here we are investigating new measures that can characterize the behavior of plasma, such as momentum projection. It will allow us to better investigate plasma motion, especially electrons'. Or creating a profile of the standing wave formed by the incident beam and its reflection off the barrier enables a better visualization of the beam-plasma interaction.

The following simulation parameters were used: hydrogen fully ionized plasma was treated, density – $9 \cdot 10^{12} cm^{-3}$ (electron plasma frequency – 18 GHz); plasma temperature – 0.5 eV (isothermal plasma); the plasma layer thickness – 12.5 cm, radius – 21.5 cm; incident wave length – 3.33 cm (frequency – 9 GHz, i.e. plasma is opaque for this wave); pulse duration – 101 ns; pulse radius (at half maximum) – 5 cm; the maximum electric field amplitude is 0.964·MV/cm (4 times smaller than moderate wave in [2-3]).

The simulation results are shown in figs. 1-2, differing in time points. Figures show the particle's impulse horizontal projection, density and electric field spatial distributions averaged in time over a 2 ns period. Time averaging allows us to observe standing electromagnetic waves and remove flickering for impulse visualization.

Thanks to time averaging, studying the concentration distribution, we now eliminate Langmuir oscillations, considering only slow concentration changes induced by the pressure of the high-frequency field (Fig. 1). Furthermore, a minimum of concentration can be observed behind the concave edge of the plasma, which is not accompanied by either a local maximum in intensity or a constant field of a similar configuration. For ions, the momentum distribution is intuitive, but a more complex picture is observed for electrons. We see that despite the unfinished process of channel formation, an electrons flow is formed (Fig. 2).

Simulation results analysis leads to the following conclusion.

1. The transition to using time averaging allowed us to investigate the profile of a standing electromagnetic wave, as well as the behavior of electrons due to their high mobility.

2. After the initial focusing of the electromagnetic wave, we observe how it forms a conical channel. At the apex of this cone, the amplitude significantly increases, after which the wave forms a cavity, which further develops into a narrow cylindrical channel.

3. The presence of electrons moving from the barrier to the left before the channel formation suggests the possibility of informational transparency if there is some correlation between the characteristics of the incident wave and the electrons.

[1] I.O.Anisimov, L.I.Romaniuk. // Ukr. Phys. Journ. Reviews. **6**, 101 (2010). In Ukrainian.
[2] B.R. Mykhailenko, I.O. Anisimov. // Probl. of Atomic Sci. and Techn. №**6 (130),** 64 (2020).
[3] B.R. Mykhailenko, I.O. Anisimov. // Probl. of Atomic Sci. and Techn. **4 (134)**, 3 (2021).
[4] M Bussmann et al. // SC'13 Proc. Int. Conf. High Perform. Comp. Networking, Storage Anal. **60,** 1 (2013).
[5] G.M. Batanov, V.A. Silin. // Proc. Lebedev Phys. Inst. 73, 87 (1974). In Russian.

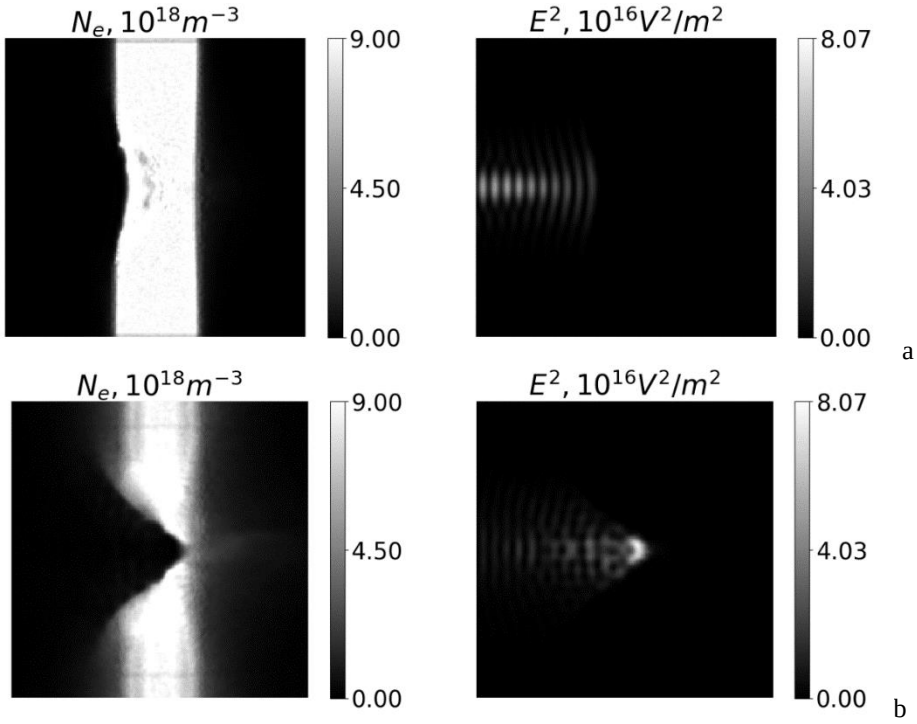

Fig.1. Electrons' density and electric field time averaged distributions, when an electromagnetic beam is falling on plasma, at the time points 23.3 ns (a) 63.8 ns (b)

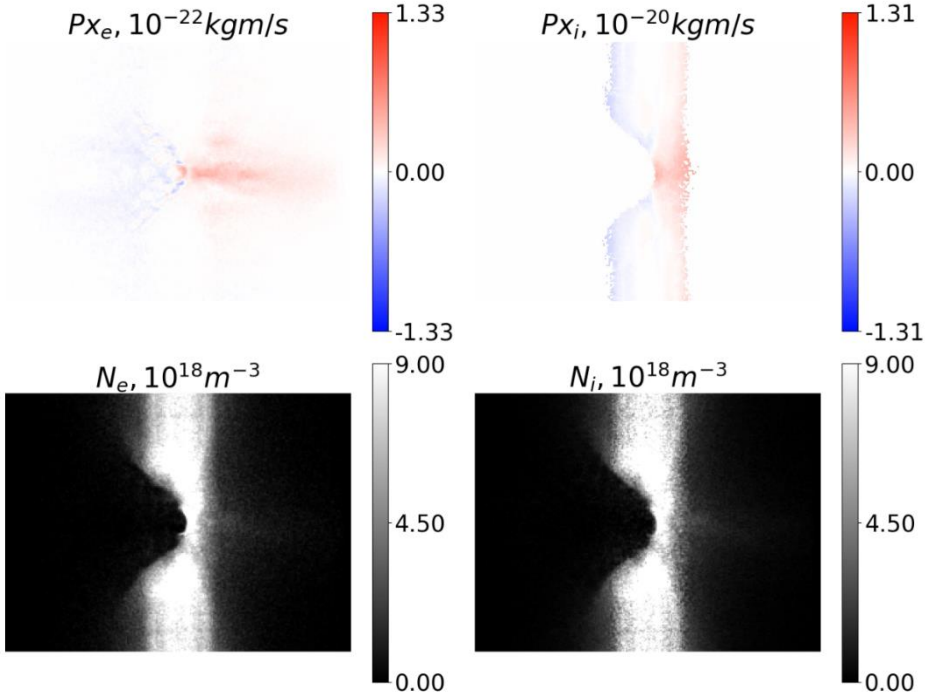

Fig.2. Electrons' and ions' impulse horizontal projection and density time averaged distributions, when an electromagnetic beam is falling on plasma, at the time point 63.8 ns

INVESTIGATION OF PLASMA GENERATION UNIFORMITY IN A DISCHARGE WITH A HOLLOW CATHODE

A.V. Ryabtsev*, V.O. Khomych**

** Institute of Physics of NAS of Ukraine, Kyiv, Ukraine, e-mail: ryabtsev@iop.kiev.ua*

*** Institute of Physics of NAS of Ukraine, Kyiv, Ukraine, e-mail: khomich@iop.kiev.ua*

A new method was proposed for determining the region of plasma generation, based on the processing of experimental data on the plasma concentration in the volume of the discharge chamber. This method was applied to low pressure arc discharge. It was shown that the introduction of an additional electrode leads to a displacement of the plasma generation region towards the walls of the chamber, which helps to increase the uniformity of plasma concentration in the working volume.

Experemental setup

The most advanced methods of plasma modification of the surface of structural materials (for example, nitriding, oxidation) are based on the use of autonomous plasma arc sources [1]. Devices based on such discharges, in contrast to glow discharges, provide more flexible management of the technological parameters of the nitriding (oxidation) process, as well as significantly less ion sputtering of the processed materials, and allow the processing of products of complex shape with holes of different diameters. Also, an important feature of devices based on these discharges is energy efficiency, they allow the generation of bulk plasma with parameters (electron concentration in the plasma $10^{10} \div 5 \times 10^{11}$ cm^{-3}) that ensure acceptable rates of heating and surface cleaning in the process of ion-plasma processing of materials and products.

A plasma generator based on an arc discharge consists of a vacuum chamber with a volume of up to 0.1 m^3, in the upper part of which a thermal emission hollow cathode is installed, the anode is located on the opposite side of the vacuum chamber. The plasma-forming gas argon is supplied through the hollow cathode, while providing its protection from the reactive gas entering directly into the working chamber. Gas supply of the installation and smooth adjustment of ballast and reactive gas pressure was carried out by needle injectors in the range of $10 \div 10^{-1}$ Pa. The discharge is powered by a low-voltage power supply unit (U = 35 ÷ 80 B, I = 5 ÷ 30 A). By changing the discharge current, its power can be adjusted, reaching an electron concentration $n_e \approx 10^9 \div 10^{11}$ cm^{-3} at an electron temperature of 1.4 ÷ 3 eV. The plasma parameters are controlled by a probe that crosses the vacuum chamber between the anode and the cathode in the middle.

But one of the significant disadvantage of plasma devices based on low-pressure arc discharge is the significant nonuniformity of the generated plasma. This leads to uneven surface treatment and/or reduction of the area that can be processed. To solve this problem, we placed an additional electrode between the cadode and the anode, which was under a cathod potential. In more detail the installation is described in [2].

Data processing and discussion

In the stationary case, the distribution of plasma concentration n in the volume of the discharge chamber is described by the ambipolar diffusion equation $D_A \Delta n = -\gamma$, where D_A is coefficent of ambpolar diffusion and γ is source term due to ionization. Considering the plasma concentration at a specific distance *z* from the cathode only as a function of the radius, we obtain the following equation

$$\frac{d^2 n(r)}{dr^2} + \frac{1}{r}\frac{dn(r)}{dr} = -b(r), \qquad (1)$$

where term $b(r)$ include both ionization source and plasama flow along the axis. It has a positive sign if the ionization rate exceeds the flux along the z-direction.

So the value of plasma concentration should be solutions for some source function $b(r)$. Therefore having experemental data for concentration we can solved reverse problem and find the source function. A set of step functions with three regions were chosen as possible source functions $b(r)$. These functions has constant values b_1, b_2, and b_3 for $r < r_1$, $r_1 < r < r_2$, and $r > r_2$ respectevly. Thus, by changing these five parameters, we can select a function for which the solution of equation (1) corresponds best to the experimental data.

The figure 1 shows the obtained functions, as well as experimental and calculated values of plasma concentration for two cases: in the absence of an additional electrode, and in the presence of a conical additional electrode with an apex angle of 60 degrees.

In the case of the ebcence of electrode, the most suitable source function *b* actually has only two regions. In the first one with a radius of about 2.5 cm, the function has a reletively large positive value, which corresponds to intense plasma generation. In the rest of the volume, the function, while remaining positive, decreases by more than two orders of magnitude. This means that in this region, ionization is only slightly superior to transport processes in the axial direction. And indeed, in the absence of an additional electrode in the discharge, a thin luminous area is observed in the center of the chamber.

With the introduction of an additional electrode with an angle of 60º, the picture changes dramatically. In this case, function *b* has a negative value at the center. This corresponds to a region in which there is a large movement of plasma in the axial direction to the anode. In the rest of the volume, function b becomes positive, and its value in the region closer to the center exceeds the value on the periphery by more than five times. This suggests that the main generation of plasma occurs in a wide ring around the center of the discharge chamber. This is visually confirmed by a wide luminous column (up to one third the radius of the chamber) in the presence of an additional electrode. Similar results are obtained for an electrode with an angle of 45º and for a flat electrode.

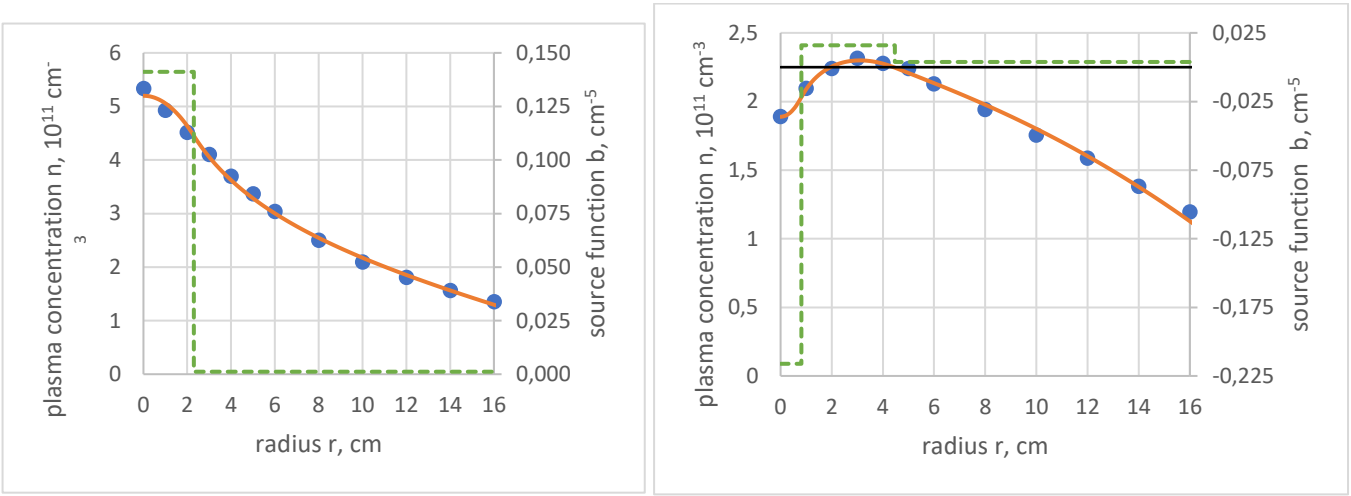

Fig. 1. Dependence of plasma concentration and the resulting source function as a function of radius. a) without additional electrod, b) with addidonal electrod with angle 60º. Circlys – experemental data for concentration; solid line – calculated value of concentration; dashed line – obtained source finction b(r).

Conclusions

The proposed method for processing the results of plasma density measurements in the working volume of the discharge makes it possible to significantly presisly determine the region in which plasma generation occurs. The data obtained in this way are in good agreement with the observational results.

The introduction of an additional electrode into the discharge chamber allows the plasma generation region to be shifted towards the chamber wall, which leads to the formation of a more uniform distribution of plasma concentration throughout the working volume.

References

[1] 1. A.A.Andreev, V.M.Shuvalov, L.P.Sablev. “Steel nitriding in a low-pressure gas arc discharge”, *PSE*, v. 4, N. 3-4, pp. 191-197, 2006.

[2] A.V.Khomich, A.V,Ryabtsev, V.G.Nazarenko “Low-Pressure Uniform Plasma Generator Based on Hollow Cathode for Ion Plasma Technologies” VANT, N 6, pp.89-94, 2022.

ORGANOMETALLIC COMPOUNDS DISPROPORTIONATION REACTIONS IN A PLASMA-LIQUID SYSTEM WITH A ROTATING GLIDING AND SECONDARY DISCHARGE

V.Ya. Chernyak[1], V.V. Iukhymenko[1], K.V. Iukhymenko[1], S.V. Shulga[2], D.D. Tretiakov[1], O.M. Tsymbaliuk[1], S.S. Nedovesov[1], N.V. Matlakh[1]
[1]Taras Shevchenko National University of Kyiv, Faculty of RECS
[2]Institute of Hydromechanics NAS of Ukraine
E-mail: *chernyak_v@ukr.net, yvitaliy@ukr.net, sergey.v.shulga@gmail.com*

A plasma-liquid system with the activation of H_2O distillate and 0.1 M ferrocene solution in organic solvents (ethanol, acetonitrile) with a rotating gliding discharge plasma was studied. The research was conducted using various plasma-forming gases (air, Ar, N_2, CO_2). It was shown that the plasma of both the rotating gliding discharge and the plasma of the secondary discharge supported by the gliding discharge is non-isothermal. It was found that cyclopentadiene ligands of ferrocene disproportionate into saturated cyclic hydrocarbons (cyclopentane and pentane). Also, as a result of plasma chemical synthesis, aromatic compounds (benzene and its derivatives) are formed

Experimental setup and tested substances

An experimental setup with a rotating gliding discharge immersed in a liquid [1] is presented in Fig. 1. The plasma generator consists of a central electrode (cathode), an upper flange (anode) and a dielectric chamber with holes for tangential supply of the working gas. The central part of the anode has a conical shape with a hole in the center. The diameter of the hole is 3 mm. A rotating gliding discharge is ignited between the cathode and the anode. The distance between the cathode and the anode is 1 mm. A quartz tube is placed on the anode, into which the test liquid is poured. A flange is placed on top of the quartz tube, into which an annular secondary discharge electrode is mounted, which was immersed in liquid. As the working gas were used air, Ar, N_2 or CO_2, the flow amounted to 10 and 15 l/min. The gas was fed tangentially to the system axis. The system outlet was connected to the ventilation system.

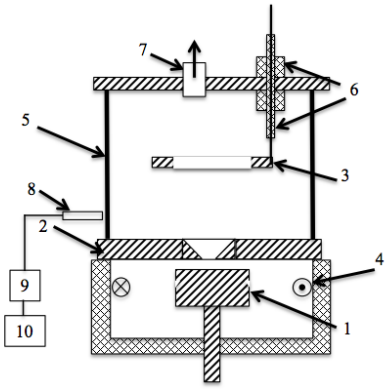

Fig. 1. Scheme of a setup with a rotating gliding discharge immersed in a liquid: 1 – high-voltage primary discharge electrode; 2 – grounding electrode; 3 – high-voltage secondary discharge electrode; 4 – gas inlet; 5 – quartz cylinder; 6 – dielectric; 7 – gas outlet; 8 – optical fiber; 9 – spectrometer; 10 – PC

Electrophysical parameters of discharges

Volt-ampere characteristics of discharges measured are presented for the primary and secondary discharges when the system is filled with distilled water, the volume of which was equal to 100 ml.

The VAC of the primary discharge has a decreasing nature and, within the measurement error, does not depend on the gas flow rate. The VAC of the secondary discharge has a linear nature within the studied current range.

In turn, the variable component of the current is a superposition of a sinusoidal component with a frequency of pulsations of the power source (100 Hz) and a sawtooth component with a frequency (3 kHz at G = 10

l/min) depending on the gas flow rate, which is characteristic of discharges with transverse blowing. Also, the shape of the sawtooth component is affected by the gas flow rate.

Results of optical diagnostics

The temperature of electron levels population (T*e) is greater than the temperature of vibrational and rotational levels population (Tv, Tr). This indicates that the plasma of the rotating gliding discharge is non-isothermal.

In the mode of operation with a secondary discharge, The temperature of O I electron levels population $T^*_e \approx 8000$ K of the secondary discharge plasma at the primary discharge current Ip = 160 mA and air flow 10 l/min. The vibrational levels population temperature is higher than the N_2 rotational levels population temperature. The OH rotational levels population temperature is equal to ≈ 3000 K and is close to $T_r(N_2)$. That is, the secondary discharge plasma is also non-isothermal.

Solutions treatment results

As a result of the treatment of the obtained solutions with the immersed discharge system, the following conclusions can be drawn based on visual observations:

1. The ammonium molybdate solution changed its color from transparent to blue with the formation of a blue precipitate, which indicates the recovery of molybdenum ions (Mo).
2. The nickel chloride solution changed its color from light green to brown with the formation of a precipitate.
3. The cobalt chloride solution color remained original without the formation of a precipitate, that is, no recovery or hydrolysis reactions were recorded.
4. Alcoholic solutions of organic compounds did not change their color as a result of plasma chemical synthesis, their composition was studied using nuclear magnetic resonance (NMR).

As a result of plasma chemical synthesis in the nitrogen, water and ammonium molybdate system, the formation of molybdenum blue was recorded. This indicates the formation of a recovering agent in the reaction mixture (atomic hydrogen) and the recovery of Molybdenum (VI) ions to oxidation states (IV-V).

Conclusions

1. The plasma of a rotating gliding discharge immersed in a liquid and a secondary discharge supported by a rotating gliding discharge is non-isothermal.
2. Population temperatures of vibrational and rotational levels for a nitrogen molecule N_2 are the same within the margin of error ≈ 4,500 K.
3. The electron levels population temperature amount to ≈ 8,000 K.
4. The population temperature of the OH rotational levels and N_2 rotational levels are the same within the measurement error.
5. The ability to perform the redox of inorganic substances with a change in the metal's valency has been demonstrated.
6. One-stage conversion of cyclopentadienyl ligands into aromatic hydrocarbons is performed, which is only possible in chemistry through a multi-step process.

References

[1] V.V. Iukhymenko, V.Ya. Chernyak, D.K. Hamazin, D.S. Levko, V.A. Bortyshevsky, R.V. Korzh, Rotating gliding discharge submerged in liquid //Problems of Atomic Science and Technology. Series “Plasma Physics” (23). 2017, №1, p. 136-139.

PLASMA STREAMS GENERATED BY MAGNETOPLASMA COMPRESSOR WITH AXIAL MAGNETIC FIELD

Y.E. Volkova[1,2], D.G. Solyakov[1], I.E. Garkusha[1,2], A.K. Marchenko[1], M.S. Ladygina[1], V.V. Staltsov[1], Yu.V. Petrov[1], V.V. Chebotarev[1], T.M. Merenkova[1], V.A. Makhlai[1,2], D.V. Yeliseyev[1]

[1]Institute of Plasma Physics NSC "Kharkiv Institute of Physics and Technology", Akademichna St., 1, Kharkiv, Ukraine, e-mail: solyakov@ipp.kharkov.ua

[2]V.N. Karazin Kharkiv National University, Svobody Square, 4, Kharkiv, Ukraine, e-mail: y.e.volkova.kh@gmail.com

The effect of the external magnetic field on the dynamics, structure, and parameters of pinching plasma flows generated by a magnetoplasma compressor was studied. The plasma stream has a complex structure, including clusters of concentric vortices and closed toroidal current structures observed throughout its lifetime. The presence of the external magnetic field in the MPC discharge channel improves compressive characteristics of the plasma flow. The formation of a current-sheet-like structure in the plasma stream has been detected.

Introduction

The generation of high-energy dense plasma streams is one of the critical issues in modern plasma physics. Such streams are vital for materials modification technologies, fusion research, spacecraft propulsion, etc. A magnetoplasma compressor (MPC) used in the present research is a quasistationary plasma device that generates powerful plasma streams with a pronounced pinching effect. The additional magnetic field in such plasmadynamic devices opens an opportunity to improve discharge characteristics and increase plasma parameters [1]. Quasistationary plasma devices with different external magnetic systems are widely used for testing of the materials performance and simulations of conditions at the divertor plates of fusion reactor ITER under transient events [2].

We conduct experimental studies of the influence of an external longitudinal magnetic field in the discharge channel of the MPC on fundamental processes in compressive plasma flows.

Experimental results

The MPC described elsewhere [3-4] is installed inside a solenoid that produces an axial magnetic field of up to 0.4 T inside the accelerating channel. The inner diameter and the total length of the solenoid are 15 and 17 cm, respectively. The MPC device operates in a regime with residual gas at different pressures. The complete system of the MPC with the solenoid is installed inside the vacuum vessel of 2 m in length and 40 cm in diameter. The diagnostic system includes a Rogowski coil for discharge current measurements, voltage dividers, and a set of local magnetic and electric probes. Experiments have been carried out under the following experimental conditions: the residual working gas – Helium, at a pressure of 2 Torr; the discharge current of 400 kA; the magnitude of the external longitudinal magnetic field inside the MPC channel of 0 and 0.24 T.

The plasma stream has a complex structure, including clusters of concentric current vortices, closed toroidal currents, and the formation of enclosed equipotentials. During the application of an external magnetic field, the configuration of the enclosed equipotentials is shifted to a greater distance from the MPC output. The external magnetic field leads to an increase in the magnitude of the electric current in the plasma stream, changes its spatial distribution, and reduces the number of current vortices. The findings demonstrate that in the presence of an external magnetic field (0.24 T), the compression zone grows, its temperature increases sixfold, and the radial component of Ampere's force goes up at least threefold. These results make it possible to apply an external magnetic field in magnetoplasma compressors to improve the compressive properties of the flow, which is crucial for further development of plasma sources of extreme ultraviolet radiation for new-generation lithography.

A structure similar to a current sheet has been observed in the compressive plasma stream of the MPC for the first time. Two-dimensional distributions of the electric current isolines in the plasma stream show the sheet formation during the second halfperiod of the discharge current. Two groups of electrons with different

temperatures appear near the layer. Also, the current density, the temperature of the second group of electrons, and the ion saturation current reach a peak in close proximity to the sheet. The reversed direction of the drift velocity near the center of the plasma stream might be explained by the outflow of an electron beam from the layer. The formation of a current-sheet-like structure without an external magnetic field occurs later than with its application. This finding opens an opportunity for laboratory modeling of various processes, including astrophysical phenomena.

References

[1] A.Z. Giovannini, I. Barendregt, T. Haslinde, et al., "Self-confined plasma in a magneto-plasma compressor and the influence of an externally imposed magnetic field", Plasma Sources Sci. Technol., vol. 24, pp. 025007, 2015.

[2] I.E. Garkusha, V.A. Makhlai, Yu.V. Petrov et al., "Vapour shielding of liquid-metal CPS-based targets under ELM-like and disruption transient loading", Nucl. Fusion, vol. 61, pp. 116040, 2021.

[3] D.G. Solyakov, Yu.Ye. Volkova, et al., "Distributions of magnetic field and current in pinching plasma flows: axial magnetic field effect", Eur. Phys. J. Plus., vol. 136, pp. 566, 2021.

[4] D.G. Solyakov, Yu.Ye. Volkova, et al., "Measurement of the local electron temperature in self-compressed plasma stream", Probl. Atom. Sci. Techn., vol. 4(134), pp. 149-153, 2021.

CHARACTERISTICS OF PLASMA SYSTEMS WITH ROTARY GLIDING DISCHARGE

V.Ya. Chernyak*, S.S. Nedovesov*, V.V. Iukhymenko*, O.M. Tsymbaliuk*, S.V. Shulga, K.V. Iukhymenko*, D.D. Tretiakov***

** Faculty of RadioPhysics, Electronics and Computer Systems Taras Shevchenko National University of Kyiv, Kyiv 01601, Ukraine, e-mail: chernyak_v@ukr.net*

*** Institute of Hydromechanics NAS of Ukraine, Kyiv, Ukraine, email: sergey.v.shulga@gmail.com*

The paper presents the results of an experimental investigation into the parameters of atmospheric pressure secondary discharge plasma sustained by a low-power (~100 W) rotating gliding discharge in an air flow, under conditions where the volume of the current channel of the secondary discharge significantly exceeds that of the standalone discharge channel. Plasma parameters were determined using emission spectroscopy methods with the SpecAir program. The assessment of the electric field intensity in the secondary discharge plasma was based on variations in voltage drop across the secondary discharge as a function of changes in the discharge channel length through adjustments in the interelectrode distance.

Installation scheme

The installation scheme and description are presented in Figure.1. The current was measured through the voltage drop across the 50 Ohm resistors. The voltage was measured by a resistive divider (D) with a ratio of 1:10000. Current setting resistor (ballast) 21.5 kΩ.

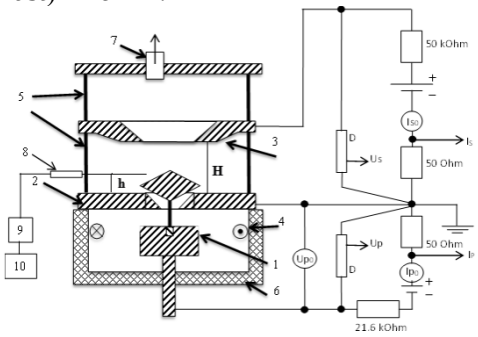

Figure 1. Scheme of a setup with a rotating gliding discharge: 1 – high-voltage primary discharge electrode; 2 – grounding electrode; 3 – high-voltage secondary discharge electrode; 4 – gas inlet; 5 – quartz cylinder; 6 – dielectric; 7 – gas outlet; 8 – optical fiber; 9 – spectrometer; 10 – PC [1]

Results and discussion

The voltage-current characteristics of the discharge system, measured using oscilloscope, for both the primary and secondary discharges, are presented in Figure 2.

As evident from the plots, the voltage-current characteristic (V-I curve) of the primary discharge exhibits a decreasing trend and is relatively insensitive to gas flow within the measurement error range. In the investigated current range, the V-I curve of the secondary discharge demonstrates a linear behavior.

(a) *(b)*

Figure 2. Typical oscillograms of current and voltage in the primary (a) and secondary (b) circuit, recorded on the installation at an air flow of 10 l/min, Ipo = 100 mA.

All measured spectra are characterized by the presence of radiation of molecular bands OH (A-X), N_2 (C-B) and atomic lines of both the elemental components of the plasma-forming gas (O) and the components of the electrode material (the main components of stainless steel are Cr, Fe) [2].

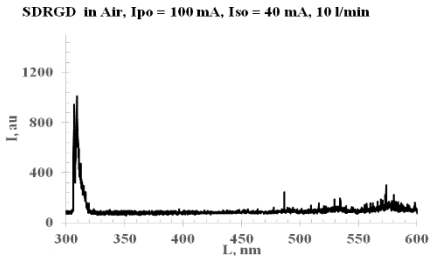

Figure 3. The dependence of plasma emission intensity (I) on wavelength (L) for SDRGD in the plasma system is shown. This was observed at a current of Ipo = 100 mA, Iso = 40 mA, and an air flow rate of 10 L/min. The temperature of Tr(OH) = 2800 K.

Typical oscillograms of currents and voltages in the RGD and SDRGD circuits, recorded on the setup for the activation of chemical transformations of gas-phase substances by secondary discharge plasma sustained by a rotating gliding discharge (Figure 2), respectively.

Table 1

h, mm	RGD	Tr(OH), K	Tv(OH), K	Tr(N_2), K	Tv(N_2), K	T*e(O), K	T*e(Cr), K
5	Air	3800	-	4000	4000	-	5800

The temperatures of population of rotational and vibrational levels of molecules and electronic levels of atoms determined in Table 1. Comparison of the obtained values of population temperatures of different excited levels indicates the non-equilibrium nature of the plasma of the rotating gliding discharge in the air flow, both submerged and not submerged in water (Tr < Tv < Te). It is also noticeable that submerging RGD in water leads to an increase in plasma non-equilibrium due to a decrease in Tr and an increase in T*e without a significant effect on Tv.

Figure 4. Electron energy distribution function (EEDF).

Conclusion

It has been demonstrated that high-pressure plasma systems with a secondary discharge, sustained by a rotating gliding discharge, are capable of generating non-equilibrium plasma of significantly larger volume with a broader range of parameter adjustments compared to standalone discharge systems. This holds the potential for scaling up plasma-chemical processes.

At atmospheric pressure, the kinetic temperature of the plasma T=Tr and according to the determined Tr≈T≈ 4000 K. Taking into account that at a higher gas flow rate in RGD than in SDRGD, the static pressure in the RGD flow is lower than in SDRGD and, accordingly, the electric field E/N>50 Td in RGD plasma.

References

[1] V.V. Iukhymenko, V.Ya. Chernyak, D.K. Hamazin, D.S. Levko, V.A. Bortyshevsky, R.V. Korzh, Ro-tating gliding discharge submerged in liquid // Problems of Atomic Science and Technology. Series “Plasma Physics” (23). 2017, №1, p. 136-139.

[2] www.specair-radiation.net

DIFFERENTIAL EQUATION WITH NON-HOMOGENEOUS COEFFICIENTS FOR THE LONG-TERM COMPLEX AMPLITUDE OF THE ELECTRIC FIELD IN A PLASMA

V.M. Lashkin*, N.A.Beloshenko**

**Kyiv Institute for Nuclear Research, Kyiv Nauki avenue 47, Ukraine, e-mail: vlashkin62@gmail.com*

*** Kyiv Institute for Nuclear Research, Kyiv Nauki avenue 47, Ukraine, e-mail: Beloshenko@gmail.com*

The problem with a plasma cylinder and a cylindrical cavity is taken as a basis. The solution of the system of six differential equations is a differential equation with an operator and the square of the operator on the longitudinal complex amplitude of the electric field in the plasma. A differential equation of the fourth order. The coefficients for the operator and for the longitudinal complex amplitude of the electric field include the components of the dielectric permeability tensor. Next, the substitution of the components of the dielectric permittivity tensor , which depend on the radius, is carried out.

Differential equation with non-homogeneous coefficients

The problem with a plasma cylinder and a cylindrical cavity is taken (the system with a plasma cylinder was also considered in [1]) as a basis. The system consists of three parts - the vacuum outside and inside the plasma cylinder and the plasma cylinder itself. The boundary conditions are determined by two transverse conductive walls that limit the sides of the plasma cylinder. The plasma cylinder is excited by a ring antenna. The ring current is taken into account in the crosslinking conditions. Next, we are interested in the plasma part of the system - the plasma cylinder. From Maxwell's equations (the plasma part of the system), after a substitution that satisfies the boundary conditions and gives a transition to complex amplitudes, a system of differential equations for complex amplitudes is obtained. The substitution is made in Maxwell's equation in the cylindrical coordinate system. After the substitution, which gives the transition to the complex amplitudes of the fields, a system of six differential equations for the complex amplitudes of the fields is obtained. The solution of the system of six differential equations is a differential equation with an operator and the square of the operator on the longitudinal complex amplitude of the electric field in the plasma. A differential equation of the fourth order. The coefficients for the operator and for the longitudinal complex amplitude of the electric field include the components of the dielectric permeability tensor. Next, the differential equation with the operator and the square of the operator on the longitudinal complex amplitude of the electric field is isolated. A differential equation of the fourth order. The coefficients of this equation with the operator and the square of the operator include the components of the dielectric permittivity tensor. Next, the substitution of the components of the dielectric permittivity tensor , which depend on the radius, is carried out. In these components of the dielectric permittivity tensor, the plasma frequency depends on the radius. The plasma frequency depends on the radius, because the plasma concentration depends on the radius. This (dependence of the plasma concentration on the radius) is a generalization of the problem with a plasma cylinder with a cylindrical cavity. Substitution of the components of the dielectric permeability tensor for the case of a zero electronic collision coefficient and for the case of a non-zero electronic collision frequency was carried out. In addition to substituting the components of the dielectric permittivity tensor into the equation with the operator and the square of the operator, the operator and the square of the operator were revealed. In this way, a fourth-order differential equation with inhomogeneous coefficients for the longitudinal complex amplitude of the electric field in the plasma was obtained. A differential equation with inhomogeneous coefficients, which is suitable for further application of the finite difference method for its solution. When its solution (a plasma cylinder problem with a cylindrical cavity) was the Bessel functions. The resulting differential equation with inhomogeneous coefficients is given below..

$$\left[((\omega+i\nu_e)^2-\omega_{ce}^2)\omega-\omega_{pe}^2(\omega+i\nu_e)\right]\frac{(\omega+i\nu_e)}{\omega(\omega+i\nu_e)-\omega_{pe}^2}\,d_r^4E_z+$$

$$+\left[((\omega+i\nu_e)^2-\omega_{ce}^2)\omega-\omega_{pe}^2(\omega+i\nu_e)\right]\frac{(\omega+i\nu_e)}{\omega(\omega+i\nu_e)-\omega_{pe}^2}\frac{2}{r}\,d_r^3E_z-$$

$$-\left\{\left[((\omega+i\nu_e)^2-\omega_{ce}^2)\omega-\omega_{pe}^2(\omega+i\nu_e)\right]\frac{(\omega+i\nu_e)}{\omega(\omega+i\nu_e)-\omega_{pe}^2}\frac{2m^2+1}{r^2}\right.$$
$$\left.+\,g(r)\frac{\omega(\omega+i\nu_e)((\omega+i\nu_e)^2-\omega_{ce}^2)}{\omega(\omega+i\nu_e)-\omega_{pe}^2}\right\}d_r^2E_z+$$
$$+\left\{\left[((\omega+i\nu_e)^2-\omega_{ce}^2)\omega-\omega_{pe}^2(\omega+i\nu_e)\right]\frac{(\omega+i\nu_e)}{\omega(\omega+i\nu_e)-\omega_{pe}^2}\frac{2m^2+1}{r^3}\right.$$
$$\left.-\frac{1}{r}g(r)\frac{\omega(\omega+i\nu_e)((\omega+i\nu_e)^2-\omega_{ce}^2)}{\omega(\omega+i\nu_e)-\omega_{pe}^2}\right\}d_rE_z+$$
$$+\left\{\left[((\omega+i\nu_e)^2-\omega_{ce}^2)\omega-\omega_{pe}^2(\omega+i\nu_e)\right]\frac{(\omega+i\nu_e)}{\omega(\omega+i\nu_e)-\omega_{pe}^2}\frac{m^4-4m^2}{r^4}+\frac{m^2}{r^2}g(r)\frac{\omega(\omega+i\nu_e)((\omega+i\nu_e)^2-\omega_{ce}^2)}{\omega(\omega+i\nu_e)-\omega_{pe}^2}\right.$$
$$\left.+\,g_1(r)\right\}E_z=$$
$$=-(1-N_l^2)^2\,((\omega+i\nu_e)^2-\omega_{ce}^2)E_z$$

$$g_1(r)=\frac{\omega_{pe}^4\omega_{ce}^2}{\omega^2}\,\frac{1}{(\omega+i\nu_e)^2-\omega_{ce}^2}-2(1-N_l^2)\frac{\omega_{pe}^2}{\omega}\,(\omega+i\nu_e\,)+\frac{\omega_{pe}^4}{\omega^2}(\omega+i\nu_e)^2\frac{1}{(\omega+i\nu_e)^2-\omega_{ce}^2}$$

$$g(r)=-\left(\frac{4\pi e^2n_0(r)}{m_e}\,\frac{1}{\omega}\,\frac{\omega_{ce}}{(\omega+i\nu_e)^2-\omega_{ce}^2}\right)^2$$
$$+\left(N_l^2-1+\frac{4\pi e^2n_0(r)}{m_e}\,\frac{1}{\omega}\,\frac{\omega+i\nu_e}{(\omega+i\nu_e)^2-\omega_{ce}^2}\right)\left(2\right.$$
$$\left.-\frac{4\pi e^2n_0(r)}{m_e}\,\frac{1}{\omega^2+i\nu_e\,\omega}\,\frac{2(\omega+i\nu_e)^2-\omega_{ce}^2}{(\omega+i\nu_e)^2-\omega_{ce}^2}\right)$$

References

[1] Characterization of an annular helicon plasma source powered by an outer or inner RF antenna. Yunchao Zhang, Christine Charles and Rod Boswell. Plasma Sources Science and Technology Received 24 March 2015, revised 25 August 2015 Accepted for publication 12 November 2015 Published 14 December 2015 .

COMPUTER TECHNOLOGIES

IMPROVING IOT WITH BLOCKCHAIN: CONSENSUS AND ENERGY EFFICIENCY

Leonid Chepel*, Yuriy Boyko**
Faculty of RadioPhysics, Electronics and Computer Systems Taras Shevchenko National University of Kyiv, Kyiv 01601, Ukraine
*email:*leonid.chepel@knu.ua,**yuriyboyko@knu.ua*

Introduction

The Internet of Things (IoT) has revolutionized various industries by enabling the remote monitoring and control of devices. However, it also presents numerous challenges, including issues related to security, coverage, scalability, interoperability, bandwidth, data storage, and remote maintenance. To address these challenges, blockchain technology offers several advantages such as shared ledgers, consensus protocols, cryptography, and smart contracts. Many researchers are studying how blockchain can be combined with IoT, showing a growing interest in this field. This paper offers an overview of the current landscape in optimizing blockchain for IoT solutions, with a specific focus on consensus mechanisms.

The proposed model outlined in this study is based on an analysis of existing research and allows for the implementation of a hybrid model. This approach enhances energy efficiency while upholding high levels of security, reliability, and data integrity in IoT deployments. Importantly, it reduces reliance on centralized cloud providers. By combining Directed Acyclic Graph (DAG) consensus mechanisms at the IoT device level with Proof of Stake (PoS)/Delegated Proof of Stake (DPoS) and Zero-Knowledge (Zk)-Rollups, the system becomes more secure, reliable, and energy-efficient.

Analysis criteria and results

In the analysis, the following criteria were considered:

- The capability to directly integrate blockchain network into IoT devices.
- Designing an efficient IoT device architecture focusing on energy efficiency and security.
- Establishing a genuinely decentralized IoT network.

Table 1 – Compariative analysis of consensus mechanisms

Consensus protocol	**Work principle**	**IoT-friendly**	**Verdict**
Proof-of-Work (PoW)	Miners compete to solve complex mathematical puzzles to add new blocks to the blockchain. The first miner to solve the puzzle is rewarded with tokens.	No	Is not possible to embed into small devices as it has high resource consumption. Some projects like Ethereum agreed to switch to PoS.
Proof-of-Stake (PoS)	Validators are chosen to add new blocks to the blockchain based on the amount of tokens they stake. Validators are rewarded with tokens for verifying new blocks.	Partially	Validators can be implemented as separate compute nodes while other parts may be implemented on IoT device.
Delegated Proof-of-Stake (DPoS)	Participants vote for delegates to validate transactions and add new blocks to the blockchain. Delegates are rewarded with tokens for their work.	Yes	Delegation makes system less resource-hungry but validators still should be implemented as separate compute nodes.

Directed Acyclic Graph (DAG)	DAG-based consensus protocols do not require miners or validators. Instead, transactions are verified and added to the blockchain in a continuous process.	Yes	Perfect mechanism for IoT devices. Drawback is that if 30% of network is vulnerable then it is possible to add new block by attacker and no smart contracts support.
Practical Byzantine Fault Tolerance (PBFT)	PBFT is a consensus algorithm that can tolerate Byzantine failures, where nodes may fail arbitrarily or even behave maliciously. PBFT is used in some blockchain networks, but it is less scalable than other consensus protocols.	No	It is good protocol for enterprise solutions. For IoT it may be used on IoT hubs that receive data from smaller IoT devices.

Another crucial aspect involves a technology known as Zk-Rollups, enabling the construction of a multi-layered blockchain network. In one layer, IoT devices are situated, some of which may have intermittent internet access. These devices form a local blockchain network, consolidating multiple transactions into a single transaction. This transaction is then sent to the main layer either simultaneously or at a later time. This process is feasible on the Ethereum network with the Proof of Stake (PoS) consensus mechanism.

However, for optimal device-to-device communication, the Directed Acyclic Graph (DAG) consensus mechanism proves to be highly effective. It can be combined with Practical Byzantine Fault Tolerance (PBFT) or PoS/Delegated Proof of Stake (DPoS) at a higher level. In this approach, IoT devices ensure high security through encrypted connections and authentication, making them resistant to compromises. Local nodes within Layer2 handle data preprocessing with smart contracts, which is then sent in batches from Layer2 to Layer1 using Zk-Rollups. Cloud-based and local nodes operate independently, ensuring data integrity through consensus protocols.

References

[1] Baig, M.J.A.; Iqbal, M.T.; Jamil, M.; Khan, J. A Low-Cost, Open-Source Peer-to-Peer Energy Trading System for a Remote Community Using the Internet-of-Things, Blockchain, and Hypertext Transfer Protocol. Energies 2022, 15, 4862. URL: https://doi.org/10.3390/en15134862. doi:10.3390/en15134862

[2] Lavaur, T.; Lacan, J.; Chanel, C.P.C. Enabling Blockchain Services for IoE with Zk-Rollups. Sensors 2022, 22, 6493. URL: https://doi.org/10.3390/s22176493. doi:10.3390/s22176493

[3] Namane, S.; Ben Dhaou, I. Blockchain-Based Access Control Techniques for IoT Applications. Electronics 2022, 11, 2225.URL: https://doi.org/10.3390/electronics11142225. doi:10.3390/electronics11142225

[4] Wadhwa, S.; Rani, S.; Kavita; Verma, S.; Shafi, J.; Wozniak, M. Energy Efficient Consensus Approach of Blockchain for IoT Networks with Edge Computing. Sensors 2022, 22, 3733. URL: https://doi.org/10.3390/s22103733. doi:10.3390/s22103733

[5] Ibrahim, R.F.; Abu Al-Haija, Q.; Ahmad, A. DDoS Attack Prevention for Internet of Thing Devices Using Ethereum Blockchain Technology. Sensors 2022, 22, 6806. URL: https://doi.org/10.3390/s22186806. doi:10.3390/s22186806

[6] Kushwaha, R., Singh, D. (2021). Hyperledger Architecture for Internet of Things and Supply Chain Management Services. In: Lee, SW., Singh, I., Mohammadian, M. (eds) Blockchain Technology for IoT Applications. Blockchain Technologies. Springer, Singapore. URL: https://doi.org/10.1007/978-981-33-4122-7_3. doi:10.1007/978-981-33-4122-7_3

[7] Popov, S. The Tangle. White Paper. 2018. Available online: http://www.descryptions.com/Iota.pdf

RADIO ENGINEERING AND COMMUNICATIONS

CLASIFICATION OF COMBUSTION PRODUCTS FROM TREE LEAVES ELECTRONIC CIGARETTES IN OUTDOOR CONDITIONS

A. Antonenko, V. Boretskij, O. Zagaria
Taras Shevchenko National University of Kyiv, 64/13, Volodymyrska Street, Kyiv, Ukraine
e-mail: andreww131998@gmail.com

The paper presents data from air quality monitoring networks for the recognition of pollution types. Sensor modules ZPHS01B, PMS 7003, and BME 280 operating in outdoor conditions were used to monitor the impact of pollutants. A neural network was trained to classify two types of pollutants: combustion of tree leaves and electronic cigarette products.

Introduction

With the constant growth of urban population and industrialization, the issue of air quality has become increasingly relevant and critical for ensuring the health of city dwellers. Air pollution affects not only physical health but also the state of the surrounding environment. Both state and public networks are established to monitor air quality [1].

State monitoring uses high-precision and expensive equipment measuring many parameters such as SO_2, CO, O_3, NO_2, H_2S, PM, radiation, and others. However, expanding such a network with good coverage is often costly, making it challenging for state authorities to scale such a network. Public networks address this problem, but they use less accurate equipment, often measuring a specific set of parameters such as PM2.5, PM10, humidity, and pressure. Gas concentrations such as CO_2, VOC, and NO_2 are less frequently measured. Combining state and public networks can enhance air quality monitoring. State monitoring data can be used to calibrate sensors in public networks, increasing the reliability of public network data and providing broader overall monitoring coverage.

Pollution data is presented in values that may not always be understandable for the average user. By themselves, the values of the level of pollution do not provide an answer to the question of the source of pollution. People are usually interested in identifying the possible sources of pollution. In this context, there is a need for new approaches to monitoring, specifically the classification of types of air pollutants. Previous work [2] successfully used a neural network to recognize two pollutants in binary formats, such as flux pairs and alcohol combustion products. The method showed prospects for using a neural network for pollutant recognition (classification) using low-cost sensors, although these studies were conducted in laboratory conditions.

This work explores the possibilities of applying low-cost sensors and artificial neural networks to create a classification of anthropogenic outdoor pollution. For this, a 22-liter box with two holes and built-in fans was used, in which the sensors are placed, as shown in Fig. 1. Pollutants were introduced into the setup, which was located in the inner courtyard of the Faculty of Radio Physics, Electronics, and Computer Systems. Sensor modules, such as ZPHS01B, were used for monitoring the impact of pollutants, measuring concentrations of various air components, including PM2.5, CO_2, CH_2O, TVOC, O_3, CO, NO_2, as well as temperature and relative air humidity [4]. Calibrated sensors PMS 7003 [5] and BME280 [6] were also used to measure PM1, PM2.5, PM10, and temperature with relative humidity, respectively. The HiLink 7688-based platform was used for data collection, processing, and transmission.

Sensor data were recorded every two seconds, independently for each sensor. For further data consolidation into a single array, time averaging over a 5-second interval was applied. A pause was made before each experiment, waiting for the readings to return to a steady state to avoid influencing the next series of experiments. There were two pollutants in total, namely combustion products from tree leaves and electronic cigarette products. Five measurements were made for each pollutant, with a combustion time of approximately 15 seconds for each.

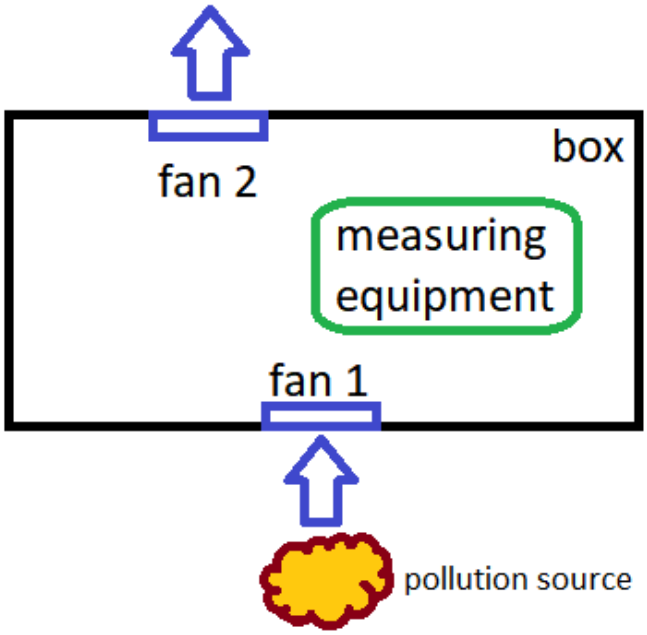

Fig. 1 Block scheme of experimental setup

References

[1] Борисенко А.В. Стан атмосферного повітря і неінфекційна захворюваність [Електронний ресурс] Лариса Василівна Кабан // Проблематика громадського здоров'я. –- 2020.. – Режим доступу: http://cgz.vn.ua/problematika-gromadskogo-zdorovya/problematika-gromadskogo-zdorovya_455.html

[2] Antonenko, A., Boretskij, V., and Zagaria, O.: Classification of Indoor Air Pollution Using Low-cost Sensors by Machine Learning, EGU General Assembly 2023, Vienna, Austria, 24–28 Apr 2023, EGU23-14856, https://doi.org/10.5194/egusphere-egu23-14856, 2023.

[3] ZPHS01B Datasheet URL: https://pdf1.alldatasheet.com/datasheet-pdf/view/1303697/WINSEN/ZPHS01B.html

[4] Plantower PMS7003 Datasheet URL: https://www.espruino.com/datasheets/PMS7003.pdf

[5] Bosch 280 Datasheet URL: https://www.mouser.com/datasheet/2/783/BST-BME280-DS002-1509607.pdf

USING OF VARIOUS FREQUENCY BANDS OF EARTH SATELLITES RADIO EMISSION FOR DIAGNOSE THE DEGREE OF SEA WAVES

Yu. A. Pedenko*, V. B. Synytsky, V. B. Zamarajev*****

**O. Ya. Usikov Institute for Radiophysics and Electronics of the National Academy of Sciences of Ukraine, Kharkiv 61085, Ukraine, e-mail: yuriy.pedenko@gmail.com*

*** O. Ya. Usikov Institute for Radiophysics and Electronics of the National Academy of Sciences of Ukraine, Kharkiv 61085, Ukraine, e-mail: vladimir.b.sinitskiy@gmail.com*

****O. Ya. Usikov Institute for Radiophysics and Electronics of the National Academy of Sciences of Ukraine,Kharkiv 61085, Ukraine, e-mail: zvb73zvb73@gmail.com*

The results of experimental studies of diffuse components of sea waves obtained during GPS and «Transit» satellite setting over the sea surface are presented. The experiments and model calculations carried out confirm the conclusion about the need to use satellite radiation in different frequency bands to expand the scale of the disturbances under study.

The study of the extent of sea waves is important both for practical needs (e.g. flight safety over the sea) and for the development of physical theory of processes occurring over the sea surface.In addition to local measurements of wave strength, radiation from satellites has recently been used for this purpose. In this case, the dominant method is radar one, which uses sea reflections in nadir surface sounding. Alternatively, a different approach can also be applied, where the diffuse component of the signal reflected from the surface when propagating at grazing angles is the main physical characteristic for the measurements.

Model

The characteristics of the diffuse component are described by a statistical model [1,2], corresponding to the Rayleigh concept for rough surfaces. In this model, the type of characteristics depends on the roughness parameter $q = \sigma_h \sin\alpha/\lambda$, where σ_h is the standard deviation of sea wave heights from the average level, λ is the radio wavelength, and α is the grazing angle. The diffuse component graph based on this model [2] can be represented as a polynomial that relates the relative intensity of the diffuse component ξ to the roughness parameter $q = \sigma_h \sin\alpha/\lambda$ [3]:

$$\begin{aligned} &\xi(q) = \frac{\rho_d}{\rho_0} = 0.794q + 108.3q^2 - 1094q^3 + 3042q^4, \quad \text{if } q \le 0.137 \\ &\xi(q) = 0.4, \qquad\qquad\qquad\qquad\qquad\qquad\quad \text{if } q > 0.137 \end{aligned} \tag{1}$$

where $\rho_d(\alpha) = \sigma_{rs}(\alpha)/D(\alpha)$ is the diffuse scattering coefficient; $\sigma_{rs}(\alpha)$ – the standard deviation of received signal; $D(\alpha)$ – current average signal value; $\rho_0(\alpha)$ – reflection coefficient of a smooth surface.

Using formulas (1), the function $\xi(q)$ was calculated depending on the variables included in the parameter q, i.e. from σ_h, α and λ. For the calculation, wavelengths were selected corresponding to the radio bands of navigation satellites of the 1- st and 2- nd generations - «Transit» (λ = 0.75 m) and GPS (λ = 0.19 m), in which the experiments were carried out. It follows from the calculations that there is a specific “saturation” of the diffuse component characteristics with increasing waves, and it is more peculiar of the shorter wavelength range. Therefore, the short wavelength of the source is a limiting factor for diagnosing strong wave values. To expand the range of measured values, it is necessary, in accordance with the Rayleigh criterion, to supplement the HF radiation with lower frequency radiation. This is confirmed by the results of experiments with satellites emitting in different frequency bands.

Experiment

Experiments on «Transit» and GPS satellite setting over the sea were carried out in the eastern part of Crimea at different periods. The main focus of the experiments in all series was the joint study of satellite signals and signals on stationary over-the-horizon near-water paths under conditions of different tropospheric

refraction [4]. Additional processing of experimental material is aimed at determining the characteristics of satellite signals associated with sea waves. This paper compares the characteristics of signals from the GPS and «Transit» systems obtained under approximately similar conditions (from calm to moderate waves).

The fluctuation component was isolated from the complete signal and its further processing was carried out using the moving average and moving standard deviation methods. As a result, the relative intensity of the diffuse component for GPS and «Transit» is determined. Additional computer modeling was carried out, assuming a Rayleigh distribution of the diffuse component, confirming the conclusions of the full-scale experiment.

Comparison of experimental characteristics with calculated ones makes it possible to determine the degree of sea waves in a particular experiment. Thus, from Figure 1a it follows that in the GPS experiment corresponding to dashed lines (calm), the waves were about $\sigma_h \sim 0.02$ m, and in the experiment corresponding to solid curve (rough) $\sigma_h \sim 0.18$ m, i.e., there is a sufficient contrast between the characteristics in calm and rough conditions. For similar characteristics obtained in the «Transit» experiment (Fig. 1b), the contrast is less; the important thing is that they are at the very beginning of the scale, so such a system is suitable for measuring stronger wave values.Thus, the model calculations performed and the experimental studies carried out show the possibility of expanding the range of measuring the degree of sea waves from satellite signals emitting at low elevation angles, using the characteristics of the diffuse component in different frequency ranges. The considered technique can be used for diagnosing waves in the coastal zone as a complement to standard meteorological measurements.

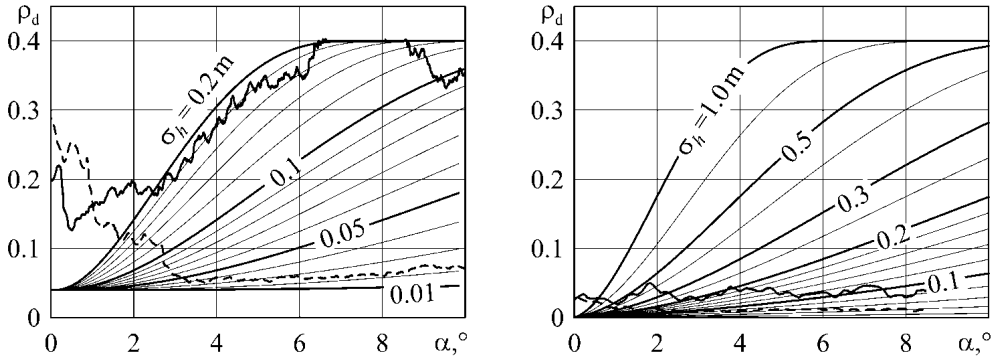

Fig. 1. Comparison of diffuse reflection coefficients obtained in experiments on GPS (a) and «Transit» (b) satellite setting over sea surface, with model calculations (dashed lines - calm, solid lines - moderate waves)

References

[1] Beard C. I., Katz I., Spetner L. M. 1956. Phenomenological vector model of microwave reflection from the ocean. *IRE Trans*. vol. AP-4, iss. 4, pp. 162-167.

[2] Barton D. K, Ward H. G., 1969. Handbook of radar measurements. Prentice-Hall.

[3] Rasskazovsky V. B., Pedenko Yu. A., 2003. Millimeter and centimeter wave field model over the sea to investigate methods for measuring the elevation of low-flying targets. Radiofizika I elektronika. Kharkov: IRE NAS of Ukraine. vol. 8, no. 1, pp. 22-33. (in Russian).

[4] Zamarajev V. B., Kabanov V. A., Morgun G. M., Sinitsky V. B., 2006. Variations of the tropospheric refraction over the sea. Simultaneous measurements at ground-to-ground and satellite-to-ground radio paths. *Telecommunications and Radio Engineering*. vol. 65, no. 8, pp. 685-689.

DETECTION AND RESTORATION OF DIGITAL INFORMATION SIGNAL FROM AMPLITUDE SHIFT KEYING (ASK) RADIO SIGNAL WITH STOCHASTIC NOISE-LIKE CARRIER

Bohdanov R.V.
Faculty of RadioPhysics, Electronics and Computer Systems, Taras Shevchenko National University of Kyiv, Prospect Glushkova, 4g, Kyiv 03022, Ukraine,,
e-mail: roman.bohdanov@knu.ua

Modified "bipolar" LC-oscillator was used as source of stochastic noise-like carrier for informational digital signal with amplitude shift keying (ASK) at Very Low Frequency radio band (30 kHz). Scheme of simple direct gain receiver for VLF ASK with noise-like carrier proposed and simulated.

Previously in [1] LC oscillator with stochastic oscillation noise modes used as carrier source in receiver of range of "Very Low radio Frequencies" (VLF) (3…30) kHz [2], which modulated by amplitude shift keying (ASK) by 4 bit or 5 bit digital informational packages. Simulated in NI Multisim scheme demonstrated stable digital data transmission up to 2 kbits per second at near 30 kHz noise-like carrier. Observed spectrum width of such signal is primarily determined by the spectrum of the noise-like carrier and not directly by informational signal. But this signal still may be received by rather simple direct gain receiver scheme (Fig.1), as informational signal restored to logical levels on NAND Schmitt triggers CD4093BD digital logic elements.

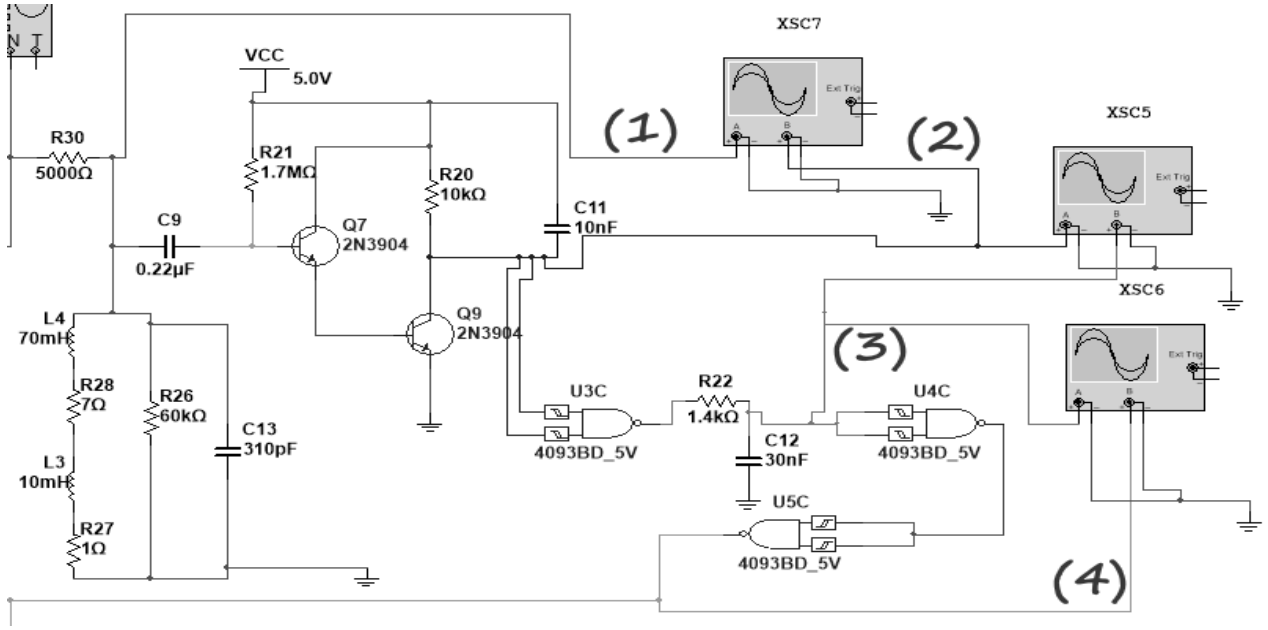

Fig. 1. NI Multisim 13 simulated scheme of direct gain receiver for VLF range with scheme of digital levels of informational signal restoration (elements U3C, U4C, U5C – CD4093BD). Control points: (1) input signal; (2) – amplified and detected signal; (3) – signal after first logical element U3C with restored logical levels after some high frequency noise R22C12 filter; (4)– output digital signal

In current work, in compare with [1], to the receiver added selective parallel oscillating circuit L4L3C13R26R27R28, which has the same resonance frequency as in similar circuit of transmitter output block. Resistor R26 is mostly optional and may be changed for regulation of quality of the oscillating circuit. Bipolar transistors Q7 and Q8 used at such scheme work as non-linear amplifier with high input impedance and amplitude detector. Resistor R30 reduces the interconnection between transmitter and receiver, symbolizing the transmission medium between antennas. Maximum experimental value of R30 on which this receiver is still operational is 18 kΩ because some minimal amplitude of input signal needed (Fig.1(1), Fig.2(1)). Also, some optimization of filters R20C11 and R22C12 regulate duty cycle of output pulses as maximum signal rate of the circuit.

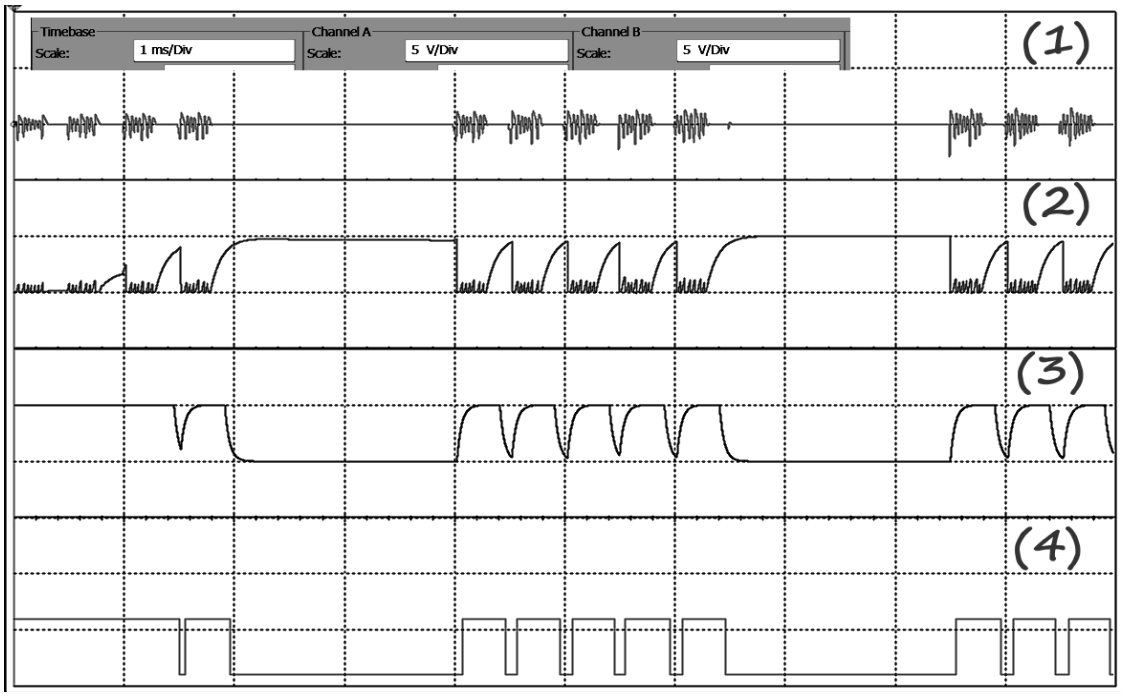

Fig. 2. Oscillograms from control points of scheme of direct direct gain ASK receiver for VLF range (Fig.1) simulated in NI Multisim 13 (R30 = 5 kΩ): (1) input signal; (2) – amplified and detected signal; (3) – signal after first logical element U3C with restored logical levels after some high frequency noise R22C12 filter; (4)– output digital signal.

. An obvious disadvantage of this scheme (Fig. 1) is that the informational signal transmitted by the first packages after the signal came to the receiver's input circuit may be distorted due to certain transient processes in it (Fig.2(2 – 4)). Only the following packages pass completely [1]. This is the result of non-optimal (too low) start voltage on collector of transistor Q9 and the first logical element U3C starts to work just when DC voltage on circuit R20C11 as on collector of Q9 from detection of the signal reached appropriate value near +3…+3.5V. Such start voltage may be reached too at R21 > 125 MΩ.

References

[1] Rasulova I.V. Stochastic noise LC-oscillator in very low frequency (VLF) electromagnetic digital data transmission channel / Rasulova I.V., Bohdanov R.V. // Abstracts of the seventh (XXII) International Young Scientists Conference on Applied Physics, May 24-27, 2022, Kyiv, Ukraine, Faculty of Radio Physics, Electronics and Computer Systems, Taras Shevchenko National University of Kyiv. – 2022. – P. 47–48.

[2] Very low frequency [Electronic resource] // Wikimedia Foundation. – 2022. – Resource access mode: https://en.wikipedia.org/wiki/Very_low_frequency.

REVIEW PEPPER: USAGE OF UNMANNED AERIAL VEHICLES IN 5G NETWORKS

Danuk D. A.*, Al Sharify Mushtaq Talib**
* e-mail: mahavstt@gmail.com
** e-mail: mushtaq.talib2005@gmail.com
***Faculty of RadioPhysics, Electronics and Computer Systems Taras Shevchenko National University of Kyiv, Kyiv 01601, Ukraine

Analythis for main aspects of unmanned aerial vehicles (UAV) usages in 5G wireless networks to research the possible enchantment mobile broadband. Enhanced mobile broadband (eMBB) with bandwidth-consuming, ultra-reliable low-latency communication (URLLC) and massive machine-type communications (mMTC). UAV main requirements as a desirable candidate to substitute or complement terrestrial cellular networks. Our future project is to improve data traffic control for UAV in 5G.

UAV main advantages

As a desirable candidate to substitute or complement terrestrial cellular networks, UAV communications exhibit major attributes as follows[1]:

Line-of-Sight Links: UAVs operating autonomously in the sky have a heigh potential to establish connections with ground users through line-of-sight (LoS) links. This capability greatly enhances the reliability of transmissions over extended distances. Furthermore, UAVs can adapt their hovering positions to ensure the continuity and quality of these links.

Dynamic Deployment Ability: In contrast to stationary ground-based infrastructure, UAVs offer the advantage of dynamic deployment in response to real-time demands. This adaptability makes UAV networks more resilient to changing environmental conditions. Moreover, since aerial Base Stations (BSs) provided by UAVs eliminate the need for land rental costs, they eliminate the requirement for erecting towers and laying cables.

UAV-Based Swarm Networks: A collection of UAVs has the capacity to form scalable multi-UAV networks, providing pervasive connectivity to ground users. This is made possible by the exceptional flexibility and rapid provisioning capabilities of multi-UAV networks. They represent a viable solution for swiftly and efficiently restoring and expanding communication services[2].

Three main categories of UAV usages in 5G wireless networks

According to International Mobile Telecommunications 2020 (IMT-2020), 5G networks are expected to support a diverse variety of use cases in three main pillar categories[3]: Enhanced mobile broadband (eMBB), Ultra-reliable and low-latency communications (URLLC), Massive machine-type communications (mMTC).

eMBB - is designed to support data-intensive applications like virtual and augmented reality (V/AR) that demand high data rates over broad coverage areas. eMBB represents a natural progression from 4G/LTE networks and will offer greater data rates and system capacity compared to current mobile broadband services[4]. While ensuring moderate reliability, such as acceptable packet error rates (PERs), eMBB is expected to enable peak data rates of up to 10 Gbits/s within 5G networks. This capability is well-suited for high-data-rate UAV communication applications, including real-time video streaming and data relay[5].

URLLC - is perfect for mission-critical applications like remote surgery, autonomous vehicles, and the Tactile Internet, where both ultra-high reliability and minimal delays are essential[6-7].

mMTC - is geared towards providing connectivity for an extensive array of power-limited devices with varying traffic profiles, as seen in the industrial Internet of Things (IoT). In this context, UAV-enabled mobile data collectors can play a valuable role by moving in close proximity to IoT devices to gather data, thus minimizing their transmit energy consumption[5].

UAV may play a central role in providing network service recovery in a disaster-stricken region, enhancing public safety networks, or handling other emergency situations when URLLC is required. In particular, UAV-aided eMBB can be regarded as an important complement to the 5G cellular networks. So in conclusion, UAVs are identified as an important component of 5G/B5G wireless technologies[2].

Futures work

Three categories of UAV technologies can be used in our research for improving data traffic control for UAV in 5G.

eMBB aspect of 5G can help ensure that UAVs have access to high-speed, high-capacity connections. This would enable smoother video streaming, faster data transfers, and improved overall communication quality between the UAV and the gNB

URLLC is crucial for applications where low latency and high reliability are paramount, such as remote drone piloting and autonomous UAV operations. By optimizing data traffic control between UAVs and gNBs in real-time, latency can be reduced and ensure that commands and data are transmitted with the utmost reliability. This is particularly important for tasks that require rapid response, like emergency services, surveillance, or critical infrastructure inspection.

While UAVs may not individually represent massive machine-type communications, they can be part of a broader network of connected devices and sensors. The efficient management of data traffic between UAVs and gNBs can help integrate UAVs into the mMTC aspect of 5G, enabling them to seamlessly communicate with other devices and systems. This could be especially useful when multiple UAVs are deployed for collaborative task or when UAVs are used for collecting data from a large number of sensors or IoT devices.

In conclusion all this technologies could be used in our future researches as main aspects of possible enchantment mobile broadband and improving data traffic control for UAV in 5G, since UAV are potential direction of mobile network within 5G.

References

[1] W. Shi, H. Zhou, J. Li, W. Xu, N. Zhang, and X. Shen, “Drone assisted vehicular networks: Architecture, challenges and opportunities,” IEEE Network, vol. 32, no. 3, pp. 130–137, May/Jun. 2018

[2] B. Li, Z. Fei and Y. Zhang, "UAV Communications for 5G and Beyond: Recent Advances and Future Trends," in IEEE Internet of Things Journal, vol. 6, no. 2, pp. 2241-2263, April 2019

[3] M. Shafi, A. F. Molisch, P. J. Smith, T. Haustein, P. Zhu, P. De Silva, F. Tufvesson, A. Benjebbour, and G. Wunder, “5G: A tutorial overview of standards, trials, challenges, deployment, and practice,” IEEE J. Sel. Areas Commun., vol. 35, no. 6, pp. 1201–1221, Jun. 2017

[4] P. Popovski, K. F. Trillingsgaard, O. Simeone, and G. Durisi, “5G wireless network slicing for eMBB, URLLC, and mMTC: A communication-theoretic view,” IEEE Access, vol. 6, pp. 55 765–55 779, 2018

[5] Q. Wu et al., "A Comprehensive Overview on 5G-and-Beyond Networks With UAVs: From Communications to Sensing and Intelligence," in IEEE Journal on Selected Areas in Communications, vol. 39, no. 10, pp. 2912-2945, Oct. 2021

[6] H. Ji, S. Park, J. Yeo, Y. Kim, J. Lee, and B. Shim, “Ultra-reliable and low-latency communications in 5G downlink: Physical layer aspects,” IEEE Wireless Commun., vol. 25, no. 3, pp. 124–130, Jun. 2018

[7] C. She, C. Liu, T. Q. S. Quek, C. Yang, and Y. Li, “Ultra-reliable and low-latency communications in unmanned aerial vehicle communication systems,” IEEE Trans. on Commun., vol. 67, no. 5, pp. 3768–3781, May 2019

LARGE-SCALE GEOMAGNETIC FIELD DISTURBANCES CAUSED BY THE STRONG EXPLOSION OF THE TONGA VOLCANO ON JANUARY 15, 2022

L. F. Chernogor*, M. Yu. Holub*
**V. N. Karazin Kharkiv National University, Ukraine, 61022, Kharkiv, Svoboda Square, 4,*
e-mail: Leonid.F.Chernogor@gmail.com
**V. N. Karazin Kharkiv National University, Ukraine, 61022, Kharkiv, Svoboda Square, 4,*
e-mail: marya160588@gmail.com

The Tonga volcano is located in the southern part of the Pacific Ocean in Polynesia (geographic coordinates: 20.54° S, 175.38° W). Its activity increased sharply on January 15, 2022. Five explosions were observed in the time interval 04:00–05:00 UT. The most intense explosion was at 04:15 UT. It caused registered disturbances in all subsystems of the Earth–atmosphere–ionosphere–magnetosphere system. The results of the analysis of the large-scale geomagnetic field disturbances caused by the explosion of the volcano are presented.

Introduction

The Tonga volcano is located in the ocean at a depth of about 200 m. The volcanic eruption continued from approximately 04:00 UT to 16:00 UT. During this time, 2.9 Gt of eruption products were thrown into the atmosphere. Their volume reached 1.9 km^3. The productivity of the volcano was 67 kt/s or 44 thousand m^3/s. The maximum height of ejections reached 58 km, which is the main feature of the Tonga volcano. According to estimates [1–3], the thermal energy of the volcano was $3.9 \cdot 10^{18}$ J, and the power was 91 TW. In terms of its energy, the Tonga volcano was inferior only to the volcanoes Krakatoa ($5 \cdot 10^{19}$ J) and Pinatubo ($2 \cdot 10^{19}$ J), but the height of the ejections of these volcanoes did not exceed 37–43 km and 40–47 km, respectively. At this time, a number of authors described the results of observations of geomagnetic field variations caused by the explosion of the Tonga volcano. At the same time, the main attention was paid to the analysis of quasi-periodic processes, disturbance of the neutral wind system, ionospheric currents at the heights of the dynamo region of the atmosphere. An urgent task is a more detailed analysis of the magnetic effect of the Tonga volcano using data from the Intermagnet network magnetic stations. The purpose of this work is to analyze the large-scale disturbances of the geomagnetic field caused by the powerful explosion of the Tonga volcano.

Discussion

The X-, Y- and Z-components of the geomagnetic field were subject to analysis. The time resolution was 1 min, the error did not exceed 1 nT. Temporal variations of the geomagnetic field level from January 12 to January 18, 2022 were analyzed. January 13 and January 17, 2022, which were used as reference days, were the most magnetically quiet days. In total, 17 stations were processed: PPT (French Polynesia), EYR (New Zealand), CNB (Australia), CTA (Australia), MCQ (Australia), HON (United States), ASP (Australia), KDU (Australia), IPM (Chile), GNG (Australia), LRM (Australia), KAK (Japan), KNY (Japan), MMB (Japan), SHU (United States), DLT (Vietnam), CKI (Australia). It is important that these stations were located on different sides and at different distances from the volcano. As an example, let us present the temporal variations of the geomagnetic field level accompanying the explosion of the Tonga volcano at the PPT station (distance from the volcano is 2730 km). On the reference days of January 13 and January 17, 2022, in the time interval 03:00–17:00 UT, the X-component level values fluctuated approximately from –12 to –5 nT (Fig. 1). The level of the Y-component increased from –(7–10) to 3–5 nT from 03:00 UT to 05:00 UT. Then it fluctuated within 2–3 nT, gradually decreasing from ~0 to –(20–25) nT. On the day of the volcano explosion, the non-monotonicity of the component level increased, and the fluctuations of their level increased significantly. The trend of all components decreased significantly. The level of the X-component increased from –20 to 10 nT, the Y-component decreased from 10 to –25 nT, and the Z-component decreased from 3 to –10 nT. In addition, six groups of disturbances with delay times $\Delta t_1 \approx 16$ min, $\Delta t_2 \approx 37$ min, $\Delta t_3 \approx 50$ min, $\Delta t_4 \approx 96$ min, $\Delta t_5 \approx 150$ min and $\Delta t_6 \approx 235$ min were observed (Fig. 1). The largest (up to 10 nT) disturbances took place after 14:00 UT. However, they were caused more by a magnetic substorm than by a volcanic eruption.

13.01.2022 **15.01.2022**

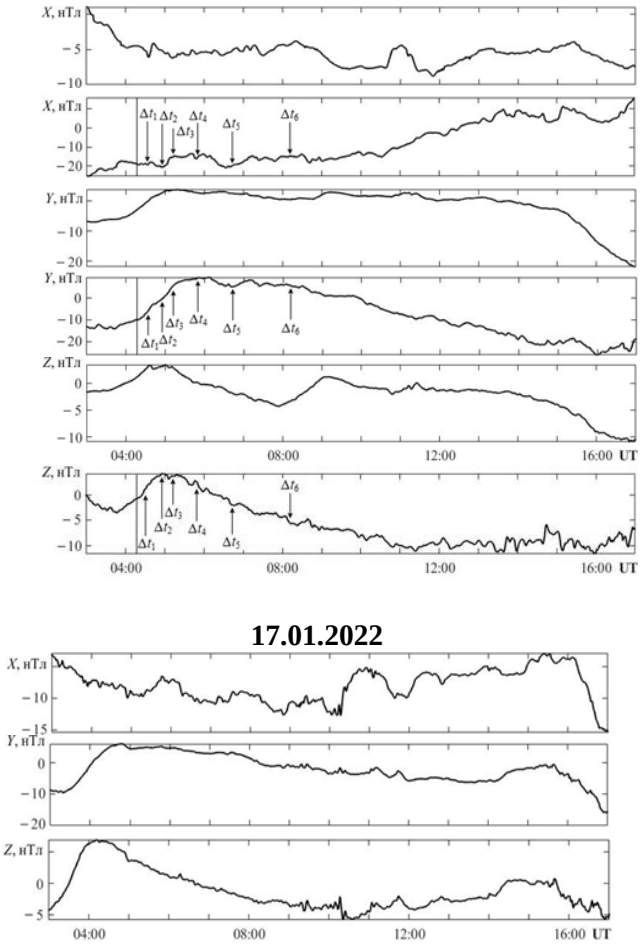

17.01.2022

Fig. 1. Temporal variations of the X-, Y-, and Z-components at the PPT station on the day of the volcano explosion and on reference days. The vertical line marks the moment of the most powerful explosion. Arrows indicate possible moments of magnetic field reaction

Main Results

As a result of the analysis of time variations of the geomagnetic field X-, Y- and Z-components, registered at stations located at a distance of ~2000–8000 km from the epicenter of the Tonga volcano explosion, it was established that the geomagnetic effect was of a global nature. Six groups of geomagnetic field component disturbances that could have been caused by a volcanic explosion were identified. Speeds close to ~4 km/s and 1.5 km/s are characteristic of MHD waves. The speed close to ~1 km/s, is characteristic of an explosive wave. Atmospheric gravity waves have a speed of ~500 m/s. Disturbances with speeds of ~315 m/s and 200 m/s propagated due to Lamb waves and tsunamis. The amplitude of quasi-periodic disturbances of the geomagnetic field was estimated to be 1–10 nT. Such values are in good agreement with the observational results. Estimates of the value of aperiodic disturbances gave a value of 30–60 nT, which was also consistent with the results of measurementsWork by L. F. Chernogor and M. Yu. Holub was supported by the National Research Foundation of Ukraine for financial support (project 2020.02/0015).

References

[1] L. F. Chernogor, “Physical effects of the January 15, 2022, powerful Tonga volcano explosion in the Earth – atmosphere – ionosphere – magnetosphere system,” Space science and technology, vol. 29(2), pp. 54-77, 2023. http://dx.doi.org/10.15407/knit2023.02.054

[2] L. F. Chernogor, “Geophysical Effects of the Tonga Volcano Explosion on January 15, 2022,” in *Proceedings of the 16th International Conference Monitoring of Geological Processes and Ecological Condition of the Environment, Monitoring 2022*. Kyiv, Ukraine, 15 – 18 November 2022. id: 188342. Mon 22-141. https://doi.org/10.3997/2214-4609.2022580141

SYSTEM ADVANTAGES AND FEATURES OF THE USE OF STOCHASTIC PERIODIC COMPLEX PULSE RADIO SIGNALS IN THE SENSING MODES OF A SURVEILLANCE RADAR

V. Kantsedal, A. Mogyla
Dept. of physical principles of radiolocation O.Ya.Usikov Institute for Radiophysics and Electronics of the National Academy of Sciences of Ukraine, Kharkiv 61085, Ukraine, e-mail: vkantsedal9@gmail.com, Moganat1196@gmail.com

The compositions, properties and features of the types of signal resource of a surveillance radar formed by a 3-level system of hierarchical cognitive control of the information content of its sensing modes and their information stability at the stages of reconnaissance of different classes of air targets in different areas of the viewing area and observation conditions are considered. This resource is based on the variety of construction and application of signal-code models of a periodic sequence of broadband unmodulated noise radio pulses with variable sequence parameters, additional randomization of its parameters and imparting increased infierence-protective properties.

Introduction

The cognitive control system forms, in the internal control circuits of its support subsystems with a situationally adaptive form of control, three types of radar signal resources with changing criteria and methods for synthesizing the forms and parameters of probing signals (PS) depending on the radar sensing mode, complex dynamic states of tactical situations (TS) target environment without interference and conflict situations (CS) in conditions of electronic suppression by the airborne RES complex. At the same time, the formulation and solution of the control problem uses the method of synthesizing the "signal shape - matched correlation processing" pair, taking into account the influence of the peculiarities of observation conditions in a particular problem area of the radar coverage area and the possibility of limited use of effective non-adaptive and adaptive means electronic masking (REM) and protection (REP), which built into the transmitting-receiving path.

Types of radar signal resource with changing criteria and methods for synthesizing the forms and parameters of sounding signals

1. Support for the information content of radar sensing modes in a target environment without interference is provided by the type of signal resource $\{S\}_1$ with a variety of forms and parameters of the considered burst PS for adapting current sensing modes to the state of the TS in problem sectors of the viewing area and improving the quality of its selection types. Optimization of the shape of a stochastic PS and its parameters is based on the effects of compression of complex pulses and bursts of them with matched correlation processing of echo signals reflected from air targets of different classes, redundancy of frequency-time parameters and the possibility of independent control of the parameters of the spectrum and temporal structure of the PS using discrete code sequences (DCS). The works [1, 2] consider the preferred methods of forming such mathematical signal-code models of the PS by changing the parameters of the noise pulse and using inter-period control of the types and parameters of time-pulse nonlinear modulation (TPM) of the time frequency structure of the burst by different DCSs with special correlation properties in depending on the needs of the sensing mode and the state of the TS [3]. When comparing ensembles of PS shapes, the differences in their dimensions, structural, correlation and interference-protection properties are taken into account. The ensemble construction of this type of resource of stochastic PS makes it possible to reduce the dimensions of the volume of the signal resource with various forms of PS and the possibility of their expansion, adaptive to changes in the states of the TS. They can serve as an alternative to the use of deterministic complex single discrete coded pulses and bursts of them in the sensing modes of a surveillance radar. For example, the properties of packets of complex pulses with different types of modulation and the use of DCS from various orthogonal ensembles of deterministic DCS can be equivalently represented by one packet of the considered form of stochastic PS. An important point in this regard is the possibility of a rapid transition from one form of the PS to another with a change in its non-energy parameters, such as the base and structure of the signal.

2. Another type of generated signal resource $\{S\}_2$ differs from the one discussed above in that it serves to simultaneously ensure the information content of radar sensing modes and the secrecy of their emissions in

the conditions of conducting electronic reconnaissance of emissions by the airborne RES complex. The use of the PS forms of the previous type of signal resource best (most fully) will respond to the threats of interception and analysis of emissions, if we additionally give it and combine such reconnaissance protective properties that would increase the covert of emissions, complicate or disrupt electronic reconnaissance of emissions from radar probing modes and ensure adequate electronic masking of them. The conditions, methods and means of ensuring energy and structural secrecy related to the forms and parameters of the PS, the structure of its processing and the ability to control them in problematic sectors of the radar coverage area are considered adequately by the threats of RTR interception and analysis of radiation from sensing modes and taking into account their features [4,5]. The use of unusual forms of stochastic probing signals will confuse the means of the RES complex, and their covert emission properties are a decisive factor in the justification their choice.

3. This type of signal resource $\{S\}_3$ differs from the first type of radar signal resource in that it serves to simultaneously ensure the information content and interference (noise) immunity of radar sensing modes in the conditions of RES by various types of active interference after the loss of secrecy of their emissions. The use of the first type of signaling resource will also respond to emerging threats, if we use the opportunity to further increase interference-resistant properties associated with improving selective properties of the PS, which together would make it difficult or disrupt the installation of dangerous types of interference to radar sensing modes and provide adequate electronic protection against them. The conditions, methods and means of increasing reference (noise) immunity related to the forms and parameters of the PS, the structure of its processing and the ability to control them, taking into account the characteristics of the states of the TS and the CS [4,6] in problem areas of the radar coverage area, are considered. It should be noted that the subsystem for supporting interference immunity of radar sensing modes is more complex.

Thus, the peculiarity is that different types of radar signal resources with various forms of PS have different properties in providing the required indicators of information content and interference (noise) immunity of radar sensing modes. Therefore, the choice of a more effective type and parameters of a complex stochastic PS in reconnaissance of an air target and combating an airborne RES complex is a primary task in order to achieve certain structural, correlation and protection properties in accordance with the criteria under consideration.

References

[1] V. Kantsedal, A. Mogyla. Synthesis of Complex Stohastic Radar SignalS witg Deired Cjrrelation Properties. Proceedings of the 18th International Conference on Electronscs and Applied Physics (APHYS 2022), 18-25 October 2022 - Kuivm Ukrain, Taras Shevchenko National University of Kuiv Faculty of Radio Physics, Electronics and Computer System, pp. 124-125.

[2] Mogyla A.A. “The use of stochastic probing radio signals to resolve the “range-velocity” uncertainty in Doppler meteorological radars, (in Russian)”, Izvestiya VUZ. Radioelectronics. 2014, V. 57, No. 12, pp. 30–42.

[3] Geister S.R., Kurenev A.V. Methodology for determining the parameters of a radar sounding signal. Reports of BGUIR, 2006 No. 4 (16), pp. 10-15.

[4] Kantsedal V.M., Mogila A.A. Features of controlling the immunity of a surveillance radar when it is suppressed by active interference and interfering information influences (in Russian). No. 0485-8972 Radiotechnika. 2021, Issue 207, pp. 89-101.

[5] Lukin K.A., Kantsedal V.M. Covert Operation of Surveillance Noise Radar. Proceedings of International Radar Symposium IRS 2006, 24-26 May, Krakow, Poland, pp. 477-480.

[6] Lukin K.A., Kantsedal V.M. Assessment of the influence of synchronous pulse interference on the noise immunity of broadband correlation radar receivers with noise and linear frequency modulation of signals. Applied radio electronics, 2013, volume 12, no. 3, pp. 408-416.

RATIONALE FOR CONSTRUCTION OF THE STRUCTURE OF THE SYSTEM FOR COGNITIVE CONTROL OF TYPES OF SIGNAL RESOURCE SURVEILLANCE RADAR

V. Kantsedal

Dept. of physical principles of radiolocation O.Ya.Usikov Institute for Radiophysics and Electronics of the National Academy of Sciences of Ukraine, Kharkiv 61085, Ukraine, e-mail: vkantsedal9@gmail.com

A rationale is presented, an analysis of the properties is given, the features of the construction of the proposed 3-level structure of a cognitive system for controlling types of signal resource are highlighted to simultaneous support the information content of radar sensing modes and their information stability at the stages of reconnaissance of various classes of air targets, as well as flexible restructuring of the radar structure in complex, fast and unpredictably changing tactical situations of the target environment and conflict situations in conditions of electronic suppression by active and information interference in problem sectors (areas) of the viewing area.

Introduction

From a systemic perspective, the objects and types of conflict interaction, sources of threats to the sensing modes of the surveillance radar and conflict impacts, as well as the uncertainty of its observation conditions [1-4] are considered in order to formalize the problem of cognitive control. The task of the cognitive control system is to develop a model of targeted operation of the radar to eliminate the discrepancy between the observed situation and the control goal, which selects the most advantageous strategy of following the tactical situation (TS) in the target environment and countering conflict situations (CS) created by the suppression strategy air complex RES. Its solution is sought based on the analysis of the changing environment and assessment of the effectiveness of radar actions in real time, using the possibilities of joint implementation in such a system of the functions of cognition, knowledge management and radar signal resource [3] within the framework of a 2-way dynamic model of conflict interaction of radar sensing modes and RES complex systems. The report presents the rationale and diagrams of the proposed structure of a system of hierarchical cognitive control of surveillance radar sensing modes in a complex, rapidly and unpredictably changing TS and CS in a particular problem area of the viewing area with restrictions on the time for making and implementing management decisions and resource costs.

Rationale of the structure of the cognitive control system for sensing modes of a surveillance radar

The proposed block diagram of a 3-level system for cognitive control of types of radar signal resource and the corresponding flexible restructuring of the radar structure is adequate to emerging threats and the effects of the interference-target environment and consists of the following support subsystems operating according to certain rules of sequential integration, belonging to hierarchical levels in ascending order:

- information content of radar sensing modes in complex various TS of the target environment without interference with changing criteria and methods for synthesizing the forms of the probing signal (PS) depending on the needs of the current radar sensing mode;
- at the same time the information content and increased secrecy of the radiation of radar sensing modes in complex different TS and conditions of tracking radar emissions by the RTR system with a change in criteria and methods for synthesizing the forms of PS depending on the current radar sensing mode and system threats (RTR system - ACS_{RES}) of the RES complex;
- at the same time, information content and increased interference immunity of radar sensing modes for various TS and CS using active interference and interfering information influences with a change in criteria and methods for synthesizing PS forms depending on the current radar sensing mode and system threats (ACS_{RES} – RES system) of the RES complex.

The radar signal resource, correlation signal processing algorithms and radar structure restructuring algorithms consist of the types of signal resource and algorithms generated by the support subsystems of the cognitive control system. The task of cognitive control is implemented on the basis of combining a certain composition of the intellectual resource [3,5] and types of radar signal resource - the main tools of the subsystems supporting the cognitive control system in the process of radar observation by selecting (synthesis) the form of the PS with the necessary structural, correlation and interference-protective properties and constructing a control law for the corresponding restructuring of the radar structure and coordinating actions in its sensing modes. A

diagram of a typical structure for constructing support subsystems with the contours of internal and external construction is given, and an analysis of the properties and features of their construction is given.

The features are associated with elements of cognitive control in the information, control and executive means of these circuits, taking into account the content of the CS, the implementation of sequential spatial and temporal processing in the radar structure and the specific needs of the radar sensing modes. The system advantages and features of the use of stochastic periodic complex pulse probing signals are highlighted [6,7]. Their various burst forms are implemented in the circuits of internal reactive cognitive control of support subsystems.. These forms of the probing signal are more acceptable for practice and simultaneously provide information content of the sensing modes of the surveillance radar, increased energy and structural secrecy of their emissions, and increased their interference immunity after loss of secrecy in complex TS in the target environment and CS in conditions of RES with active interference.

The role of information confrontation in a modern radar conflict [2,4], assigned to the contours of external cognitive control with a reflexive form of control of support subsystems for covert active control of the information and control system of the RES complex, is emphasized. At the same time, a targeted influence on the dynamic state of the CS is carried out with the effectiveness of the applied reflexive tactics of information impact management. On the other hand, the presence of conflict-type information influences on the control of radar sensing modes introduces into consideration such a tactical characteristic of the radar as its resistance to covert control by the electronic control complex under the conditions of specific various destabilizing forms of information influences. Setting, solving problems of information confrontation and their implementation is impossible outside of a cognitive control system, which makes the development of such a system especially relevant.

The considered structure for constructing a control system expands the functionality of the radar in the conditions of a complex dynamic radar conflict, more fully takes into account the correspondence of the control objectives of the radar information content of the current radar sensing mode and its stability to the specific conditions of tactical and conflict situations in problem areas of the radar coverage area, and the methods used for solving problems management will allow for greater validity and efficiency of management decisions.

References

[1] Radio-electronic systems: Fundamentals of construction and theory. Directory. Ed. 2nd, revised and additional Ed. I. Shirman. M.: Radiotechnika, 2007, 512 p.

[2] Makarenko S.I. Information confrontation and electronic warfare in network-centric wars of the early 21st century (in Russian). Monograph. St. Petersburg: Science-intensive technologies, 2017, 546 p.

[3] A. D. A. Farina and S. Haykin, Eds. Cognitive Radar: The Knowledge-Fided Fully Adaptive Approach. Oxford,U.K.: IET, 2017.

[4] Kantsedal V.M., Mogyla A.A. Features of controlling the immunity of a surveillance radar when it is suppressed by active interference and interfering information influences (in Russian). N 0485-8972 Radiotechnika. 2021, Issue 207, pp. 89-101.

[5] Labinsky A.Yu., Nefed'ev S.A., Bardulin E.N. The use of fuzzy logic and neural networks in automated control systems (in Russian). Scientific and analytical journal "Bulletin of St. Petersburg University of the State Fire Service of the Ministry of Emergency Situations of Russia", 2019, 1-7, pp. 33-49.

[6] Kantsedal V., Mogyla A. Synthesis of Complex Stohastic Radar SignalS witg Deired Cjrrelation Properties. Proceedings of the 18th International Conference on Electronscs and Applied Physics (APHYS 2022), 18-25 October 2022. Kuivm Ukrain, Taras Shevchenko National University of Kuiv Faculty of Radio Physics, Electronics and Computer System, pp. 124-125.

[7] Mogyla A.A.The use of stochastic probing radio signals to resolve the "range-velocity" uncertainty in Doppler meteorological radars (in Russian). Izvestiya VUZ. Radioelectronics. 2014, V. 57, No. 12, pp. 30–42.

WEAK SIGNAL MODEL AND ITS APPLICABILITY TO THE ANALYSIS OF DISTRIBUTED FIBER OPTIC AMPLIFIER IN TELECOMMUNICATION SYSTEMS

Kononenko A. A. [*], **Zhirov G.B.** [*], **Reznikov M.I.** [**], **Felinskyi G.S.** [**].
Taras Shevchenko National University of Kyiv, Kyiv, Ukraine,
[*] *Faculty of Radio Physics, Electronics and Computer Systems e-mail: kononenkoartem267@gmail.com, genna-g@ukr.net*
[**] *Educational and Scientific Institute of High Technologies e-mail: mirez@ukr.net, felinskyi.gs@gmail.com*

The application limits of the undepleted pumping approximation for the modeling of distributed fiber Raman amplifier (FRA) in single-mode fibers based on silica glass are being considered. Due to results of the introduced criterion, it is proven the using possibility of analytical solutions of the nonlinear problem about the stimulated Raman interaction for modeling of the FRA designed to the operation in optical fiber telecommunication systems. Comparative analysis of the distributed amplification features in two widespread active fibers types, namely G.652 and TrueWave^{RS} *are presented. It is shown despite the twice lower pump efficiency in the standard G.652 fiber, the application range of the weak signal model is significantly expanded, and such modeling results are expected to be reliable up to a pump power of 1660 mW, where the gain bandwidth reaches 26 THz (1.445 - 1.652 μm).*

The modeling problem of the distributed FRA continuously was attracted a lot of attention of researchers and developers worked out the modern telecommunications for the past two decades and it is remains relevant today. In particular, the dynamics of distributed Raman amplification due to the nonlinear power exchange between the pump and the signal is not yet fully explored [1] in the case of single-mode fibers (SMF). Furthermore, modeling such fundamental processes requires new approaches that are free from the limitations of existing methods for solving complex systems of differential equations [2], which involve singular points and have unstable solutions [3]. In our work, it is studied the application limits of an alternative and simplified model of nonlinear optical amplification in typical SMF and modeling results in such active fibers as G.652 and TrueWave^{RS} are presented.

Our modeling is applied for the weak optical signal as it is based on well-known analytical solutions of the two coupled equations described the nonlinear Raman interaction using the undepleted pumping approximation [3]. So for co-propagating pump the distributed on/off gain coefficient for the Stokes signal with initial power of $P_s(0)$ as function of fiber length L, denoted as $G_{on/off}(L) = P_s(L)/P_s(0)$, will be described by a dynamic equation in the form:

$$G_{on/off}(L) = \exp\left(g_R P_0 L_{eff} - \alpha_s L\right), \text{where } L_{eff} = \left[1 - \exp\left(-\alpha_p L\right)\right]/\alpha_p, \quad (1)$$

here, P_0 is represents the initial pumping power at its input into the active fiber, and other designations are described in the notes to Table 1. If one introduced the term of the critical signal power as $P_s^{cr} = (\omega_s/\omega_p)(\alpha_p/g_{R_{max}})$, then the undepleted pumping approximation can be expressed in the form of following inequality:

$$P_s \ll P_s^{cr}. \quad (2)$$

Therefore, the dynamics of distributed Raman amplification are adequately described by equation (1) if the signal power P_s remains significantly below the critical power P_s^{cr} and it should be considered as an important characteristic parameter for a specific fiber. In general, the fulfillment of inequality (2) serves as a criterion for the applicability of the weak-signal model for true description of the distributed FRA dynamics and its design possibilities based on relationships (1).

It is shown the application of the weak signal model is suitable for simulation when the gain coefficient $G_{on/off}$ for a 1 mW signal does not exceed ~216 (23 dB) in standard G.652 fiber and ~76 (19 dB) in TrueWave^{RS} fiber using the direct pump scheme. The model parameters of the distributed FRA in TrueWave^{RS} and G.652 active fibers and some simulation results are presented in Table 1. The comparison of the attenuation (a) and transparency functions of TrueWave^{RS} and G.652 active fibers over the 4 telecommunication windows is illustrated on Fig. 1. It is shown at the critical pumping of P_p = 1660 mW in G.652 fiber, the gain bandwidth extends to 26.01 THz (1.445 - 1.652 μm).

Table 1. Model parameters of the FRA for a monochromatic signal $\lambda_s = 1{,}52$ μm μm and single wavelength of $\lambda_p = 1{,}425$ μm at a pump source.

Parameter	Fiber type	
	G.652	TrueWave^{RS}
1	*2*	*3*
P_s, *mW*	1	1
дБм	0	0
P_s^{cr}, *mW*	215,9	75,8
dBm	23,3	18,8
ω_s, *ТГц*	197,4	197,4
α_s, *dB/km*	0,2	0,2
km $^{-1}$	0,046	0,046
ω_p, *THz*	210,5	210,5
α_p, *dB/ km*	0,4	0,26
km $^{-1}$	0,092	0,060
L_{eff}, *km*	10,9	16,7
$L_{1/2}$, *km*	7,5	11,5
g_{Rmax}, $(W \cdot km)^{-1}$	0,4	0,74
P_{th}, *mW*	115,1	62,3
dBm	20,6	17,9

Notation: P_s, P_s^{cr} are input and critical signal powers; P_{th} is pump threshold power for the net signal amplification at the maximum of the Raman gain profile g_{Rmax}; α_s and α_p are optical attenuation coefficients at the Stokes signal frequency ω_s and pump frequency ω_p, respectively; L_{eff} is effective length of the Raman amplification; $L_{1/2}$ is fiber length to half-power attenuation (3 dB) from the input signal power.

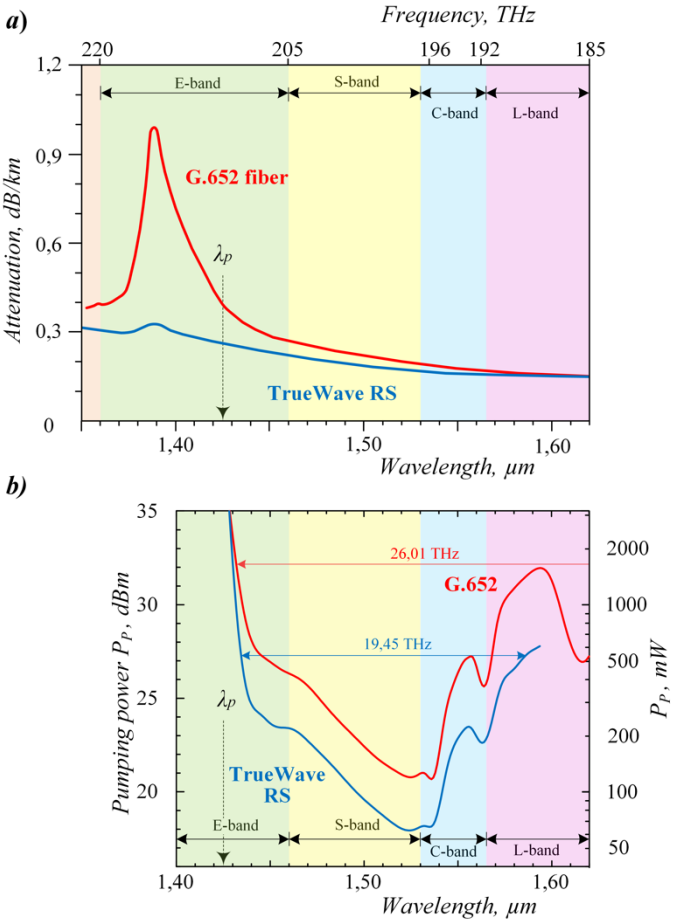

Fig. 1 Optical attenuation (a) and transparency function (b) of TrueWave^{RS} and G.652 active optical fibers in the transparency telecom windows.

In summary, the parameter of the critical signal power P_s^{cr} for the arbitrary active Raman fiber was introduced in our work. It allows to verify in the quantitative form the applicability of the undepleted pumping model in design of FRA and its nonlinear components. By the direct calculations in such active fibers as TrueWave^{RS} and G.652, strict adherence to the specified criterion has been demonstrated, confirming the full suitability of the weak signal model for FRA improvement meat the practical requirements of the long-distance communication systems.

References

[1] A.A. Kononenko, G.B. Zhirov, G.S. Felinskyi, O.I. Tytova Dynamics of distributed Raman gain in telecommunication True Wave^{RS} and G.652 fibers Proc. XXIII Int. Young Scientists' Conf. on Applied Physics, ICAP 2023, May, 16-20, 2023, Kyiv, Ukraine, p. 141-142.was

[2] J. Yao and H. Deng. "Fiber Raman Amplifier Based on Improved Whale Algorithm" The 2nd International Conference on Electronic Information and Communication Engineering (EICE 2023) 13- 15 Jan 2022 Guangzhou, China, J. Phys.: Conf. Ser. 2525 012016, 2023 DOI: 10.1088/1742-6596/2525/1/012016

[3] V.I. Gryhoruk, P.A. Korotkov, G.S. Felinskyi. Nonlinear and Laser Processes in Optical Fibers. – Kyiv: Publishing and printing center 'Kyiv University', 2008. – 576 p.

DICOM VIEWER FOR WEB IMPLEMENTATION OF TELEMEDICINE APPLICATIONS

M. Kononov *, V. Kononov **
Taras Shevchenko National University of Kyiv, Volodymyrska str.,64/13,
** e-mail: m_v_k@univ.kiev.ua*
*** e-mail: viktor1998kononov@gmail.com*

In order to implement telemedicine applications based on web architecture, a software module has been developed that can be embedded in the system of remote access to graphic and auxiliary text data contained in files of DICOM format. Performed testing showed an acceptable delay time of data processing of the diagnostic file exclusively on the server.

Use of diagnostic data in telemedicine

One of the relevant, including for Ukraine [1], ways to increase the effectiveness of medicine is the use of electronic communication means for medical needs, i.e. telemedicine. In modern society, the use of electronic communications is one of the factors of speeding up various types of business. One of the activity types that requires rapid processing of information is medical diagnostics. There are some directions in telemedicine that actively use remote access to the results of instrumental diagnostics. This allows providing teleconsultation, remote training of medical personnel and remote diagnostics. Note that for the needs of diagnostics and training, it is possible to use examinations with big number of frames or several examinations from database with metadata accompanying graphical data of each frame.

The complex structure of diagnostic data requires the use of appropriate structuring of the file. One of the most widely used formats for storing and forwarding of graphic diagnostic data DICOM [2] use the data formatting in the form of a hierarchical list of tags. Most modern diagnostic devices support this format, but its use in remote mode requires the additional software using. Thus, for the implementation of telemedicine systems, there is a necessity to develop modules with such functionality. It is interesting to consider the implementation of DICOM data viewing tools based on client-server architecture (web technologies). At the same time, an additional functionality should be to ensure information security requirements, i.e. the ability to close access to some denied blocks of data contained in DICOM files.

Application architecture

It is proposed to implement access to diagnostic data in DICOM format through a browser without the use of plugins, i.e. exclusively on the basis of data preparation on the server. Accordingly the client side perform, only the visualization of graphics and meta-data from the file stored on the serve. For this purpose, the data from the file, which is reproduced on the client side as an image, must be converted into a graphic file of a format acceptable to the browser. Note what is desirable, when a client request requires only a change in rendering parameters for 16-bit grayscale images, the server must recalculate the body of the image without completely refreshing the page in the browser. Realization of such functionality can be done by AJAX [3]. Formatting of other (text) data from the file into a form acceptable for display in the browser must also be performed on the server. Such architecture provides the blocking of access denied tags in a more secure part of the system.

The most resource-intensive part of data processing is the calculation of the image body. Accordingly, the use of the traditional for the server side coding script languages (PHP or Python) for this purpose is unacceptable. Thus, from the web processor to which the client addresses, it is necessary to forward a task to an additional software component (DICOM processor), which is implemented with faster technology. Microsoft.Net (language C#) was chosen, although data processing can be transferred to C++ to reach even greater speed. According to the proposed architecture, the DICOM processor is single-threaded. Full use of server hardware resources is provided by launching a separate process for each session. To exchange data between the components of the server side (for the command and the results of its execution), auxiliary files are used in a separate directory for each session. This allows you to scale the project.

Implementation of DICOM format data processing

The DICOM specification defines that data is organized as a sequence of data elements (tags). A tag identifier is a pair of unsigned 16-bit numbers (the group number and the element number in the group). Groups in data sequence and tags within each group are ordered by ascending numbers. The tag identifier is assigned a certain content purpose. The next tag field is VR of character type and two-byte length. It specifies a data type from the list defined in this standard. Next comes, the VF field - the byte length of the tag data. If the VR field is present, this field is a 16-bit number and if VR is absent, it is a 32-bit number.

A separate C# class was created to implement DICOM format file data preparation on the server, which performs structuring of file data in the form of a list, each element of which is an instance of a class whose structure includes all tag fields. The tag data entered into the program in this way is convenient for manipulation and selection from the list of data needed to render the image, but is not acceptable for display for the user, because text values are required instead of conditional codes stored in a file. Some dictionary can be used for transcoding. A separate method of this class is used to generate the text that is provided to the user. It creates a long string in which the data of the necessary tags is accumulated already in a form acceptable for viewing by the user. During forming this string, individual tags that should be blocked for viewing are not included. In this form, meta-data can be sent to the client side without the need for processing in the browser.

Support for 8- and 16-bit grayscale images was provided for visualization of the graphic component of the DICOM file. In most cases, a series of examination images is saved as a group of files in a folder. But additionally, the standard supports multi-frame files, in which, with a common set of other tags, there is a combined graphic data tag, i.e. consecutively recorded in one data block all frames of examination. To support this format, the number of the active frame and its size are taken into account for calculation an offset.

Test results

The main task of the test was to evaluate the delay when making a request to the server to select a file or change the image playback parameters. At the same time, the most resource-intensive is the recalculation of graphic data. For testing, a computer with Windows 10 OS (21H2) and an Intel Core i5 10400 processor with a clock speed of 2.9/4.3 GHz was used. The parallelism of data processing (the number of processor threads) in this case does not matter, since the main software module is single-threaded. We will remind that within the framework of the architecture of this project, the use of server multi-core is implemented at the level of simultaneous service of several sessions. The web server (Apache 2.4.23) and the browser (Google Chrome 114.0.5735.199) were running on the same computer. This excludes the delay of the network connection and the observed delay is determined only by the time of data processing on the server.

The delay from start the request to the update in the browser window of the list of tags is not visually observed at all. The delay for updating the image when changing playback parameters does not exceed 0.1–0.2 seconds, so, it does not cause much of a discomfort. Thus, the proposed two-level processing technology on the server of DICOM files does not significantly slow down the work. So, the software components developed in this work are acceptable for use in creating a system of teleconsultations or remote diagnostics.

References

[1] On the organization of the provision of medical care using telemedicine under martial law (order of the Ministry of Health of Ukraine No. 1062 dated 20.06.2022) https://zakon.rada.gov.ua/laws/show/z0728-22#Text

[2] DICOM – https://www.dicomstandard.org/current

[3] W3schoolsUA (Ajax) – https://w3schoolsua.github.io/js/js_ajax_intro.html

THE COMPACT POLARIZATION SEPARATOR FOR WEATHER RADAR

V. Glamazdin, M. Natarov, O. Shubnyi, A. Mogyla
Dept. of physical principles of radiolocation O.Ya.Usikov Institute for Radiophysics and Electronics of the National Academy of Sciences of Ukraine, Kharkiv 61085, Ukraine, e-mail: m.nataroff@gmail.com, moganat1196@gmail.com

Compact parabolic antenna feed system with separation of linear polarization signals has been developed on the base of orthomode transducer design. The device has a good level of matching of all ports and a potentially high level of isolation between ports for orthogonal polarization signals. The feed system is designed for use in the wearther radar.

Introduction

Many designs of signal splitters of the orthogonal polarization signals, linear and circular are known [1-2]. Basically, these structures in the microwave range are divided into quasi-optical and waveguide devices. The presented work is based on the waveguide design which are usually called as "orthomode transducer" (OMT) [3]. The device described in this work was developed for use in the mm wave range, namely at frequencies of 34-36 GHz, where the wavelength in free space is 8.8-8.3 mm. The purpose of this report is to describe the development of a compact linear polarization splitter for C-band radio waves in the frequency band 7 – 7.3 GHz. Polarization splitter is the part of parabolic antenna feed that located in the parabola focus. Feed system must be compact in order to minimally obscure the antenna aperture.

The principle of operation and design

Since the goal of the work is to develop OMT for use at frequencies of 7 - 7.5 GHz, where the wavelength in free space is approximately 43 - 40 mm, simple scaling of the device described in [3] will lead to excessively large device sizes. And in order for the OMT to be an integral part of the parabolic antenna feed, it is necessary to minimize its dimensions.

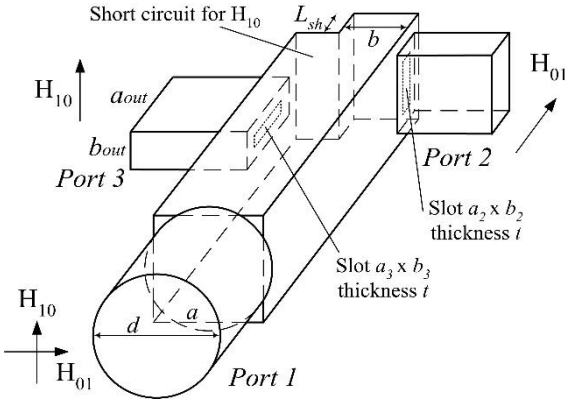

Fig. 1. Schematic diagram of the OMT design

Let's consider the proposed scheme of OMT keeping most of the notations introduced in [3] (fig. 1).The main polarization waveguide mode of the main polarization H_{01} from the conical horn passes through the circular waveguide with a diameter d (Port1) into a square waveguide with dimensions $\boldsymbol{a}\times\boldsymbol{a}$. This waveguide mode almost does not interact with a longitudinal slot with dimensions $\boldsymbol{a_3}\times\boldsymbol{b_3}\times\boldsymbol{t}$ cut in the middle of the wall of a square waveguide, due to the small size of b3 compared to the wavelength and the location of the slot along the currents on the waveguide wall. Behind the slot is a step that acts as a transformator for H_{01} mode. in Port2. The cross-polarization waveguide mode H_{10} also enters the square waveguide from the circular waveguide, but passes through the slot to Port3. The step acts as a short circuit because the size b is chosen so that the H_{10} mode cannot propagate in the waveguide. Thanks to the short-circuit, there is an agreement between Port1 and Port3. Port2 and Port3 are standard waveguides with a cross-section $\boldsymbol{a_{out}}\times\boldsymbol{b_{out}}$ equal to 28.5×12.6 mm

This layout of OMT turned out to be quite compact. In addition, the circular waveguide is connected to the square waveguide, and the distance to the slot of port 3 and to the step is chosen to achieve the maximum matching between Port1 and Port2 and Port3. The final optimization of the device dimensions in order to achieve a return loss level of no more than -20 dB on each of the ports in the 7-7.3 GHz frequency band was carried out using the COMSOL package. The main dimensions of the structure (Fig. 1) are as follows: a=26 mm, b=16.1 mm, d=30 mm, a2=21.4 mm, b2=3.8 mm, a3=26 mm, b3=5.3 mm, t=1 mm, the total length of the square waveguide is 64.1 mm. With such dimensions, the combination of a conical horn with an OMT forms a compact irradiator of a parabolic antenna with separation of the linear polarization signals. This design provides for the output of signals of different polarizations on different sides of the parabolic antenna to the receiver.

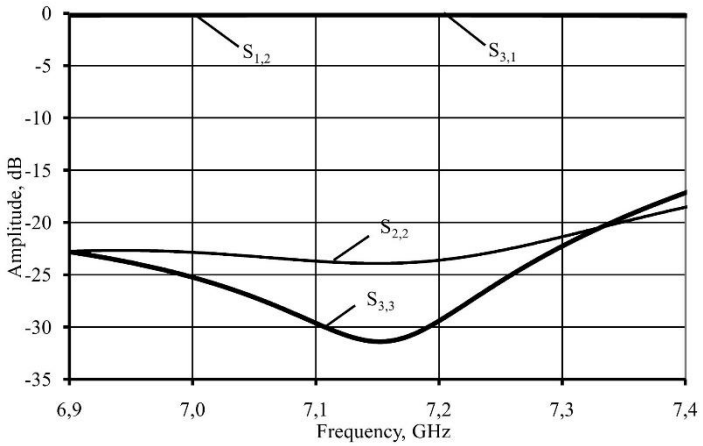

Fig. 2. Reflection and transmission coefficients vs frequency

The calculated frequency characteristics of the reflection ($S_{2,2}$, $S_{3,3}$) and transmission ($S_{1,2}$, $S_{3,1}$) coefficients from Port1 to Port2 and Port3 for modes H_{01} and H_{10} are shown in fig. 2. The calculated reflection coefficients of Port1, Port2 and Port3 are less then -20dB in the frequency band 7-7.3 GHz . The isolation between Port 2 and Port3 in the idealized model, which was investigated in the work, with the symmetrical arrangement of the port3 gap and the symmetrical connection of the circular waveguide to the square waveguide, is more than 150 dB. In a real device, isolation will depend on manufacturing accuracy and is expected to be more than 40 dB.

Thus, in the presented work compact parabolic antenna feed system with separation of linear polarization signals was developed. The device has a good level of matching of all ports and a potentially high level of isolation between ports of orthogonal polarization signals.

References

[1] J. Uher, J. Bornemann, and U. Rosenberg, “Waveguide Components for Antenna Feed Systems: Theory and CAD”, Norwood, MA: Artech House, 1993.

[2] W.A.Imbriale, Large Antennas of the Deep Space Network. Monograph 4. Deep–Space Communications and Navigation Series. Jet Propulsion Laboratory, California Institute of Technology, 2002.

[3] M.P.Natarov, L.A.Rud, V.I.Tkachenko, “Orthomode transducer for MM-wave range”, MSMW’2004 Symposium Proceedings. Kharkov, Ukraine, June 21-24, 2004, vol. 2, pp. 641-643.

INFLUENCE OF STOCHASTICALLY DISTRIBUTED ENVIRONMENTAL PARAMETERS TO THE DETERMINISTIC SIGNAL

Olszewski S.V.*, Lysyuk Yu.V.*
**Taras Shevchenko National University of Kyiv, 64/13, Volodymyrska Street, City of Kyiv, Ukraine, 01601,*
e-mail: olszewski.serge@gmail.com
e-mail: grishaeva-yulia@ukr.net

In the work on the example of a plasma layer with a randomly distributed concentration in the volume, the simulation of the influence of the stochastic environment on the shape of a rectangular pulse was carried out. It is established that this nature of the environment affects the signal as a phase interference, that significantly distorts its shape. It is shown that such an interference does not add noise power to signal but converts its own power of the deterministic signal into noise power. In this case, SNR decrease faster than the variance of a randomly distributed parameter increases.

Introduction

The reliable transmission of information by channels of telecommunication in the spread of signals in the conditions of intensive interference caused by stochastic perturbations of the environment is until the end of an unresolved problem, which has remained relevant and now. These are, in particular, ground and satellite radio communication in the conditions of ionospheric breaks and high -rise nuclear explosions. It is the technical protection of information channels of any nature in conditions of active counteraction to a militaristic nature. This is a connection with space modules when they enter the atmosphere layers and interplanetary communication in the near future. In order to solve the individual components of this global problem, it is proposed to model the influence of plasma volume with a randomly distributed concentration on the spread of rectangular pulse through it.

Physical model

A plasma volume with chaotically distributed concentration is chosen for the stochastic environment. Within this model, the stochastic environment is dispersed. The stochastic volume parameter is selected by the refraction of the electromagnetic wave, which is a function of frequency $\eta(\omega)$. A rectangular impulse is considered as a superposition of harmonic flat electromagnetic waves: $s(t)=\sum_{i=1}^{\infty} A_i e^{-j(\omega_i t+\varphi_i)}$. The spread of electromagnetic waves through the plasma is considered in conditions of slight extinction. The impact of such an environment is to change the raising of the phase of each harmonic of a complex signal in each element of the plasma volume randomly. The final signal on the receiving aperture is formed as a total signal in the mode of multi -channel distribution through individual sections of plasma formation. In the general case, the phase assault in a small element of plasma, for which refractive index is considered homogeneous, looks like:

$$\Delta\varphi(\omega)=\left(\beta(\omega)-\frac{\omega}{c}\right)\Delta z$$

where

$$\beta(\omega)=\frac{\sqrt{2}}{2}\frac{\omega}{c}\left(1-\frac{\omega_0^2}{\omega^2+\nu^2}+\left(\left(1-\frac{\omega_0^2}{\omega^2+\nu^2}\right)^2+\frac{\nu^2}{\omega^2}\left(\frac{\omega_0^2}{\omega^2+\nu^2}\right)^2\right)^{1/2}\right)^{1/2} \quad [1]$$

in here $\omega_0=\sqrt{4\pi n_e e^2/m_e}$ [1] – plasma frequency; $\nu\approx n_a\sqrt{2kT_e/m_e}\,3.5\times10^{-16}$ [2] – the frequency of collisions of electrons with neutral atoms; e, m_e, T_e – the charge, electron mass and temperature; n_a – the neutral atoms concentration; k – the Boltsman's constant. The plasma layer was viewed as thick. That is, when the signal spreads along a separate channel through the plasma, there is a cumulative accumulation of the random raid of the phase of each harmonic from each small element of the plasma along the wave vector. The final signal on the receiving aperture is formed as a total signal in the mode of multi -channel distribution through individual sections of plasma formation. The raid in each phase channel between the space between the plasma volume and the receiving aperture was calculated as a

deterministic value determined by the system geometry without disperse.

The simulation model

A three -dimensional array of dimension [M, N, L], where M = N = 100000 and L = 100, is ruled by the stochastic environment model. On the platform R it is an object array (…, c (M, N, L)). Each element of the array is an elementary volume of the environment. It retains the value of the concentration of plasma.

The model of the receiving aperture is ruled by a two-dimensional array of dimension [R, c], where R = C = 100. On the platform R it is Matrix (0, R, C). The signal in the aperture is formed on the principle of superposition and is equal to the algebraic sum of the signals formed in each element of the aperture. The signal in the aperture element is formed as the geometric sum of the signals detained over each plasma volume. The delay in time of signals is proportional to the distance from the element of the plasma volume to the element.

The initial step of the calculation procedure is the generation of a vector with a test signal. The next step is the formation of a vector of a distorted and detained signal that has passed through the current element of ionospheric plasma. This signal is added to the current element of iteration by all elements of the plasma volume, taking into account the distance between the volume element and the aperture element form a signal in the current element of the aperture. Similar calculations are made for all elements of the aperture. Having made the signals formed in all the elements of the aperture, they received the final signal.

Results and discussion

As a result of the studies, it was found that a stochastic environment on the signal form is quite strong. Thus, the size of the stochastic parameter is an order of magnitude less than the power of the deterministic signal, there is a loss of initial shape more than 10%. Fig.1. represents the distorted stochastic environment signals.

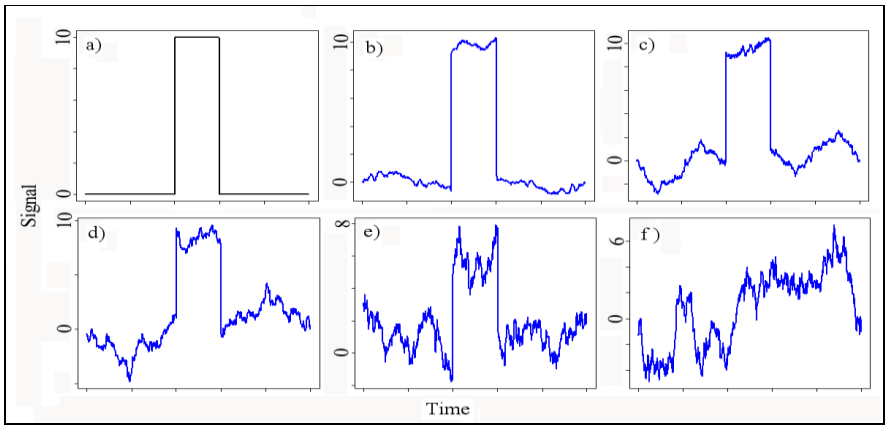

Fig.1. Distorted stochastic environment signals.

Graph a) corresponds to an undistorted deterministic signal. The power of signals on the graphs b) -e) exceeds the noise of the stochastic parameter of 10, 5, 3 and 2 times-respectively. Graph f) corresponds to the case when the noise power of the stochastic parameter is equal to the power of the deterministic signal. Analysis of the average power of the distorted signal showed that it retains the average power of the output deterministic signal to 5%.

Conclusions

It is established that this nature of the environment affects the signal as a phase interference, that significantly distorts its shape. It is shown that such an interference does not add noise power to signal but converts its own power of the deterministic signal into noise power. In this case, SNR decrease faster than the variance of a randomly distributed parameter increases.

References

[1] Особливості використання мікрохвильових методів для діагностики запорошеної плазми. і. діелектрична проникність, показники заломлення та поглинання/Ю.В. Ковтун, А.І. Скибенко, Є.І. Скібенко, Є.В. Сюсько//ISSN 2071-0194. Укр. фіз. журн. 2019. Т. 64, № 5, с.с. 378-389.

[2] Quantum-Mechanical Calculations of Cross Sections for Electron Collisions With Atoms and Molecules/Klaus Bartschat, Jonathan Tennyson, Oleg Zatsarinny//Plasma Process. Polym. 2017, 14, 1600093, p.p. 1-13..

GYROSCOPIC COUPLING IN THE OUTPUT SIGNAL OF A GYROSCOPE MEMS SENSOR

R. Andriichuk, V. Boretskij
Taras Shevchenko National University of Kyiv, 64/13, Volodymyrska Street, Kyiv, Ukraine,
e-mail: r.andriichuck@gmail.com

A vibration stand was created for the purpose of generating controlled angular disturbances for a studied array of 13 MEMS gyroscopes. The developed platform allows for assessing the impact of the noise component on the spectrum of the output signal of the measurement system.

Introduction

Using a gyroscope array consisting of several uniform and affordable MEMS gyroscopes has proven to be an effective method for reducing measurement errors and enhancing the navigation performance of inertial sensors by harnessing redundant information [1-2]. Unfortunately, using such sensors requires a thorough analysis of the resulting signal to identify various types of parasitic signal components, such as those arising from gyroscopic coupling, for instance [3]. This work is part of developing an image registration gyro stabilization system for vehicles such as automobiles and Unmanned Aerial Vehicles (UAVs).

Experimental setup

The output signals from 13 MEMS gyroscopes were simplified by calibrating each sensor and calculating the average of their simultaneous readings. This method allows for multiple measurements of a physical quantity with the aim of reducing measurement errors. To replicate real-world conditions for testing the use of such an inertial navigation device with the sensor array, a brushless DC (BLDC) outrunner motor was integrated. This motor generated vibrations and angular disturbances by cyclically accelerating and decelerating its outer shaft.

The STM32F407VET6 microcontroller is utilized as the core of the data acquisition system, which gathers data from 13 gyroscope sensors using the SPI interface that is clocked at 10 MHz. Once the controller has polled each sensor, it transmits the data to the PC via the COM interface before initiating a new data collection cycle. Data is collected at a frequency of 1.33 kHz from each LSM6DS3 sensor from ST Semiconductor. This frequency is selected to ensure optimal performance of the data collection system. Each sensor is set to a resolution of ±125 degrees per second (DPS), and data recording is carried out from three sensor axes. The data collection is divided into 16 sessions, each lasting 60 seconds. To minimize the impact of additional high-frequency vibrations that may occur during the experiment, the sensor array and the source of vibrations are firmly mounted on a polypropylene foam plate. The sensor array is designed for use in image registration gyro stabilizers, and the vibrations are generated at a frequency of 80Hz, which is close to the oscillation frequency of internal combustion engine movements in vehicles. The axis of the rotational process of the vibration motor is parallel to the Z-axis of each sensor in the array, and this axis is perpendicular to the plane of the sensor.

Results and Discussions

After performing several experiments, 16 datasets were obtained. These datasets contain information about the ordinal number of each measurement cycle to verify the integrity of the acquired data. Additionally, they contain data on angular acceleration values from each sensor in the array in the format Z-Y-X, represented in integer format. This integer format was chosen to optimize the computational resources of the microcontroller in the data collection system and achieve maximum speed. The measurement results were converted into degrees per second (DPS) on a PC by recalculating the collected data from the data collection system.

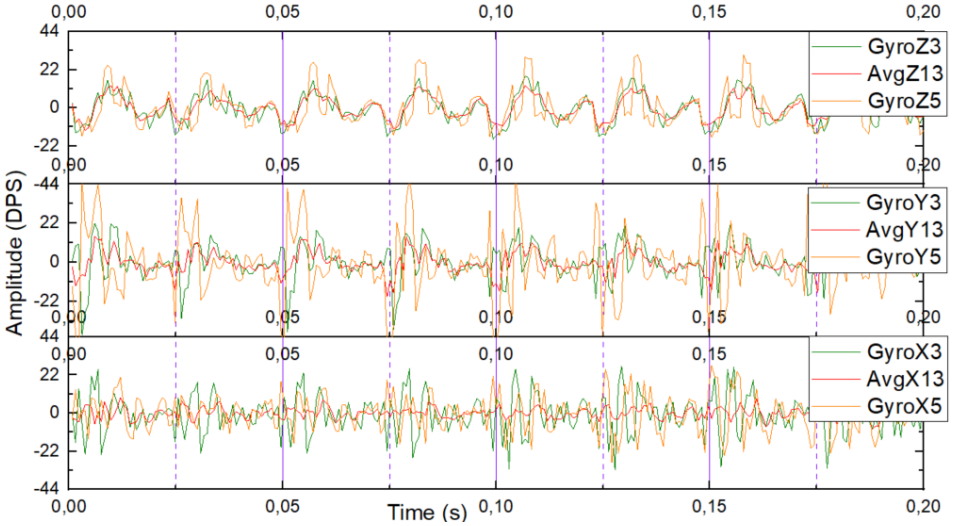

Fig. 1. The readings of individual gyroscopes from the averaged value.

Analyzing the curves depicted in Fig. 1, it's important to note that the high correlation of disturbances along the Y-axis with the Z-axis.

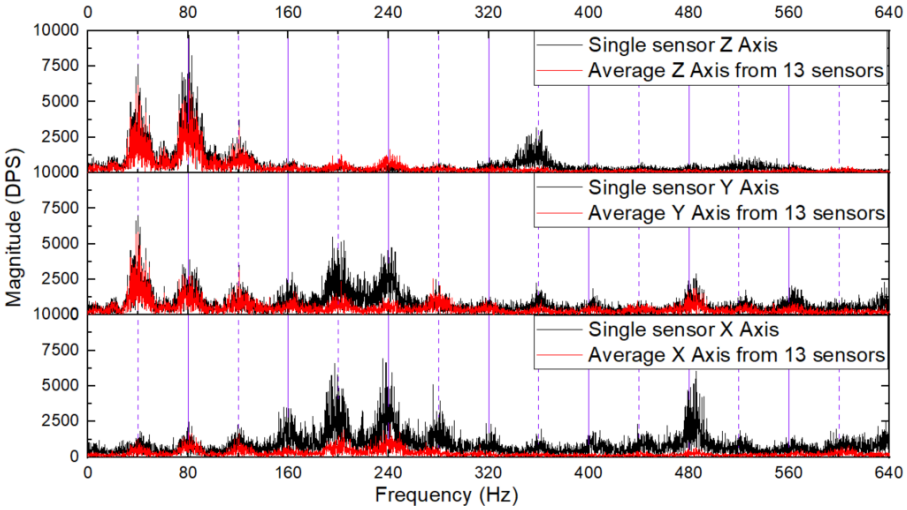

Fig. 2. Frequency components of the received signal.

After examining the frequency components of the signals recorded during the experiment displayed in Fig. 2, it is clear that the most prominent frequency components are present at around 40Hz and 80Hz. These components maintain their shape and magnitude even after averaging the readings from the entire sensor array. Nevertheless, the motor disturbance was applied only to the Z-axis, one can observe in Fig. 2 disturbance impact on both the X and Y axes. Such behaviour can be caused by two possible reasons: uncertainty between axis arrangement between sensors, as well as, the gyroscopic coupling effect between the axes of each sensor. The averaging of sensors data significantly decreases the values of signals for X and Y axes. Especially for the higher harmonics (more than 160 Hz). But the signals on 40, 80 and 120 Hz remain prominent. Such behavior after data averaging leads us to assume that it can be explained by gyroscopic coupling effect.

References

1. H. Li, X. Xiao and P. Peng, "Gyroscope Array Analysis Based on EMKF Algorithm," 2023 42nd Chinese Control Conference (CCC), Tianjin, China, 2023, pp. 3279-3284, doi: 10.23919/CCC58697.2023.10240851.
2. L. Wang, H. Tang, T. Zhang, Q. Chen, J. Shi and X. Niu, "Improving the Navigation Performance of the MEMS IMU Array by Precise Calibration," in IEEE Sensors Journal, vol. 21, no. 22, pp. 26050-26058, 15 Nov.15, 2021, doi: 10.1109/JSEN.2021.3118455.
3. M. Morlans, J. Guérard and J. Juillard, "Characterization of electrical and mechanical coupling in MEMS gyroscopes with electrical measurements," 2021 Symposium on Design, Test, Integration & Packaging of MEMS and MOEMS (DTIP), Paris, France, 2021, pp. 01-04, doi: 10.1109/DTIP54218.2021.9568500.

GEOMAGNETIC EFFECTS OF KYIV METEOROID

Chernogor L. F., Shevelev M. B., Tilichenko N. M.
** School of Radiophysics, Biomedical Electronics and Computer Systems*
V. N. Karazin Kharkiv National University, 61022, Svobody Sq., 4, e-mail: chernogor@karazin.ua
*** e-mail: mykyta.b.shevelev@karazin.ua*
**** e-mail: tilichenko2021rr11@student.karazin.ua*

The results of the analysis of temporal variations of the geomagnetic field at the Lviv, Belsk, Surlari, and Hurbanovo stations, which accompanied the fall and explosion of the cosmic body, are described. The value of the variations was units of nanotesla.

Introduction

A space object entered the atmosphere over Kyiv region, Ukraine on April 19, 2023 at 18:57:20 UTC. The author [1–3] called it the Kyiv meteoroid. There was a cascading destruction of the body, which was accompanied by five thermal explosions of large fragments, in the height range of 38–28 km. According to International Meteor Organisation [4] coordinates of the most powerful explosion are: 49.5°N, 29.9°E. The speed of the meteoroid was equal to 29 km/s. According to the author's estimations [1–3], the glow energy reached 25.2±2.5 GJ, and the initial kinetic energy was 0.09±0.01 kt TNT ≈ 375±35 GJ. With a body weight of 0.89±0.09 t, the volume was close to 0.25±0.025 m^3, and its size did not exceed 79±3 cm. The angle of inclination of the trajectory to the horizon was 32°. Preliminary results of research of the Kyiv meteoroid are briefly published in works [5, 6].

The author [1–3] performed a complex simulation of the main physical effects in all geospheres caused by the fall and explosion of a meteoroid. In [1], the energetics of processes, mechanical, optical, and gas-dynamic effects are analyzed. An estimate of thermodynamic and plasma effects, as well as turbulence effects, is given in [2]. The work [3] is devoted to the evaluation of magnetic, electric, electromagnetic, ionospheric and seismic effects, as well as the effects of acoustic-gravitational waves. In particular, it is shown that the fall and explosion of the meteoroid should have been accompanied by the generation of aperiodic and quasi-periodic variations of the geomagnetic field with a magnitude of several nanoteslas.

Analysis Results

To find the reaction of the geomagnetic field to the fall and explosion of the Kyiv meteoroid, the temporal dependences of the variations of the *X*-, *Y*- and *Z*-components of the geomagnetic field, registered at the stations closest to the trajectory of the space body. The measurements recording from the stations such as Lviv (49.9000°N, 23.7500°E), Belsk (51.8360°N, 20.7890°E), Surlari (44.6800°N, 26.2500°E), Gurbanovo (47.8730°N, 18.1900°E) were used. At the same time, the distances from Kyiv to Lviv, and from Kyiv to other observation sites were 486 km, 695 km, 716 km, 940 km respectively. The time resolution was 1 min, and the amplitude resolution was 1 nT.

An example of wave variations of the level of the *X*-component on the days of the meteoroid fall and on the reference days is shown in Fig. 1. It can be seen that after the explosion of the Kyiv meteoroid, there was a bay-like decrease in the level per unit of nanotesla, as well as quasi-periodic variations with an amplitude of about 1 nT and a period of 3–15 min. Note that variations in the levels of *Y*- and *Z*-components were expressed less clearly.

Main Results

The reaction of the geomagnetic field to the fall and explosion of the Kyiv meteoroid was revealed. The largest variations, which reached nanotesla units, were observed in the *X*-component (from North to South). In addition to the bay-shaped decrease in the level, there were quasi-periodic disturbances with an amplitude of about 1 nT of the geomagnetic field level. In general, the results of the observations corresponded to the theoretical estimates of the magnitude of the effect.

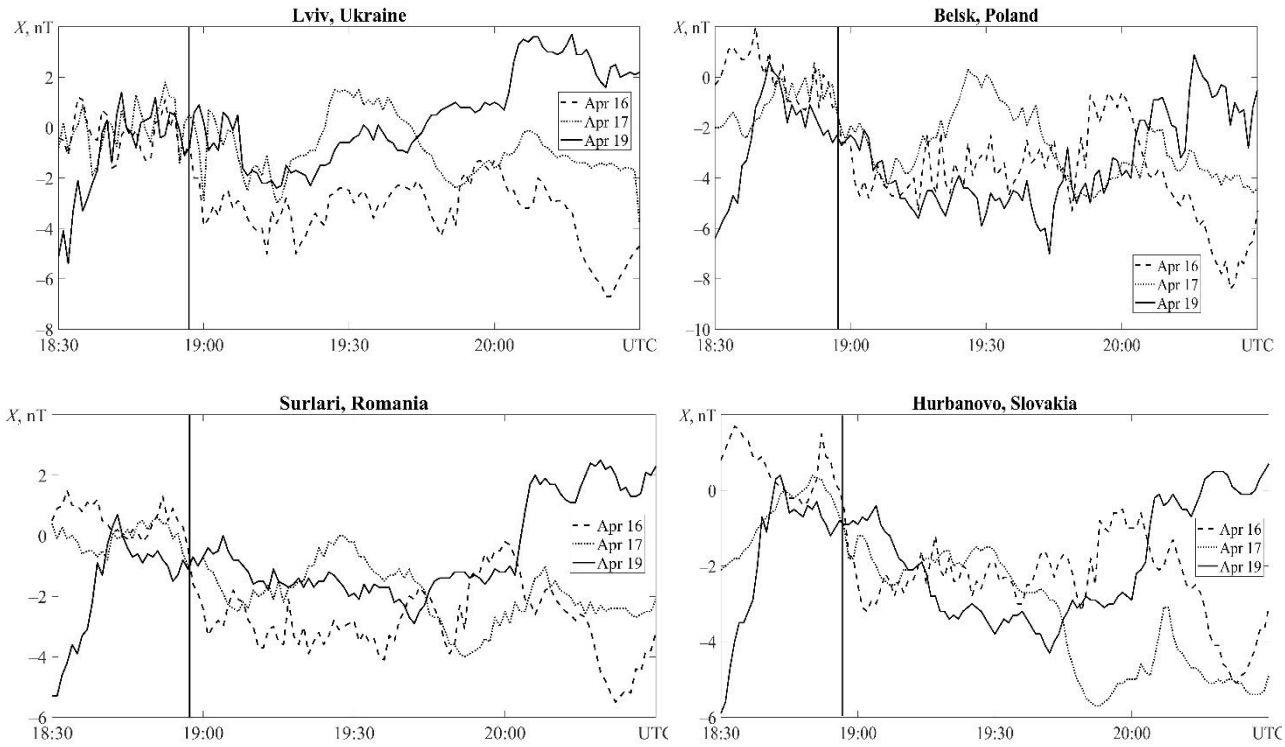

Fig. 1. Temporal variations of the level of the X-component of the geomagnetic field at the Lviv, Belsk, Surlari, and Gurbanovo on reference days and on the day of the meteoroid explosion. The vertical lines indicate of the time moment explosion of meteoroid

Work was supported by the National Research Foundation of Ukraine for financial support (project 2020.02/0015, “Theoretical and experimental studies of global perturbations of natural and man-made origin in the Earth–Atmosphere–Ionosphere system”). Work was also supported in part within the state budgetary research program of the Ministry of Education and Science of Ukraine (research projects #0121U109881, and #0122U001476).

References

[1] L. F. Chernogor, “Physical Effects from the Kyiv Meteoroid: Part 1,” Kinem. Phys. Celes. Bod., vol. 39, no. 5, pp. 261–279, 2023. https://doi.org/10.3103/S0884591323050045

[2] L. F. Chernogor, “Physical Effects from the Kyiv Meteoroid: Part 2,” Kinem. Phys. Celes. Bod., vol. 39, no. 6, 2023 (in press).

[3] L. F. Chernogor, “Physical Effects from the Kyiv Meteoroid: Part 3,” Kinem. Phys. Celes. Bod., vol. 40, no. 1, 2024 (in press).

[4] April 19 superbolide over Ukraine: https://www.imo.net/april-19-superbolide-over-ukraine/

[5] L. F. Chernogor, “Physical Effects of the Kyiv Meteoroid. International Conference,” Astronomy and Space Physics in the Kyiv University, May 23–26, book of Abstracts, pp. 98—99, 2023.

[6] L. F. Chernogor, O. I. Liashchuk, M. B. Shevelev, “Infrasonic effect of the Kyiv meteoroid,” International Conference «Astronomy and Space Physics in the Kyiv University», May 23–26, book of abstracts, pp. 115–116.

EFFECTS OF ROCKET LAUNCHES IN THE IONOSPHERE DURING GEOSPACE STORMS

L. F. Chernogor*, Y. H. Zhdanko*
**V. N. Karazin Kharkiv National University, Ukraine, 61022, Kharkiv, Svoboda Square, 4,*
e-mail: Leonid.F.Chernogor@gmail.com
**V. N. Karazin Kharkiv National University, Ukraine, 61022, Kharkiv, Svoboda Square, 4,*
e-mail: eugenezhd@gmail.com

The ionospheric response to the Soyuz and Proton rocket launches 2000 km away from the observation site during geospace storms, confirmed by the Doppler method, consisted of the generation of several groups of disturbances with a different horizontal apparent speeds.

Introduction

Ionospheric effects accompanying launches and flights of large rockets have been studied for about 60 years. The effects manifest themselves in all subsystems of the Earth–atmosphere–ionosphere–magnetosphere (EAIM) system and are highly diverse [1, 2]. The parameters of the effects significantly depend on the state of the Sun–interplanetary medium–magnetosphere–ionosphere–atmosphere–Earth (SIMMIAE) system, atmospheric and space weather, geographic coordinates of cosmodromes and observation means, type of rockets, their trajectory and type of fuel, etc. The scientific significance of studying the EAIM system reaction to rocket launches and flights lies in the fact that they contribute to a better understanding of the subsystems interaction in this system, the mechanisms of generation and transport of disturbances up to global distances. The practical significance of the research lies in the impact of disturbances from rocket launches and flights on the environment, the ecological situation in the EAIM system, the characteristics of radio waves of different ranges and, finally, on the performance characteristics of telecommunications, radio navigation, radio astronomy and remote radio sensing. The EAIM and SIMMIAE systems are often found to be disturbed. The strongest and most significant source of global disturbances are geospace storms [3]. Geospace storms significantly complicate the search for the ionospheric response to spacecraft launches. The aim of this study is to describe the results of long-term observations of the ionospheric processes that accompanied rocket launches and flights during geospace storms in the 2009–2021 period.

Space Weather State. Methods and Techniques

The state of space weather was described by the K_p, D_{st}, *F10.7* and *W* indices. K_p-index took values from 4– to 7–. Observational data on the ionospheric state prior to, during, and after the launch of the *Soyuz* and *Proton* rockets for 6–12 hours were used to analyze the measurements. The rockets were launched at different times of the day under significantly different geomagnetic activity, and therefore different ionospheric state. Observations were carried out at the Radiophysical Observatory of the V. N. Karazin Kharkiv National University. The Doppler radar for vertical sounding was used for measurements. The Doppler shift resolution is about 17 mHz. Frequencies of 3.2 and 4.2 MHz were used. The smaller one is effective in studying dynamic processes in the *E* and F_1 layers, and the larger one is effective in the F_1 and F_2 layers. The number of the *Soyuz* rocket launches is 81, and of the *Proton* rocket launches is 53. The application of the Fourier transform to the time variations of the beats of the received and reference signals over a time interval of 60 s made it possible to construct the time dependences of the Doppler spectra (DS) in the range from –1 Hz to +1 Hz. The delay time Δt of the possible ionospheric reaction to the rocket launch and flight was determined from the change in the nature of DS variations.

Discussion

Proton rocket launch on July 9, 2012. A very strong storm ($K_{p\max}$ = 7–) had a significant impact on the nature of the DS variations (Fig. 1*a*). All this made it difficult to identify the ionospheric reaction to the rocket launch. It is possible that this reaction was observed 14, 45 and 79 min after the event, which corresponded to apparent speeds of 4.4 km/s, as well as 1000 and 540 m/s. The speed was estimated according to the relation $v' = R/(\Delta t - \Delta t_0)$, where R is the distance between the disturbance generation region and the observation location, $\Delta t \approx 5$ min is the time during which the rocket reaches the disturbance generation region.

Soyuz rocket launch on December 15, 2015. The effects of a moderate storm ($K_{p\max}$ = 5–) superimposed on the effects characteristic of the ionosphere in December (Fig. 1*b*). Changes in the nature of the DS time variations were observed approximately 11, 62, 103 and 150 min after the rocket launch, which corresponded to apparent speeds of about 6.7 km/s, as well as 700, 410 and 275 m/s.

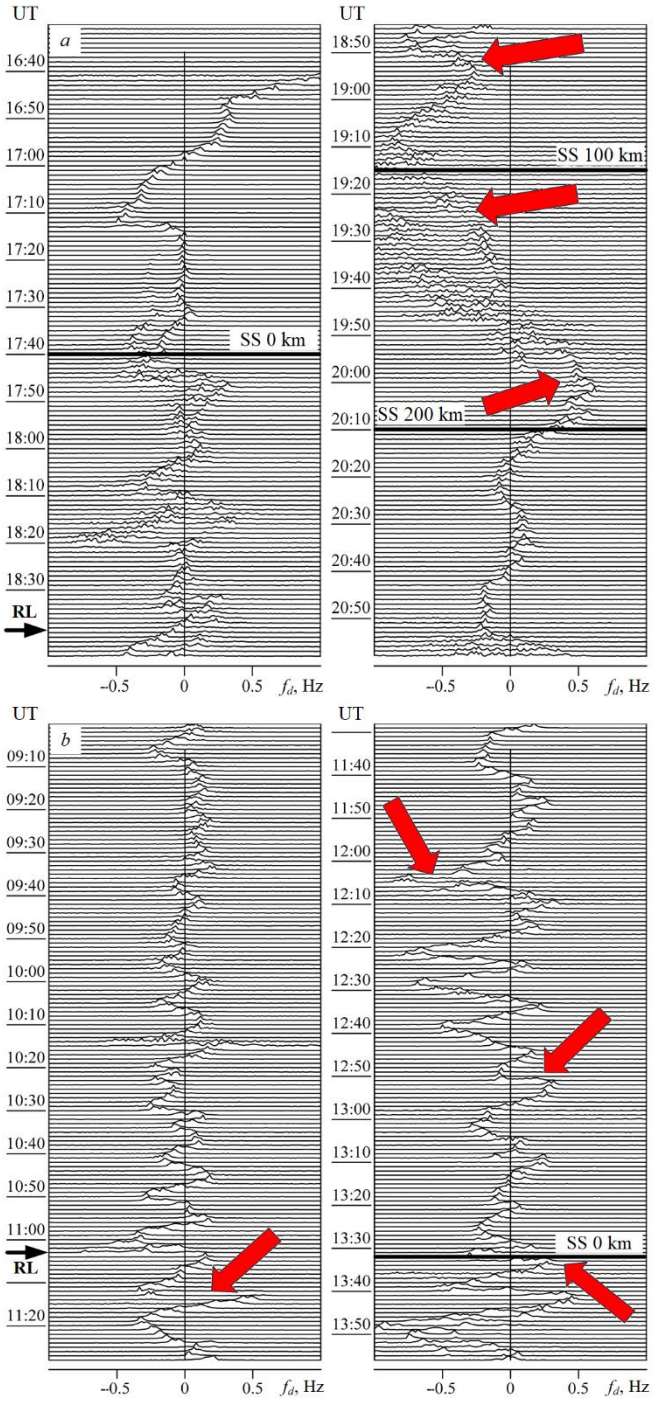

Fig. 1. (*a*) *Time variations of the DS at 3.2 MHz, followed the Proton rocket launch in the evening on July 9, 2012 and* (*b*) *at 4.2 MHz, followed the Soyuz rocket launch in the daytime on December 15, 2015.*

Main Results

Identification of the ionospheric response to the launch and flight of a large rocket 2000 km away from the observation site during the geospace storm by the Doppler method is usually possible at $K_{p\max} \leq 5$, and at its larger values is very complicated or even impossible. In a number of cases, even though $K_{p\max}$ = 4 the

determination of the ionospheric response is complicated. To increase the detection reliability of the response to the launch and flight of a rocket, the Doppler radar has to operate on a number of frequencies in the frequency range from 1.5–2 to 4–6 MHz. The existence of several groups of horizontal apparent speeds of disturbance propagation is confirmed: 1.7–3 km/s and more, 700–1000 m/s, 300–700 m/s, 150–260 m/s.

Work by L. F. Chernogor and Y. H. Zhdanko was supported by the National Research Foundation of Ukraine for financial support (project 2020.02/0015, «Theoretical and experimental studies of global perturbations of natural and man-made origin in the Earth–Atmosphere–Ionosphere system»).

References

[1] L. F. Chernogor, *Radiophysical and Geomagnetic Effects of Rocket Engine Burn: Monograph.* Kharkiv: V. N. Karazin Kharkiv National University Publ, 2009. (in Russian).

[2] L. F. Chernogor and N. Blaunstein, *Radiophysical and Geomagnetic Effects of Rocket Burn and Launch in the Near-the-Earth Environment*. Boca Raton, London, New York: CRC Press. Taylor & Francis Group, 2013.

[3] L. F. Chernogor and I. F. Domnin, *Physics of geospace storms*. Kharkiv: V. N. Karazin Kharkiv National University Publ, 2014. (in Russian).

MATHEMATICAL PROBLEMS OF APPLIED PHYSICS

MULTI-FRACTAL ANALYSIS IN PROBLEMS OF THE APPLIED PHYSICS

Leonid F. Chernogor*, Oleg V. Lazorenko, Andriy A. Onishchenko*****
** School of Radiophysics, Biomedical Electronics and Computer Systems, V. N. Karazin Kharkiv National University, Kharkiv 61022, Ukraine e-mail: Leonid. F. Chernogor@gmail.com*
*** School of Physics, V. N. Karazin Kharkiv National University, Kharkiv 61022, Ukraine, e-mail: Oleg.V.Lazorenko@karazin.ua*
**** Faculty of Automatics and Computerized Technologies, Kharkiv National University of Radioelectronics, Kharkiv 61166, Ukraine, email: Andrey.Onishchenko@nure.ua*

For the researchers, a review of the existing multi-fractal analysis methods applied in different branches of modern applied physics is proposed. For each multi-fractal analysis method, some actual references allowing to study the method and to develope corresponding numerical realization are given.

Introduction

According to the non-linear and the system paradigms, many processes generated in open, non-linear, dynamical systems under influence of a powerful source of energy release are appeared to be short-time, ultra-wideband, non-linear and fractal. In the paper [1] published one year ago, we have introduced a short review of the existing mono-fractal analysis methods, which can be useful and quitly applicable for solving of the applied physics problems, where there are a lot of such processes and such systems. To investigate their fractal properties more extended, the multi-fractal analysis methods should be applied. Unfortunately, similar the mono-fractal analysis methods, these methods are often appeared to be quite unknown for the most part of researchers too.

The purpose of this work is to present the multi-fractal analysis methods to the researchers. Due to volume limitations of this paper, the number of references for each method is strictly limited.

Multi-Fractal Analysis Methods

Multi-fractal analysis of the signals and processes is based on calculation of the set of numerical characteristics, namely the spectrum of generalyzed dimensions, which are known as the Renyi dimensions too, the scaling exponent, which is known as the mass index too, the multi-fractal spectrum function, which is known as the Hausdorf's multi-fractal spectrum, the singularities spectrum or the scaling spectrum too, and some other (see, for example, [2, 3]).

Now there are over ten multi-fractal analysis methods, which are regularly applied, in particular, in the applied physics (see, for example, [4]). Today there are the Wavelet Transform Modulus Maxima (WTMM) method [5 – 7], the Wavelet Coefficients method [8], the the Wavelet Leaders Method [8, 9], the multi-fractal detrended fluctuation analysis (MF DFA) [10], the generalyzed Hurst exponent method [11, 12], the multi-fractal regime detecting method [13], the weighted generalyzed Hurst exponent method [14], the local method of the second moment [15], the method based on the Cohen's class non-linear transforms [16, 17], the multi-fractal diffusion entropy analysis (MF DEA) [18], the Large deviation multifractal spectrum method [19], the Cumulative Mass Method, which is known as The "Sandbox" Method too [20], the the multi-fractal Detrended Moving Average (MFDMA) method [21] and other.

Besides methods listed above, there are the methods, which unite the multi-fractal and cross-correlations analyses [22], for example, Detrended Cross-Correlation Analysis (DCCA) та Multi-Fractal Detrended Cross-Correlation Analysis (MF-DXA). Most likely, it is already difficult to call them methods of multifractal analysis, but they allow to evaluate the cross-correlation of two signals using detrending and multifractal properties.

In the review paper [4], much more extended set of references and descriptions for the multifractal analysis methods listed above can be found.

References

[1] L. F. Chernogor, O. V. Lazorenko, A. A. Onishchenko, “Fractal Analysis in Problems of the Applied Physics”, Proc. XVIIIth APHYS, pp. 148 – 149, 2022.

[2] O. V. Lazorenko, L. F. Chernogor, “Fractal Radio Physics. 1. Theoretical Bases”, Radiophys. and Radioastron., vol. 25, no. 1, pp. 3 – 77, 2020.

[3] A. Onishchenko, L. Chernogor, O. Lazorenko, “Fractal and Multi-Fractal Analyses of the Geomagnetic Field Variations Caused by the Earthquake on January 24, 2020 in Turkey, J. of Nat. Sci. and Tech., vol. 1, no. 1, pp. 56 – 61, 2022.

[4] O. V. Lazorenko, L. F. Chernogor, “Fractal Radio Physics. 2. Fractal and Multifractal Analyses of Signals and Processes”, Radiophys. and Radioastron., vol. 28, no. 1, pp. 5 – 70, 2023.

[5] A. Arneodo, G. Grasseau and M. Holschneider, “Wavelet transform of multifractals”, Phys. Rev. Lett., vol. 61, pp. 2281 – 2284, 1988.

[6] S. Mallat, A Wavelet Tour of Signal Processing. San Diego, CA: Academic Press. 1998.

[7] J. F. Muzy, E. Bacry and A. Arneodo, “Multifractal formalism for fractal signals: The structure-function approach versus the wavelet-transform modulus-maxima method”, Phys. Rev. E, American Physical Society (APS), vol. 47, no. 2, pp. 875 – 884, 1993.

[8] B. Lashermes, S. Jaffard and P. Abry, “Wavelet Leader based Multifractal Analysis”, Proc. ICASSP ’05, 2005.

[9] S. Jaffard, B. Lashermes, and P. Abry, “Wavelet Leaders in Multifractal Analysis”, Appl. and Num. Harm. Anal., pp. 201 – 246, 2006.

[10] J. W. Kantelhardt, S. A. Zschiegner , E. Koscoelny-Bunde, S. Havlin, A. Bunde and H. E. Stanley, “Multifractal detrended fluctuation analysis of nonstationary time series”, Phys, A: Stat. Mech. and Its App,, vol. 316, no. 1 – 4, pp. 87 – 114, 2002.

[11] A.-L. Barabási, and T. Vicsek, “Multifractality of self-affine fractals”, *Phys. Rev. A,* vol. 44, no. 4, pp. 2730 – 2733, 1991.

[12] T. Di Matteo, T. Aste, and M. Dacorogna, “Scaling behaviors in differently developed markets”, Phys, A: Stat. Mech. and its App., vol. 324, no. 1, pp. 183 – 188, 2003.

[13] H. Lee, and W. Chang, “Multifractal regime detecting method for financial time series”, Chaos, Solitons & Fractals, vol. 70, pp. 117 – 129, 2015.

[14] R. Morales, T. Di Matteo, R. Gramatica, and T. Aste, “Dynamical generalized Hurst exponent as a tool to monitor unstable periods in financial time series”, Phys. A Stat. Mech. Appl., vol. 391, pp. 3180 – 3189, 2012.

[15] H. M. Hastings, and G. Sugihara, Fractals: A User’s Guide for the Natural Science. Oxford: Oxford University Press, 1993.

[16] P. Flandrin, ed., Time-Frequency/Time-Scale Analysis. San Diego: Academic Press, 1999.

[17] J. J. Benedetto, J. S. Byrnes, J. L.Byrnes, K. A. Hargreaves, and K. Berry, Wavelets and Their Applications. Springer Scince+Business Media, B.V., 1994.

[18] J. Huang, P. Shang, and X. Zhao, “Multifractal diffusion entropy analysis on stock volatility in financial markets”, Phys. A: Stat. Mech. and Its App., vol. 391, no. 22, pp. 5739 – 5745, 2012.

[19] M. Broniatowski, and P. Mignot, “A self-adaptive technique for the estimation of the multifractal spectrum”, Stat. & Probab. Lett., vol. 54, no. 2, pp. 125 – 135, 2001.

[20] T. Vicsek, “Mass multifractals”, Phys. A: Stat. Mech. and Its App., vol. 168, no. 1, pp. 490 – 497, 1990.

[21] G.-F. Gu, and W.-X.Zhou, “Detrending moving average algorithm for multifractals“, Phy. Rev, E, vol. 82, no. 1, 2010.

[22] D. Ghosh, S. Dutta, and S. Chakraborty, “Multifractal detrended cross-correlation analysis for epileptic patient in seizure and seizure free status”, Chaos, Solitons & Fractals, vol. 67, pp. 1 – 10, 2014.

STUDY OF ORIENTATIONAL MOTION OF PROTONS ALONG THE C-AXES IN HEXAGONAL CRYSTALS USING QUADRATIC APPROXIMATION

M.V. Maksyuta, V.I. Vysotskii, D.M. Maksyuta, S.V. Efimenko
Faculty of Radio Physics, Electronics and Computer Systems Taras Shevchenko Kyiv National University of Kyiv, Glushkova ave., 4g, e-mail: maksyuta.nik@gmail.com

The paper calculates the potentials of interaction between positively charged particles and the c-axes in crystals with a hexagonal structure (specifically, in crystals of Be, Sc, Ti, Co, Zn, Y, Zr, Tc, Ru, Cd and La). The analysis was conducted using the approximation potentials Moliere, Firsov and Barrett. For protons with various Lorentz-factors, energy levels and their corresponding wave functions are computed by solving the Schrödinger equation in a cylindrical coordinate system using a quadratic approximation. Based on this data, radial distribution profiles are calculated for non-dispersive beams of protons moving at zero angles to the c-axes in hexagonal channels, as well as spectral distributions of spontaneous radiation.

Using the approximation potentials of Moliere and Firsov (see, for example, [1]), as well as the Barrett potential (see [2]) the potentials of interaction, denoted as $U(\xi,\eta)$ between protons and the c-axes were computed in hexagonal crystals of Be, Sc, Ti, Co, Zn, Y, Zr, Tc, Ru, Cd and La in relative units $\xi = x/a$, $\eta = y/a$ (parameters *a* are given in [3]). It's worth noting that the calculation using the Molière approximation have previously been carried out in [4]. 2D-interaction potentials in the ξ- and η-directions (see Fig. 1a) are presented in Fig. 1b, c, d for instance, for the case of the Zn crystal.

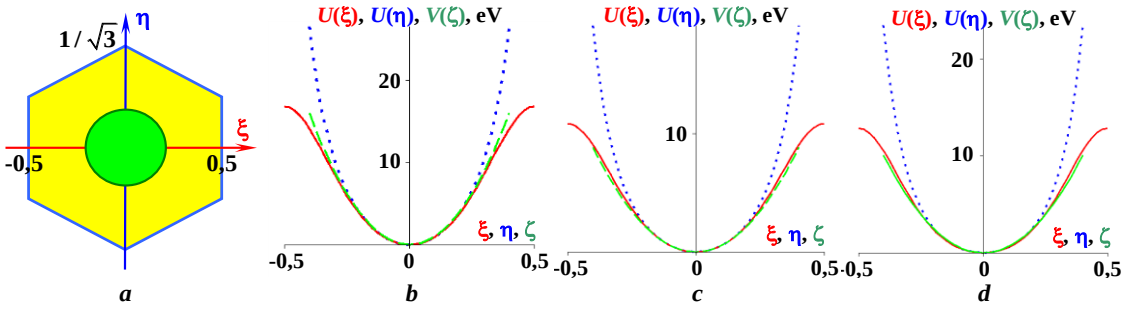

Fig. 1. (a) – schematic representation of hexagonal channel and the circular region where the quadratic approximation is applied; 2D-interaction potentials between a proton and the c-axes in Zn crystal along the ξ-directions (solid curves) and η-directions (dotted curves), computed using the Moliere approximations – (b), Firsov – (c), Barrett – (d)

The results presented in Figure 1b, c, d indicate that the choice of approximation for the single-particle potential of crystal atom significantly affects the depth of the potential well. Obviously, these differences will substantially influence other characteristics of the orientational motion of protons, namely, the radial distribution of the proton wave function in the channel, the spectra of spontaneous emission, etc.

The results of the calculations have shown that for all the investigated hexagonal crystals and for all approximations within the circular regions with relative radii $\zeta_0 = \rho_0/a \approx 0,2$, the interaction potentials $U(\xi,\eta)$, as seen from Fig. 1b, c, d are described quite accurately by quadratic functions $V(\zeta) = V_0\zeta^2$ (dashed curves). The values of the parameters V_0 (in eV) are given in Table 1 in the numerators of the fractions. Additionally, Table 1 presents the minimum values of the Lorentz-factors γ_{min} (see the denominators of fractions) of channeled protons, for which the function $V(\zeta)$ can be used. It is worth noting that similar calculations were conducted in a previous work [5], which investigated the orientational motion of positrons in non-chiral nanotubes.

Table 1. *Values of the approximation parameters V0 in the hexagonal crystals under study for the Moliere, Firsov and Barrett approximations, as well as the values of γmin*

Crystal		Be	Sc	Ti	Co	Zn	Y	Zr	Tc	Ru	Cd	La
$\frac{V_0}{\gamma_{min}}$	M	38/44	52/18	75/11	123/9	100/12	47/11	70/8	116/8	125/9	45/27	40/19
	F	30/56	28/25	43/14	73/20	55/28	28/27	40/21	67/28	80/23	25/30	30/23
	B	42/55	28/40	43/34	80/23	63/17	13/74	24/47	58/19	61/26	7/150	8/120

Further investigations were conducted taking into account the solution of the Schrödinger equation in potential $V(\zeta)$ (see [6]). Using these solutions, as well as the numerical values from the table. 1, radial distributions, as well as spectral distributions of spontaneous emission, were determined (in relative units). Fig. 2 illustrates these distributions using the example of a Zn crystal.

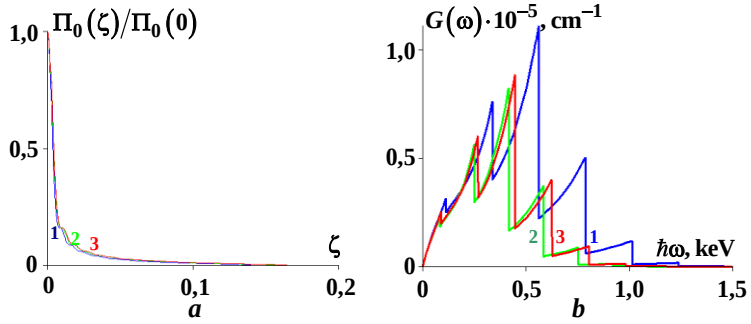

Fig. 2. Distributions using the Moliere (curves 1), Firsov (curves 2), Barrett (curves 3) approximations for a non-dispersive proton beam with a Lorentz factor γ = 30, moving in a Zn crystal at a zero angle to the c-axes: (*a*) – radial, (*b*) – spectral

As seen from Fig. 2a, the radial distributions of protons are insensitive to the choice of approximation. However, for the spectral distributions (see Fig. 2b), there is a difference that can be experimentally verified.

References

[1] V.A. Bazylev, N.K. Zhevago. Fast particles radiation in a substance and in external fields. Moscow: Nauka, 1987 (in Russian).

[2] J.H. Barrett // Phys. Rev B., 1979, Vol. 20, No. 9, pp. 3535 – 3542.

[3] N. Ashcroft, N. Mermin. Solid State Physics. New York: Saunders College Publishing, 1976.

[4] N.V. Maksyuta, V.I. Vysotskii, S.V. Efimenko, D.N. Maksyuta / *Book of proceedings of The 18th Int. Conf. on Electronics and applied physics, Taras Shevchenko National University of Kyiv, Faculty of RadioPhysics, Electronics and Computer Systems*, October 18 – 22, 2022, Kyiv (Ukraine), pp. 152 – 153.

[5] M.V. Maksyuta, V.I. Vysotskii, D.M. Maksyuta, S.V. Efimenko / *Book of Abstracts XIV Int. Symp. RREPS – 23 & VIII Int. Conf. Meghri – 23*, Septembe 18 – 22, 2023, Tsaghkadzor (Armenia), pp. 58 – 59.

[6] S. Flügge. Practical Quantum Mechanics. Springer – Verlag Berlin, 1999.

CONTENTS OF THE CONFERENCE

INTRODUCTION 2
PREFACE 4

INVITED LECTURES

1 **INTRODUCTION TO BASICS OF INTELLECTUAL PROPERTY: WHAT ONE NEEDS TO KNOW WHILE WORKING IN HIGH TECH?**

A. Veligura 6
Head of IP for Monitoring and Enterprise Informatics, Philips IP&S, Eindhoven, The Netherland

2 **NONLINEAR DYNAMICS OF SKYRMION STRINGS**

V. Kravchuk 7
Leibniz-Institut für Festkörper- und Werkstoffforschung, IFW Dresden, 01171 Dresden, Germany
e-mail: v.kravchuk@ifw-dresden.de

3 **HIGH-PERFORMANCE OF LIQUID-GATED SILICON NANOWIRE FIELD-EFFECT TRANSISTORS COVERED WITH ULTRATHIN LAYERS OF DIAMOND LIKE TETRAHEDRAL AMORPHOUS CARBON** 7

Nazarii Boichuk
Bioelectronics (IBI-3), Forschungszentrum Jülich, Germany

1. LASER PHYSICS AND OPTOELECTRONICS (LPO)

1. **NON-DESTRUCTIVE TESTING OF MAO ALUMINA COATINGS USING SUB-THZ ELLIPSOMETRY**

Galuza A.A.*, Kolenov I.V., Vinnikov D.V.***, Mizrakhy S.V.******** 9
National Technical University "Kharkiv Polytechnic Institute", 2 Kyrpychova St., Kharkiv 61002, Ukraine,
e-mail: alexey.galuza@gmail.com
***Institute of Electrophysics and Radiation Technologies of the NAS of Ukraine, P.B. 8812, 28 Chernyshevsky St., Kharkiv 61002, Ukraine,*
O.Ya. Usikov Institute for Radiophysics and Electronics of the NAS of Ukraine, 12, Ac. Proskura St., Kharkiv 61085, Ukraine
e-mail: ivan.kolenov@gmail.com
****National Science Center Kharkiv Institute of Physics and Technology, Kharkiv, Ukraine, email: vinniden@gmail.com*
*****O.Ya. Usikov Institute for Radiophysics and Electronics of the NAS of Ukraine, 12, Ac. Proskura St., Kharkiv 61085, Ukraine*
emial: smizrakhy@hotmail.com

2. **FEATURES OF FOCUSING COMBINED MODES OF DIELECTRIC WAVEGUIDE RESONATOR**

Degtyarev Andrey*, Dubinin Mykola*, Maslov Vyacheslav*, Muntean Konstantin*, Svystunov Oleg* 11
**V.N. Karazin Kharkiv National University,*

e-mail: mykola.dubunin@karazin.ua

3. **PACKET QUANTIZATION OF THR ELECTROMAGNETIC FIELD**

Ovechko V*. 14
e-mail: ovs@univ.kiev.ua
** Taras Shevchenko National University of Kyiv, Kyiv 01601, Ukraine,*

2. PHYSICS OF MAGNETISM (PM)

1. **ENHANCED LONGITUDINAL RELAXATION OF SOLITONS IN ULTRATHIN MAGNETIC FILMS**

Ivan A. Yastremsky[1,2], Boris A. Ivanov[3], Denys Makarov[2]

[1]Taras Shevchenko National University of Kiev, 03127 Kiev, Ukraine 17

2Helmholtz-Zentrum Dresden-Rossendorf e.V., Institute of Ion Beam Physics and Materials Research, Bautzner Landstrasse 400, 01328 Dresden, Germany

[3]Institute of Magnetism, National Academy of Sciences and Ministry of Education and Science, 03142 Kyiv, Ukraine

2. **OPTICAL TUNING OF THE MAGNETIC MODE FREQUENCIES IN Si:YIG**

M. O. Popov*, H. L. Chumak*
** Educational and Scientific Institute of High Technologies, Taras Shevchenko National University of Kyiv, Kyiv 01601, Ukraine,* 19
e-mail: maxim_popov@univ.kiev.ua chumak_hryhorii@univ.kiev.ua

3. **ULTRAFAST PROPAGATION OF NONLINEAR SPIN WAVE THROUGH AN ANTIFERROMAGNETIC MAGNONIC CRYSTAL**

***Gorobets, O.Yu., *Kulish, V.V., *Syzon, I.A., *Provolovska, D.V.** 21
**National Technical University of Ukraine «Igor Sikorsky Kyiv Polytechnic Institute», 37 Beresteisky Ave., 03056 Kyiv, Ukraine,*
e-mail: provolovska.daryna@lll.kpi.ua

4. **THE EFFECT OF MAGNETIC FIELD ON RESIDUAL STRESS RELAXATION IN EP-718 ALLOY**

Seidametov S.V., Pavlenko D.V., Schetinina M.O., Loskutov S.V., Pravda M.I. 22
National University Zaporizhzhia Polytechnic, 64 Zhukovskogo str., Zaporizhzhia, 69063, Ukraine, e-mail: stanislav.seidametov@gmail.com

3. SURFACE PHYSICS, NANO- AND MICROELECTRONICS (SP)

1. **INFLUENCE OF AHARONOV-BOHM EFFECT ON HYDRODYNAMIC INSTABILITY OF A TUBULAR ELECTRON BEAM MOVING ALONG SEMICONDUCTOR NANOTUBE WITH DIELECTRIC FILLING**

Yu. O. Averkov*, Yu. V. Prokopenko, V. M. Yakovenko***, V. A. Yampol'skii****** 25
** O. Ya. Usikov Institute for Radiophysics and Electronics of the National Academy of Sciences of Ukraine, Kharkiv 61085, Ukraine; Faculty of Computer Science of V. N. Karazin Kharkiv National University, Kharkiv 61077, Ukraine, e-mail: yuriyaverkov@gmail.com*

*** O. Ya. Usikov Institute for Radiophysics and Electronics of the National Academy of Sciences of Ukraine, Kharkiv 61085, Ukraine, e-mail: yurii.prokopenko@nure.ua*
**** O. Ya. Usikov Institute for Radiophysics and Electronics of the National Academy of Sciences of Ukraine, Kharkiv 61085, Ukraine*
***** O. Ya. Usikov Institute for Radiophysics and Electronics of the National Academy of Sciences of Ukraine, Kharkiv 61085, Ukraine; Faculty of Theoretical Physics of V. N. Karazin Kharkiv National University, Kharkiv 61077, Ukraine, e-mail: val.yampolskii@gmail.com*

2. **SELF-ASSEMBLY OF LONG RANGE ORDERED ANISOTROPIC SPATIALLY PERIODIC ADSORBATE STRUCTURES ON Mo(112) – A REVIEW**

A. G. Fedorus*, A. M. Goriachko, A. G. Naumovets***, D. V. Rumiantsev***
**Department of Physical Electronics, Institute of Physics, The National Academy of Sciences of Ukraine,*
Prospect Nauky, 46, Kyiv 03028, Ukraine, e-mail: fedorus.gm@gmail.com
***Faculty of RadioPhysics, Electronics and Computer Systems, Taras Shevchenko National University of Kyiv, Volodymyrska Str. 64/13, Kyiv 03127, Ukraine, email: goriachko@knu.ua*
****Presidium of the National Academy of Sciences of Ukraine, Volodymyrska, 54, Kyiv 01030, Ukraine,*
email: naumovets@nas.gov.ua
27

3. **SCANNING TUNNELING MICROSCOPY / SPECTROSCOPY OF METALLIC NANOCLUSTERS DEPOSITED ON THE GERMANIUM (111) SURFACE**

Andrii Goriachko*
**Faculty of RadioPhysics, Electronics and Computer Systems, Taras Shevchenko National University of Kyiv, Volodymyrska Str. 64/13, Kyiv 03127, Ukraine, email: goriachko@knu.ua*
29

4. **STUDY OF THE OXYGEN INTERACTION WITH (001) SILICON SURFACE COVERED WITH PREADSORBED METALS MONOLAYERS**

Yaroslav Kulikovskyi*, Yurii Len**
Faculty of Radio Physics, Electronics and Computer Systems, Taras Shevchenko National University of Kyiv, 64/13, Volodymyrska Str., Kyiv, Ukraine, 01601
**kylikyar23@gmail.com, **lenyurii21@gmail.com*
31

4. PHYSICS OF SEMICONDUCTORS AND DIELECTRICS, SEMICONDUCTOR DEVICES (PS)

1. **MICROWAVE PROPERTIES OF COMPOSITE MATERIALS BASED ON POLYVINYL CHLORIDE AND OXIDATED ACTIVATED CARBON IN THE MICROWAVE BAND**

D.O. Zhytnyk*, V.A. Moiseienko, Yu.V. Noskov***, I.P. Matushko*, O.V. Mischanchuk******, L.M. Grishchenko***
**Taras Shevchenko National University of Kyiv, Kyiv 01601, Ukraine, e-mail: radiodima2000@gmail.com*
***Independent Research & Development Laboratory "200k Electronics", Kyiv, Ukraine, e-mail: vamrpd@gmail.com*
****Kukhar institute of bioorganic chemistry and petrochemistry NAS of Ukraine, Kyiv 02000, Ukraine, e-mail: yuriy.noskov@gmail.com*
34

****O.O. Chuiko Institute of Surface Chemistry of NAS of Ukraine, Kyiv 03164, Ukraine, e-mail: bigsnake@i.ua

2. **ANALYTICAL MODEL FOR A SUBTHRESHOLD SWING IN A MOSFET WITH A SOURCE BASED ON COLD METAL**

K.O.Korzh* , M.V.Strikha**
*Taras Shevchenko National University of Kyiv
Volodymyrska Str. 64/13, 01601 Kyiv – Ukraine, e-mail: korzh.katia14@gmail.com
**Taras Shevchenko National University of Kyiv
Volodymyrska Str. 64/13, 01601 Kyiv – Ukraine, e-mail: maksym.strikha@gmail.com* 37

3. **ADHESIVE PROPERTIES OF THE BROKEN SURFACE LAYER OF PZT PIEZOCERAMICS**

S.P. Lushchin
National University Zaporizhzhia Polytechnic, 64, Zhukovskogo Street, Zaporizhzhye 69063, Ukraine, e-mail: luschin@zntu.edu.ua 39

4. **MICROWAVE PROPERTIES OF COMPOSITE MATERIALS BASED ON POLYURETHANE AND CARBON NANOMATERIALS**

D.O. Zhytnyk*, V.V. Trachevskiy, V.A. Moiseienko***, A.N. Zaderko*, L.M. Grishchenko***
* Taras Shevchenko National University of Kyiv, Kyiv 01601, Ukraine, e-mail: radiodima2000@gmail.com
** National Academy of Sciences of Ukraine Institute of Macromolecular Chemistry, 48, Kharkivske Shosse, Kyiv, 02155, Ukraine, e-mail: meches49@ukr.net
*** Independent Research & Development Laboratory "200k Electronics", Kyiv, Ukraine, e-mail:vamrpd@gmail.com* 41

5. **GAS SENSOR BASED ON THE SPECTRAL SURFACE PLASMON RESONANCE EFFECT WITH COLORIMETRIC REGISTRATION**

O. Riabcenko, O Kukla, A. Biletskiy

V.E. Lashkaryov Institute of Semiconductor Physics of the National Academy of Sciences of Ukraine 43

5. MEDICAL PHYSICS (MP)

1. **MODIFIED NANOSTRUCTURED TITANIUM OXIDE ELECTRODES FOR DNA HYBRIDIZATION SENSOR**

Schurenko A.I.[1], Khomich V.A.[1], Dobrovolskiy A.M.[1], Mamykin A.V.[2], Doroshenko T.P.[2], Kukla O.L. [2], Grynko D.O.[2,3]
[1] *Institute of Physics, National Academy of Sciences of Ukraine, 46, Nauki Av., Kyiv 03028, Ukraine*
[2] *V.Ye. Lashkaryov Institute of Semiconductor Physics, National Academy of Sciences of Ukraine, 41, Nauki Av., Kyiv 03028, Ukraine*
[3] *Institute of Molecular Biology and Genetics, National Academy of Sciences of Ukraine, 150, Zabolotnogo Str., Kyiv 03143, Ukraine; e-mail: dgrynko@gmail.com* 46

2. **HARNESSING PHYSICALLY-INFORMED NEURAL NETWORKS FOR NOISE REDUCTION** 47

Sliusarenko D. G.*, Netreba A. V.**
**Faculty of RadioPhysics, Electronics and Computer Systems Taras Shevchenko National University of Kyiv, Kyiv 01601, Ukraine, email: d.fulhem@gmail.com*
***Faculty of RadioPhysics, Electronics and Computer Systems Taras Shevchenko National University of Kyiv, Kyiv 01601, Ukraine, email: avn@univ.kiev.ua*

3. **LASER PULSE RADIUS EFFECT ON GENERATION OF RAMAN SCATTERING IN SELF-FOCUSING LIQUID**

Oleksandr Mokhonko*, Anatoliy Ivanisik**
**Taras Shevchenko National University of Kyiv, e-mail: sashamohonko@gmail.com*
***Taras Shevchenko National University of Kyiv, e-mail: anatoliyivanisik@gmail.com* 49

4. **BUILDING A SYSTEM FOR RECORDING AND PROCESSING ELECTROENCEPHALOGRAPHIC DATA IN REAL TIME**

Roman Piven*, Oleksandr Sudakov**
**Faculty of RadioPhysics, Electronics and Computer Systems Taras Shevchenko National University of Kyiv, Kyiv 01601, Ukraine, email romapivev@knu.ua* 51

***Faculty of RadioPhysics, Electronics and Computer Systems Taras Shevchenko National University of Kyiv, Kyiv 01601, Ukraine, email* saa@knu.ua

5. **RESEARCH OF LOW TEMPERATURE REDUCED PRESSURE PLASMA FOR AGRICULTURAL PURPOSES**

U. Palianytsia, Yu. Veremii, V. Cherniak, V. Yukhymenko
Faculty of RadioPhysics, Electronics and Computer Systems Taras Shevchenko National University of Kyiv, Kyiv 01601, Ukraine, e-mail: yu.veremii@knu.ua 53

6. PLASMA PHYSICS (PP)

1. **THE INFLUENCE OF SINTERING TEMPERATURE ON THE EROSION RESISTANCE OF Cu-W COMPOSITE MATERIALS**

A. Murmantsev[1], A. Veklich[1], V. Boretskij[1]
[1]Taras Shevchenko National University of Kyiv, 63/13, Volodymyrska str., Kyiv 01601, Ukraine
**murmantsev.aleksandr@gmail.com* 56

2. **EFFECT OF AN GENERATED PUMP ELECTRIC FIELD ON A GROWTH INCREMENT OF THE INPUT SIGNAL IN THE PARAMETRIC SUPERHETERODYNE FREE ELECTRON LASER IN QUADRATIC NONLINEAR APPROXIMATION**

Stanislav Ilin, Alexander Lysenko
Faculty of Electronics and Information Technology Sumy State University, Sumy 40007, Ukraine, e-mail: sequell3@gmail.com 59

3. **GROWTH AND DIFFUSION OF CLUSTERS IN THE CYLINDRICAL MAGNETRON CHAMBER**

O.Yu.Abakumenko, O.A. Demeshko, O.Yu. Kravchenko
Taras Shevchenko Kyiv University, Volodymirs'ka Str. 64, 01601, Kyiv, Ukraine, kay@univ.kiev.ua 61

4. **FORMATION OF THE CHANNEL IN A DENSE PLASMA BARRIER VIA THE BEAM OF STRONG ELECTROMAGNETIC WAVES**

B.R. Mykhailenko, I.O. Anisimov 63
Taras Shevchenko National University of Kyiv, Faculty of Radio Physics, Electronics and Computer Systems
E-mail: mihaylenko.bogdan12@gmail.com

5. **INVESTIGATION OF PLASMA GENERATION UNIFORMITY IN A DISCHARGE WITH A HOLLOW CATHODE**

A.V. Ryabtsev*, V.O. Khomych** 65
** Institute of Physics of NAS of Ukraine, Kyiv, Ukraine, e-mail: ryabtsev@iop.kiev.ua*
*** Institute of Physics of NAS of Ukraine, Kyiv, Ukraine, e-mail: khomich@iop.kiev.ua*

6. **ORGANOMETALLIC COMPOUNDS DISPROPORTIONATION REACTIONS IN A PLASMA-LIQUID SYSTEM WITH A ROTATING GLIDING AND SECONDARY DISCHARGE**

V.Ya. Chernyak[1], V.V. Iukhymenko[1], K.V. Iukhymenko[1], S.V. Shulga[2], D.D. Tretiakov[1], O.M. Tsymbaliuk[1], S.S. Nedovesov[1], N.V. Matlakh[1] 67
Taras *Shevchenko National University of Kyiv, Faculty of RECS [2]Institute of Hydromechanics NAS of Ukraine*
E-mail: chernyak_v@ukr.net, yvitaliy@ukr.net, sergey.v.shulga@gmail.com

7. **PLASMA STREAMS GENERATED BY MAGNETOPLASMA COMPRESSOR WITH AXIAL MAGNETIC FIELD**

Y.E. Volkova[1,2], D.G. Solyakov[1], I.E. Garkusha[1,2], A.K. Marchenko[1], M.S. Ladygina[1], V.V. Staltsov[1],
Yu.V. Petrov[1], V.V. Chebotarev[1], T.M. Merenkova[1], V.A. Makhlai[1,2], D.V. Yeliseyev[1] 69
[1]Institute of Plasma Physics NSC "Kharkiv Institute of Physics and Technology", Akademichna St., 1,
Kharkiv, Ukraine, e-mail: solyakov@ipp.kharkov.ua
[2]V.N. Karazin Kharkiv National University, Svobody Square, 4, Kharkiv, Ukraine,
e-mail: y.e.volkova.kh@gmail.com

8. **CHARACTERISTICS OF PLASMA SYSTEMS WITH ROTARY GLIDING DISCHARGE**

V.Ya. Chernyak*, S.S. Nedovesov*, V.V. Iukhymenko*, O.M. Tsymbaliuk*, S.V. Shulga, K.V. Iukhymenko*, D.D. Tretiakov***
** Faculty of RadioPhysics, Electronics and Computer Systems Taras Shevchenko National University of Kyiv, Kyiv 01601, Ukraine, e-mail: chernyak_v@ukr.net* 71
*** Institute of Hydromechanics NAS of Ukraine, Kyiv, Ukraine, email: sergey.v.shulga@gmail.com*

9. **DIFFERENTIAL EQUATION WITH NON-HOMOGENEOUS COEFFICIENTS FOR THE LONG-TERM COMPLEX AMPLITUDE OF THE ELECTRIC FIELD IN A PLASMA**

73

V.M. Lashkin*, N.A.Beloshenko**
**Kyiv Institute for Nuclear Research, Kyiv Nauki avenue 47, Ukraine, e-mail: vlashkin62@gmail.com*

** *Kyiv Institute for Nuclear Research, Kyiv Nauki avenue 47, Ukraine, e-mail: Beloshenko@gmail.com*

7. COMPUTER TECHNOLOGIES (CT)

1. **IMPROVING IOT WITH BLOCKCHAIN: CONSENSUS AND ENERGY EFFICIENCY**

Leonid Chepel*, Yuriy Boyko**
Faculty of RadioPhysics, Electronics and Computer Systems Taras Shevchenko National University of Kyiv, Kyiv 01601, Ukraine 76

8. RADIO ENGINEERING AND COMMUNICATIONS (REC)

1. **CLASIFICATION OF COMBUSTION PRODUCTS FROM TREE LEAVES ELECTRONIC CIGARETTES IN OUTDOOR CONDITIONS**

A. Antonenko, V. Boretskij, O. Zagaria 79
Taras Shevchenko National University of Kyiv, 64/13, Volodymyrska Street, Kyiv, Ukraine
e-mail: andreww131998@gmail.com

2. **USING OF VARIOUS FREQUENCY BANDS OF EARTH SATELLITES RADIO EMISSION FOR DIAGNOSE THE DEGREE OF SEA WAVES**

Yu. A. Pedenko*, V. B. Synytsky, V. B. Zamarajev*****
**O. Ya. Usikov Institute for Radiophysics and Electronics of the National Academy of Sciences of Ukraine, Kharkiv 61085, Ukraine, e-mail: yuriy.pedenko@gmail.com* 81
*** O. Ya. Usikov Institute for Radiophysics and Electronics of the National Academy of Sciences of Ukraine, Kharkiv 61085, Ukraine, e-mail: vladimir.b.sinitskiy@gmail.com*
****O. Ya. Usikov Institute for Radiophysics and Electronics of the National Academy of Sciences of Ukraine,Kharkiv 61085, Ukraine, e-mail: zvb73zvb73@gmail.com*

3. **DETECTION AND RESTORATION OF DIGITAL INFORMATION SIGNAL FROM AMPLITUDE SHIFT KEYING (ASK) RADIO SIGNAL WITH STOCHASTIC NOISE-LIKE CARRIER**

Bohdanov R.V.
Faculty of Radio Physics, Electronics and Computer Systems, Taras Shevchenko National University of Kyiv, 83
64/13, Volodymirska Str., City of Kyiv, Ukraine, 01601,
e-mail: roman.bohdanov@knu.ua

4. **REVIEW PEPPER: USAGE OF UNMANNED AERIAL VEHICLES IN 5G NETWORKS**

Danuk D. A.*, Al Sharify Mushtaq Talib**
** e-mail: mahavstt@gmail.com*
*** e-mail: mushtaq.talib2005@gmail.com* 85
****Faculty of RadioPhysics, Electronics and Computer Systems Taras Shevchenko National University of Kyiv, Kyiv 01601, Ukraine*

5. **LARGE-SCALE GEOMAGNETIC FIELD DISTURBANCES CAUSED BY THE STRONG EXPLOSION OF THE TONGA VOLCANO ON JANUARY 15, 2022**

L. F. Chernogor*, M. Yu. Holub*
**V. N. Karazin Kharkiv National University, Ukraine, 61022, Kharkiv, Svoboda Square, 4, e-mail: Leonid.F.Chernogor@gmail.com*
**V. N. Karazin Kharkiv National University, Ukraine, 61022, Kharkiv, Svoboda Square, 4, e-mail: marya160588@gmail.com* 87

6. **SYSTEM ADVANTAGES AND FEATURES OF THE USE OF STOCHASTIC PERIODIC COMPLEX PULSE RADIO SIGNALS IN THE SENSING MODES OF A SURVEILLANCE RADAR**

V. Kantsedal, A. Mogyla
Dept. of physical principles of radiolocation O.Ya.Usikov Institute for Radiophysics and Electronics of the National Academy of Sciences of Ukraine, Kharkiv 61085, Ukraine, e-mail: vkantsedal9@gmail.com, Moganat1196@gmail.com 89

7. **RATIONALE FOR CONSTRUCTION OF THE STRUCTURE OF THE SYSTEM FOR COGNITIVE CONTROL OF TYPES OF SIGNAL RESOURCE SURVEILLANCE RADAR**

V. Kantsedal
Dept. of physical principles of radiolocation O.Ya.Usikov Institute for Radiophysics and Electronics of the National Academy of Sciences of Ukraine, Kharkiv 61085, Ukraine, e-mail: vkantsedal9@gmail.com 91

8. **WEAK SIGNAL MODEL AND ITS APPLICABILITY TO THE ANALYSIS OF DISTRIBUTED FIBER OPTIC AMPLIFIER IN TELECOMMUNICATION SYSTEMS**

Kononenko A. A. [*], Zhirov G.B. [*], Reznikov M.I. [**], Felinskyi G.S. [**].
Taras Shevchenko National University of Kyiv, Kyiv, Ukraine,
[*] Faculty of Radio Physics, Electronics and Computer Systems e-mail: kononenkoartem267@gmail.com, genna-g@ukr.net
[**] Educational and Scientific Institute of High Technologies e-mail: mirez@ukr.net, felinskyi.gs@gmail.com 93

9. **DICOM VIEWER FOR WEB IMPLEMENTATION OF TELEMEDICINE APPLICATIONS**

M. Kononov *, V. Kononov **
Taras Shevchenko National University of Kyiv, Volodymyrska str.,64/13,
** e-mail: m_v_k@univ.kiev.ua*
*** e-mail: viktor1998kononov@gmail.com* 95

10. **THE COMPACT POLARIZATION SEPARATOR FOR WEATHER RADAR**

V. Glamazdin, M. Natarov, O. Shubnyi, A. Mogyla
Dept. of physical principles of radiolocation O.Ya.Usikov Institute for Radiophysics and Electronics of the National Academy of Sciences of Ukraine, Kharkiv 61085, Ukraine, e-mail: m.nataroff@gmail.com, moganat1196@gmail.com 97

11. **INFLUENCE OF STOCHASTICALLY DISTRIBUTED ENVIRONMENTAL PARAMETERS TO THE DETERMINISTIC SIGNAL**

Olszewski S.V.*, Lysyuk Yu.V.*
**Taras Shevchenko National University of Kyiv, 64/13, Volodymyrska Street, City of Kyiv, Ukraine, 01601,*
e-mail: olszewski.serge@gmail.com
e-mail: grishaeva-yulia@ukr.net 99

12. **GYROSCOPIC COUPLING IN THE OUTPUT SIGNAL OF A GYROSCOPE MEMS SENSOR**
R. Andriichuk, V. Boretskij
Taras Shevchenko National University of Kyiv, 64/13, Volodymyrska Street, Kyiv, Ukraine,
e-mail: r.andriichuck@gmail.com 101

13. **GEOMAGNETIC EFFECTS OF KYIV METEOROID**

Chernogor L. F., Shevelev M. B., Tilichenko N. M.
** School of Radiophysics, Biomedical Electronics and Computer Systems*
V. N. Karazin Kharkiv National University, 61022, Svobody Sq., 4, e-mail: chernogor@karazin.ua
*** e-mail: mykyta.b.shevelev@karazin.ua*
**** e-mail: tilichenko2021rr11@student.karazin.ua* 103

14. **EFFECTS OF ROCKET LAUNCHES IN THE IONOSPHERE DURING GEOSPACE STORMS**

L. F. Chernogor*, Y. H. Zhdanko*
**V. N. Karazin Kharkiv National University, Ukraine, 61022, Kharkiv, Svoboda Square, 4,*
e-mail: Leonid.F.Chernogor@gmail.com
**V. N. Karazin Kharkiv National University, Ukraine, 61022, Kharkiv, Svoboda Square, 4,*
e-mail: eugenezhd@gmail.com 105

9. MATHEMATICAL PROBLEMS OF APPLIED PHYSICS (MAP)

1. **MULTI-FRACTAL ANALYSIS IN PROBLEMS OF THE APPLIED PHYSICS**

Leonid F. Chernogor*, Oleg V. Lazorenko, Andriy A. Onishchenko*****
** School of Radiophysics, Biomedical Electronics and Computer Systems,*
V. N. Karazin Kharkiv National University, Kharkiv 61022, Ukraine e-mail: Leonid. F. Chernogor@gmail.com
*** School of Physics, V. N. Karazin Kharkiv National University, Kharkiv 61022, Ukraine,*
e-mail: Oleg.V.Lazorenko@karazin.ua
**** Faculty of Automatics and Computerized Technologies, Kharkiv National University of Radioelectronics, Kharkiv 61166, Ukraine, email: Andrey.Onishchenko@nure.ua* 109

2. **STUDY OF ORIENTATIONAL MOTION OF PROTONS ALONG THE C-AXES IN HEXAGONAL CRYSTALS USING QUADRATIC APPROXIMATION**

M.V. Maksyuta, V.I. Vysotskii, D.M. Maksyuta, S.V. Efimenko
Faculty of Radio Physics, Electronics and Computer Systems Taras Shevchenko Kyiv National University of Kyiv, Glushkova ave., 4g, e-mail: maksyuta.nik@gmail.com 111